ICES REPORT 17-05

March 2017

Smooth cubic spline spaces on unstructured quadrilateral meshes with particular emphasis on extraordinary points: Geometric design and isogeometric analysis considerations

by

Deepesh Toshniwal, Hendrik Speleers, Thomas J.R. Hughes

The Institute for Computational Engineering and Sciences
The University of Texas at Austin
Austin, Texas 78712

Reference: Deepesh Toshniwal, Hendrik Speleers, Thomas J.R. Hughes, "Smooth cubic spline spaces on unstructured quadrilateral meshes with particular emphasis on extraordinary points: Geometric design and isogeometric analysis considerations," ICES REPORT 17-05, The Institute for Computational Engineering and Sciences, The University of Texas at Austin, March 2017.

Smooth cubic spline spaces on unstructured quadrilateral meshes with particular emphasis on extraordinary points: Geometric design and isogeometric analysis considerations

Deepesh Toshniwal[a,*], Hendrik Speleers[b], Thomas J. R. Hughes[a]

[a] *Institute for Computational Engineering and Sciences, University of Texas at Austin, USA*
[b] *Department of Mathematics, University of Rome "Tor Vergata", Italy*

Abstract

We present a framework for geometric design and isogeometric analysis on unstructured quadrilateral meshes. Acknowledging the differing requirements posed by design (e.g., the convenience of an intuitive control net) and analysis (e.g., good approximation behavior), we propose the construction of a separate, smooth spline space for each while ensuring isogeometric compatibility — requiring the geometric models to be members of the analysis-suitable spaces. The methodology is simple and is presented for bi-cubic splines; extensions to higher degrees are possible, and are briefly discussed. The presentation has been structured to show compatibility with T-splines — a state-of-the-art CAD technology — but the approach should extend to other locally refinable spline technologies (based on local tensor-product structures). An instantiation of the framework is presented, and several numerical tests focused on geometric design and isogeometric analysis demonstrate the versatility of the developed framework, and show significantly higher convergence rates than attained previously in the considered setting.

Keywords: Unstructured quadrilateral spline spaces, Extraordinary points, Isogeometric analysis, Geometric modeling

*Corresponding author
Email addresses: deepesh@ices.utexas.edu (Deepesh Toshniwal), speleers@mat.uniroma2.it (Hendrik Speleers), hughes@ices.utexas.edu (Thomas J. R. Hughes)

1. Introduction

Isogeometric analysis was introduced in [20] to facilitate efficient design-through-analysis procedures. The goal of the technology is the unification of geometric modeling and engineering analysis. This is realized by exploiting the smooth spline spaces used for the former as the finite-element spaces required for the latter, thereby yielding exact geometry-representations for the purpose of analysis. Rejuvenating the study of higher-order methods, the methodology has been successfully applied to myriad problems; see [4, 16, 50, 55, 62] for example. However, an unintended consequence has been the inheritance of open problems in the field of geometric modeling, such as construction of smooth splines on unstructured quadrilateral meshes, working with trimmed geometries, transitioning from bivariate to trivariate representations, etc.; in this work we focus on the first, namely, unstructured splines.

Modeling geometries of arbitrary topologies using quadrilaterals leads, in general, to unstructured meshes containing *extraordinary points*, i.e., internal vertices where $\mu \neq 4$ edges meet. On the regular parts of the mesh, where the quadrilateral elements are locally arranged in a structured fashion, smooth splines can be built. However, there is no canonical way of constructing smooth splines on an unstructured arrangement of quadrilateral elements, and this leads to *multi-sided holes* around extraordinary points.

A smooth visual representation of spline surfaces associated with such meshes can be most easily obtained by employing the *subdivision* paradigm [39] — refinements applied to the mesh lead to the multi-sided holes shrinking as larger portions of the mesh become regular. However, the holes around extraordinary points only get filled in the limit of an infinite number of refinements which, practically, can never be realized. The smoothness characteristics of the resulting infinite patchwork of piecewise-polynomials can be analyzed [41, 44] and there exist efficient evaluation techniques [53]. Subdivision surfaces have been widely used in the field of computer graphics and computer animation, and have also been used in some instances for performing engineering analysis [10, 34, 46]. Nevertheless, the fact remains that these non-finite representations are much more complex to analyze and process (computation of integrals, for exam-

ple) than their closed-form counterparts that contain a finite number of polynomial patches. An alternative to the subdivision framework is a *patch-based* approach, where a piecewise-polynomial spline space is defined over all elements of the mesh and special modifications to m-ring quadrilateral elements in an extraordinary point's neighborhood are performed to ensure smoothness. This usually involves degree elevation in the immediate neighborhood of the extraordinary point [23, 24, 29, 50] and may introduce lines of reduced regularity [38, 50, 23]. All the aforementioned approaches in the literature lead to non-nested geometries during refinement, demonstrate sub-optimal approximation behavior when performing engineering analysis, and, despite geometric modeling being the driving force in their development, many of them do not yield a set of non-negative spline basis functions.

In a more recent work [36], some of the above mentioned problems are tackled by introducing C^1 spline elements in the neighborhood of extraordinary points, albeit only in the context of PHT splines [13]. The construction is based on the D-patch framework developed in [44]. Although the spline basis functions built in [36] are not non-negative, the spline spaces spanned by them are provably refinable and, as shown in [36] for a Poisson problem, demonstrate *almost*-optimal approximation behavior in the L^2 and H^1 norms. Despite the excellent results reported, the limited smoothness of PHT splines is a major shortcoming with regards to geometric modeling. Therefore, as it stands, construction of smooth spline spaces suitable for both geometric modeling and isogeometric analysis on unstructured quadrilateral meshes remains an open problem.

Note that almost all existing literature on this topic focuses on bi-cubic splines for the purposes of geometric modeling and engineering analysis. As these are the most widely used and studied class of splines in this context, we will follow suit.

In this work, taking inspiration from [36, 44], we present a novel design and analysis framework. The presentation is structured, for the sake of simplified exposition, in the context of bi-cubic, analysis-suitable T-splines [3, 26, 27, 50], the de facto standard for engineering design and isogeometric analysis. Nevertheless, the methodology seems highly portable and we expect it to be directly applicable in the context of higher

degrees and other locally refinable spline technologies (based on local tensor-product structures).

1.1. Our methodology

Before embarking upon the details of a new approach, it is always worthwhile to investigate first the motivations behind it. The driving force behind our approach is a desire for reconciliation between geometric modeling and computational (engineering) analysis, and in order to achieve this we look toward the attributes these fields prioritize.

Geometric modeling is a highly visual process and is driven by practical considerations. It is important to have simple, intuitive modeling tools that can be used to build visually pleasing geometries, and discrepancies below industrial tolerances (typically 10^{-5}) are considered admissible. With regards to the spline technology underlying the modeling process, this suggests prioritizing (a) a set of spline basis functions possessing properties such as non-negativity, smoothness, partition of unity and local support; and (b) a control net with familiar and understandable connectivity, such that pulling on its constituent control points modifies the associated surface in an intuitive manner. At the same time, properties such as exact nestedness of geometries during refinement, and optimal approximation by the spline spaces can be disregarded to a certain extent.

Computationally analyzing the designed geometric objects, on the other hand, is very much motivated by accuracy and stability considerations. For this purpose, keeping in mind that smooth splines put higher-order methods within our reach and allow easy analysis of higher-order PDEs, we wish to be able to construct (a) a set of spline basis functions that are smooth, form a partition of unity, have local support, and can represent the designed geometric objects exactly; and (b) a refinement scheme that generates a sequence of nested spline spaces that demonstrate optimal approximation behavior. In contrast to geometric modeling, non-negativity of basis functions and the connectivity of degrees of freedom are viewed as somewhat less important. It should be noted that while the nestedness of spline spaces ensures that the geometric objects are represented exactly at all refinement levels, it is not necessary for obtaining optimal

approximation behavior.

Keeping the above in mind, we outline a novel framework for geometric modeling and isogeometric analysis on unstructured quadrilateral meshes. Given a T-mesh satisfying mild restrictions [50], we acknowledge the differing requirements posed by design and analysis and propose a two-pronged solution. We aim to construct two spline spaces, called the *design* and *analysis spaces*, for the purposes of geometric modeling and isogeometric analysis, respectively. The general requirements imposed on the functions that span each space are the following: they should be bi-cubic splines that form a convex partition of unity, be linearly independent and locally supported, and be data-independent, that is, independent of the locations of the control points. These are useful properties to have from the vantage points of both design and analysis. Additionally, the following sets of disparate objectives are prioritized:

(a) Design space, $\mathbb{S}_D$:

- C^1 smooth at extraordinary points,
- the geometry must have a finite representation,
- only mesh vertices must have smooth spline basis functions associated with them, thus favoring "familiar" control nets and avoiding exotic control-point placements, and,
- for the sake of compatibility with the previous point, and as is the norm, the computational "book-keeping" [36] required when refining patch-based constructions is ignored, thereby yielding non-nested geometries; however, the *geometric consistency errors* [60] introduced by this non-nestedness should be kept small.

(b) Analysis space, $\mathbb{S}_A$:

- C^1 smooth at extraordinary points,
- the analysis space must be rich enough to represent any element of $\mathbb{S}_D$ exactly, and there must exist explicit, simple formulas dictating the change

of basis from the one spanning $\mathbb{S}_D$ to the one spanning $\mathbb{S}_A$,

- refinements should yield nested spline spaces in order to preserve the true geometry during analysis, and,
- the space must be rich enough to yield fast convergence to solutions of (higher-order) PDEs.

Aside from the proposed separation of spaces, a crucial component of our framework — actually, for all frameworks dealing with extraordinary points — is the imposition of smoothness at extraordinary points. Data-independent basis functions can be found using an optimization framework [30, 50] where the smoothness constraints are coupled with functional minimization to compute the Bézier extraction coefficients. We employ affine-invariant linear transformations, Π, for the same (in the spirit of [44]); the range of Π being equal to the null space of the smoothness constraints. We call such linear transformations *smoothing matrices*. We choose this approach as it is an explicit process and allows us to determine *a priori* the properties of the resulting spline basis from those of the particular smoothing matrix used. Being able to determine the framework's properties from the properties of Π hands control over to the users. Indeed, based on the (application-dependent) properties desired from the framework, users can decide the particular linear transformations to be used for smoothness imposition.

Figure 1 summarizes the properties the resulting framework allows one to obtain. It has a number of beneficial features regardless of the choice of Π. In particular, the geometric model has (a) a finite representation, (b) the usual vertex-based control points, (c) C^2 smooth contact between all elements except the 1-ring elements where we have C^1 smoothness, and (d) small geometric consistency errors during refinement. Furthermore, during isogeometric analysis on the geometric models, we (a) obtain simple, explicit formulas for exact representations of geometric models as elements of $\mathbb{S}_A$, and (b) observe excellent approximation behavior when solving PDEs.

Remark 1.1. *An interesting research direction arising out of the framework is the development of smoothing matrices possessing desirable properties that they, in turn, can endow unto the spline basis functions. For example, as we will see in Sections 3*

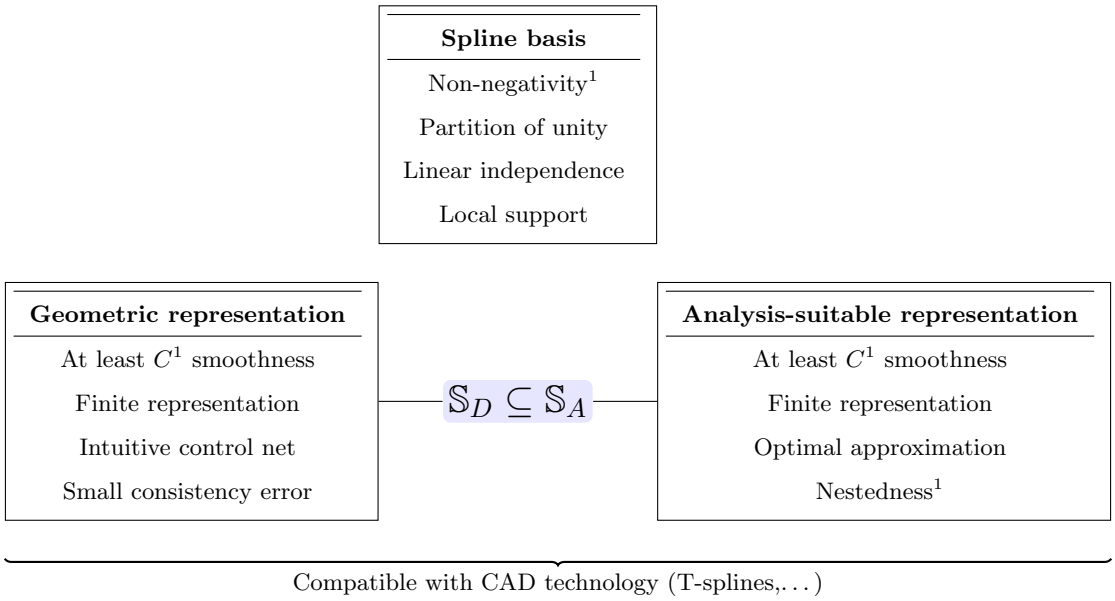

Figure 1: A summary of the properties achievable within our framework.

and 4, constructing basis functions that are non-negative and analysis-suitable spaces that are nested requires Π *to have non-negative entries and be idempotent, respectively.*

Remark 1.2. *In the present work, as in [36], we exploit the smoothing matrices developed in [44, Section 6]; see Section 5.1 and later. However, these matrices either have non-negative coefficients or are idempotent; we denote these by* Π^+ *and* Π°*, respectively. This entails making a choice between non-negativity of spline basis and nestedness of analysis spaces. While [36] chose* Π° *resulting in nested spaces, we focus primarily on non-negativity when presenting an instantiation of the framework in Section 5. While both choices result in excellent approximation behavior, we work with* Π^+ *as it yielded higher quality surfaces when applied to geometric modeling applications.*

Remark 1.3. *The initial* $\mathbb{S}_A$ *and subsequent refinements can exactly replicate the final, refined design space,* $\mathbb{S}_D$*, if the smoothing matrix ensures nestedness. Therefore, with the additional property of partition of unity, the isoparametric concept implies all rigid body motions and uniform strain states are exactly representable. These facts imply all patch tests are automatically passed. If the smoothing matrix does not ensure nestedness, patch tests are still satisfied assuming that, at each refinement level, the analysis space is used to represent the geometry.*

1.2. Related literature

The subdivision paradigm [39] has been used extensively in the fields of computer graphics and computer animation. The infinite piecewise-polynomial patchwork around

[1]Contingent upon the properties of the smoothing matrix; see Sections 3 and 4.

extraordinary points means that analyzing smoothness of the limit surface is an involved process. In [42], a solution was presented for analyzing tangent plane continuity of limit surfaces using eigenvalues of the subdivision matrix and characteristic maps. For higher-order smoothness, degree estimates and construction of subdivision schemes were presented in [40, 41, 43]. While subdivision usually deals with uniform non-rational splines, non-uniform subdivision surfaces can be built, see [52] for example, and, in particular, a scheme for building non-uniform rational subdivision surfaces of arbitrary topology and arbitrary odd degrees was presented in [7]. The scheme made use of the multi-stage symmetric and non-uniform knot-insertion scheme developed in [8]. Notable examples of use of subdivision surfaces for engineering analysis are [9, 10, 34, 46]. In [56], a framework for truncated hierarchical Catmull–Clark subdivision with local refinement is developed but suffers from the lack of an inexpensive and accurate quadrature scheme, a problem common with subdivision-based schemes.

Schemes that rely on a finite polynomial patchwork around extraordinary points have also been explored extensively over the years. A methodology for patching Catmull–Clark meshes using NURBS patches that are C^2 almost everywhere, and tangent-plane continuous near extraordinary points was presented in [38]. Second-order smoothness was achieved in [24, 31, 40], for example, using Bézier patches of degrees 6 and 7. In particular, [31] explicitly computed data-independent spline basis functions by minimizing a quadratic energy functional. The basis functions, however, violated the convex hull property as they were observed to be slightly negative.

The observation that geometrically continuous constructions yield parametrically continuous isogeometric methods [18] has been put to use in [23, 34, 35] for performing engineering analysis on unstructured meshes. While optimal convergence rates have been reported for the special case of bi-quadratic splines with symmetric tessellations of a disk utilizing only valence 3 extraordinary points, in general they are sub-optimal. For example, in the bi-cubic spline setting, [23] performed a G^1 construction using bi-quartic Bézier elements near extraordinary points and observed error convergence rates similar to bi-quadratic elements. The G^1 join of bi-linearly parameterized patches

presented in [11, 22] leads to optimal convergence rates but does not have a nice set of non-negative spline basis functions and, more importantly, is not applicable to the multi-sided hole problem as posed here.

A possible extension of T-splines to unstructured quadrilateral meshes for the purpose of design and analysis was presented in [50], and applications to the boundary element method were considered in the same work. Linear independence of analysis-suitable T-splines over unstructured meshes was proven in [25]. Truncated T-splines were presented in [57] using a G^1 construction around extraordinary points, but sub-optimal approximation behavior was observed. The geometric consistency errors introduced by non-nested refinements of unstructured T-spline geometries were analyzed in [60], and a new refinement scheme was proposed with the aim of achieving uniform meshes upon refinement. An analysis-oriented application showed that error convergence rates were similar to those for bi-quadratic splines.

Bi-cubic Hermite spline spaces over quadrilateral meshes with arbitrary topology were investigated in depth in [58]. In particular, their Hermite basis functions are allowed to be singular at extraordinary points by means of vanishing first derivatives. Optimal approximate rates in the L^2 norm were proved theoretically and observed numerically for a second-order non-linear PDE. Similarly, [36] constructed bi-cubic C^1 spline elements that complement PHT-splines [13] by utilizing a singular construction from [44] coupled with a 2×2 element splitting around the extraordinary point. Almost-optimal convergence rates for the Poisson equation were observed numerically. However, the fact that PHT-splines are only C^1 in the bi-cubic setting limits applicability of their technique.

Manifold techniques are another well-known approach in computer graphics for construction of smooth surfaces [17, 33, 59]. Recently, [32] employed such a technique in the context of isogeometric analysis. Almost-optimal convergence rates were shown for the Poisson equation in the bi-quadratic setting. However, the basis functions they constructed are not non-negative and require an excess of quadrature points. T-spline manifolds were studied in [47], for which optimal approximate rates in the L^2

norm were proved theoretically in a simplified configuration (with C^0 continuity in the neighborhood of the extraordinary point).

1.3. Overview

In Section 2, we introduce preliminary concepts related to unstructured meshes and the existing literature our technique is based upon. In particular, Section 2.1 introduces an approach for smoothly joining $\mu \neq 4$ Bézier patches at an extraordinary point using singular parameterizations and suitable smoothing matrices, Π, while Section 2.2 defines unstructured quadrilateral meshes in the context of our work.

In Section 3 we propose a framework for geometric modeling on unstructured meshes. Section 3.2 outlines the construction of vertex-based spline basis functions that have local support and form a (possibly convex) partition of unity. They are C^1 on the 1-ring elements and C^2 everywhere else. A simple refinement scheme is presented in Section 3.3.

In Section 4 we describe a framework for performing analysis on the unstructured geometries built in Section 3. Section 4.3 outlines the construction of analysis-suitable spline basis functions that have local support, form a (possibly convex) partition of unity, and are at least C^1 smooth in the neighborhood of extraordinary points. We prove nestedness of the constructed spline spaces under refinement in Section 4.4, demonstrating the possibility of exact geometry representation at all refinement levels.

In Section 5, we instantiate our abstract framework, and several numerical tests demonstrate its applicability to geometric modeling (Section 5.2) and isogeometric analysis (Section 5.3). Extensions (to arbitrary degrees, other locally refinable spline technologies, etc.) are briefly discussed in Section 6.

2. Preliminaries

In this section we collect several preliminary concepts and notations that are needed for the construction of our spline spaces over unstructured quadrilateral meshes.

First, we present in Section 2.1 a methodology for connecting μ Bézier patches smoothly at an extraordinary point using singular parameterizations. Subsequent to

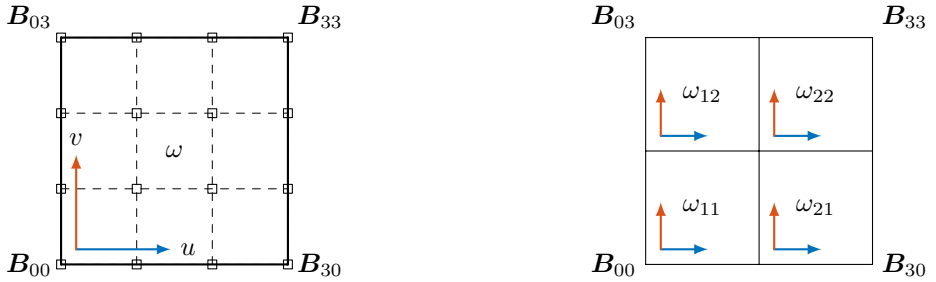

(a) Bézier element with control points (b) Element labeling after refinement

Figure 2: A bi-cubic Bézier parent element, ω, together with a schematic representation of the corresponding Bézier control points $\boldsymbol{B}_{pq}$, $p, q = 0, \ldots, 3$, is shown in Figure 2a. The labeling of elements obtained after refining the Bézier element is shown in Figure 2b

definitions of Bézier patches and degenerate Bézier patches, or *D-patches*, we review in Section 2.1.1 the C^1 smoothness constraints placed on the Bézier control points when two Bézier patches share a common edge. In Section 2.1.2 we outline a solution to the smooth contact of μ uniform Bézier patches at an extraordinary point using the theory of D-patches developed in [44]. Then, in Section 2.1.3 we introduce suitable linear transformations that can be used as smoothing matrices. In our work, instead of a direct application of the D-patch framework, we will first apply a 2×2 split to each of the Bézier elements, as in [36], and Section 2.1.4 elaborates upon the approach. In Section 2.2 we define all relevant concepts related to unstructured quadrilateral meshes and introduce definitions of admissible meshes. Finally, in Section 2.3 we give an outlook on our approach for constructing unstructured spline spaces in terms of smooth basis functions with specific properties of interest for design and analysis.

2.1. Degenerate Bézier patches

A bi-cubic Bézier patch $\boldsymbol{x}$ is obtained by mapping a *parent element* $\omega := [0,\ a^1] \times [0,\ a^2] \subset \mathbb{R}^2$, where $a^1, a^2 > 0$, to $\mathbb{R}^d$ using 16 bi-cubic *Bernstein (polynomial) basis functions*, b_{pq}, and 16 *Bézier control points* or *degrees of freedom*, $\boldsymbol{B}_{pq} \in \mathbb{R}^d$,

$$\boldsymbol{x}(u, v) := \sum_{p,q=0}^{3} \boldsymbol{B}_{pq} b_{pq}(u, v) \in \mathbb{R}^d, \quad \boldsymbol{u} := (u, v) \in \omega \ . \tag{2.1}$$

Such a Bézier parent element is visualized in Figure 2. Note that, when needed, we will denote the local coordinate system of Bézier elements with the same colored arrows as in Figure 2, and this convention will also inform the numbering of the control points.

Definition 2.1 (D-patch [44]). *A Bézier patch is called a (generic) D-patch if*

(a) it is degenerate at $\boldsymbol{B}_{00}$*,*

$$\boldsymbol{B}_{00} = \boldsymbol{B}_{10} = \boldsymbol{B}_{01} = \boldsymbol{B}_{11} \ , \tag{2.2}$$

(b) there exist constants $\alpha, \delta \in \mathbb{R}$ *and* $\beta, \gamma \in \mathbb{R}^+$ *such that,*

$$\begin{bmatrix} \boldsymbol{B}_{21} - \boldsymbol{B}_{00} \\ \boldsymbol{B}_{12} - \boldsymbol{B}_{00} \end{bmatrix} = \begin{bmatrix} \alpha & \beta \\ \gamma & \delta \end{bmatrix} \begin{bmatrix} \boldsymbol{B}_{20} - \boldsymbol{B}_{00} \\ \boldsymbol{B}_{02} - \boldsymbol{B}_{00} \end{bmatrix} \ , \tag{2.3}$$

(c) $\boldsymbol{B}_{20} - \boldsymbol{B}_{00}$ *and* $\boldsymbol{B}_{02} - \boldsymbol{B}_{00}$ *are linearly independent.*

There exists a regular smooth re-parameterization for a (generic) D-patch in a neighborhood of $\boldsymbol{B}_{00}$, and it has a well-defined tangent plane there spanned by the vectors $(\boldsymbol{B}_{20} - \boldsymbol{B}_{00})$ and $(\boldsymbol{B}_{02} - \boldsymbol{B}_{00})$. We also recall a last result from [44] that concerns the refinability of D-patches.

Proposition 2.1. *Let the Bézier control points* $\boldsymbol{B}_{pq}$*,* $p, q = 0, \ldots, 3$*, define a D-patch* ω *for constants* α, β, γ *and* δ*. After performing a dyadic refinement for this Bézier element we get 4 new Bézier elements (see Figure 2b). The control points* $\tilde{\boldsymbol{B}}_{pq}$*,* $p, q = 0, \ldots, 3$*, related to* ω_{11} *also define a D-patch with constants* $\tilde{\alpha}, \tilde{\beta}, \tilde{\gamma}$ *and* $\tilde{\delta}$ *where,*

$$\tilde{\alpha} = \frac{1}{2}(\alpha + 1), \quad \tilde{\beta} = \frac{1}{2}\beta, \quad \tilde{\gamma} = \frac{1}{2}\gamma, \quad \tilde{\delta} = \frac{1}{2}(\delta + 1) \ . \tag{2.4}$$

Before we proceed to a solution to the problem of smooth contact at an extraordinary point, we briefly recall the well-known constraints that the control points need to satisfy when two Bézier patches join smoothly at a common edge.

2.1.1. Two Bézier patches sharing an edge

For $i \in \{1, 2\}$ define Bézier patches $\boldsymbol{x}^i$ as in Equation (2.1) for parent elements $\omega^i := [0,\ a^i] \times [0,\ a^{i+1}]$ and control points $\boldsymbol{B}^i_{pq}$. Let $\boldsymbol{x}^1$ and $\boldsymbol{x}^2$ join parametrically smoothly such that,

$$\boldsymbol{x}^1(0, t) = \boldsymbol{x}^2(t, 0) \ , \qquad \boldsymbol{x}^1_u(0, t) = \boldsymbol{x}^2_v(t, 0) \ , \qquad t \in [0,\ a^2] \ . \tag{2.5}$$

Using Equation (2.1) and elementary properties of the Bernstein basis functions, the above constraints can be equivalently posed in terms of the Bézier control points,

$$\boldsymbol{B}^1_{0q} = \boldsymbol{B}^2_{q0} = \frac{a^3}{a^3 + a^1}\boldsymbol{B}^1_{1q} + \frac{a^1}{a^3 + a^1}\boldsymbol{B}^2_{q1} \ , \qquad q = 0, \ldots, 3 \ . \tag{2.6}$$

2.1.2. Smooth contact of μ uniform Bézier patches

Let us now present, in the same vein as [44], a possible solution to the problem of smoothly joining $\mu \geq 3$ Bézier patches at an extraordinary point using D-patches. We consider Bézier patches $\boldsymbol{x}^i$, where $i = 1, \ldots, \mu$ and $\mu \in \mathbb{N}\backslash\{1, 2, 4\}$, such that,

(a) $\boldsymbol{x}^i$ are uniform Bézier patches, i.e., they share a common, square parent element, $\omega := [0,\ a]^2$, $a > 0$, and,

(b) $\boldsymbol{x}^i$ joins $\boldsymbol{x}^{i+1}$ parametrically smoothly,

$$\boldsymbol{x}^i(0, t) = \boldsymbol{x}^{i+1}(t, 0)\ , \qquad \boldsymbol{x}^i_u(0, t) = \boldsymbol{x}^{i+1}_v(t, 0)\ , \qquad t \in [0,\ a]\ , \tag{2.7}$$

where the index i is to be understood modulo μ. The common corner at which all patches meet, $\boldsymbol{B}_{00} := \boldsymbol{B}^1_{00} = \cdots = \boldsymbol{B}^\mu_{00}$, is an extraordinary point of valence μ. Expressing the smoothness condition in Equation (2.7) in terms of the Bézier control points as in Equation (2.6), we obtain a cyclic system of equations,

$$\boldsymbol{B}^i_{0q} = \boldsymbol{B}^{i+1}_{q0} = \frac{1}{2}\boldsymbol{B}^i_{1q} + \frac{1}{2}\boldsymbol{B}^{i+1}_{q1}\ , \qquad q = 0, \ldots, 3\ , \tag{2.8}$$

with i understood modulo μ. The solution to this cyclic system of equations that ensures a well-defined tangent plane at the extraordinary point requires the μ Bézier patches to be D-patches. This implies that we must have for all i,

$$\boldsymbol{B}^i_{00} = \boldsymbol{B}^i_{10} = \boldsymbol{B}^i_{01} = \boldsymbol{B}^i_{11} =: \boldsymbol{B}_{00}\ .$$

Therefore, assuming that the Bézier elements are smoothly connected, the corresponding control points must satisfy the following system of equations, where we have used Equations (2.3) and (2.8),

$$\begin{bmatrix} \boldsymbol{B}^i_{21} - \boldsymbol{B}_{00} \\ \\ \boldsymbol{B}^i_{12} - \boldsymbol{B}_{00} \end{bmatrix} = \frac{1}{2}\begin{bmatrix} \alpha^i & \beta^i \\ \\ \gamma^i & \delta^i \end{bmatrix}\begin{bmatrix} \boldsymbol{B}^i_{21} + \boldsymbol{B}^{i-1}_{12} - 2\boldsymbol{B}_{00} \\ \\ \boldsymbol{B}^i_{12} + \boldsymbol{B}^{i+1}_{21} - 2\boldsymbol{B}_{00} \end{bmatrix}\ , \tag{2.9}$$

for some constants $\alpha^i, \delta^i \in \mathbb{R}$ and $\beta^i, \gamma^i \in \mathbb{R}^+$. This, in turn, implies that out of the Bézier degrees of freedom,

$$\left\{\boldsymbol{B}^i_{21},\ \boldsymbol{B}^i_{12} : i = 1, \ldots, \mu\right\} \cup \{\boldsymbol{B}_{00}\}\ ,$$

only 3 can be chosen independently. Alternatively, we can arrange the smoothness constraints above in a matrix $\boldsymbol{A}$ (whose null space has dimension 3) and collect control points $\{\boldsymbol{B}^i_{11},\ \boldsymbol{B}^i_{21},\ \boldsymbol{B}^i_{12} : i = 1, \ldots, \mu\}$ into vectors, $\boldsymbol{B}_{pq} := \left[\boldsymbol{B}^1_{pq},\ \ldots,\ \boldsymbol{B}^\mu_{pq}\right]$, such that the following equation is satisfied,

$$\boldsymbol{A}\left[\boldsymbol{B}_{11},\ \boldsymbol{B}_{21},\ \boldsymbol{B}_{12}\right]^T = \boldsymbol{0}\ . \tag{2.10}$$

2.1.3. Smoothness-enforcing matrices

To avoid the inconvenience of choosing control points such that they a priori satisfy Equation (2.10), we introduce a set of linear transformations, Π, which we call smoothing matrices.

Definition 2.2 (Smoothing matrix)**.** *A matrix* Π *of size* $3\mu \times 3\mu$ *is called a smoothing matrix if,*

(a) Π *is affine-invariant, and,*

(b) columns of Π *span the null space of the matrix* $\boldsymbol{A}$ *in Equation* (2.10)*.*

Arbitrary control points $\{\boldsymbol{B}^i_{11},\ \boldsymbol{B}^i_{21},\ \boldsymbol{B}^i_{12} : i = 1, \ldots, \mu\}$ that do not necessarily satisfy Equation (2.10) can be transformed by such a smoothing matrix Π into a set of control points that do,

$$\left[\boldsymbol{b}_{11},\ \boldsymbol{b}_{21},\ \boldsymbol{b}_{12}\right]^T = \Pi\left[\boldsymbol{B}_{11},\ \boldsymbol{B}_{21},\ \boldsymbol{B}_{12}\right]^T\ . \tag{2.11}$$

Once the new, constraint-satisfying control points $\{\boldsymbol{b}^i_{11},\ \boldsymbol{b}^i_{21},\ \boldsymbol{b}^i_{12} : i = 1, \ldots, \mu\}$ have been obtained as above, one can obtain the remaining control points on the intra-element boundaries using Equation (2.8).

Remark 2.1. *Due to Proposition 2.1, refinability of D-patches implies that the smoothness constraint matrices* $\boldsymbol{A}$ *depend on the refinement level as the set of constants* $\{\alpha^i, \beta^i, \gamma^i, \delta^i : i = 1, \ldots, \mu\}$ *changes with each refinement. Thus, a necessary condition for refinability is ensuring that at each refinement level the columns of* Π *span the null space of the appropriately modified* $\boldsymbol{A}$*.*

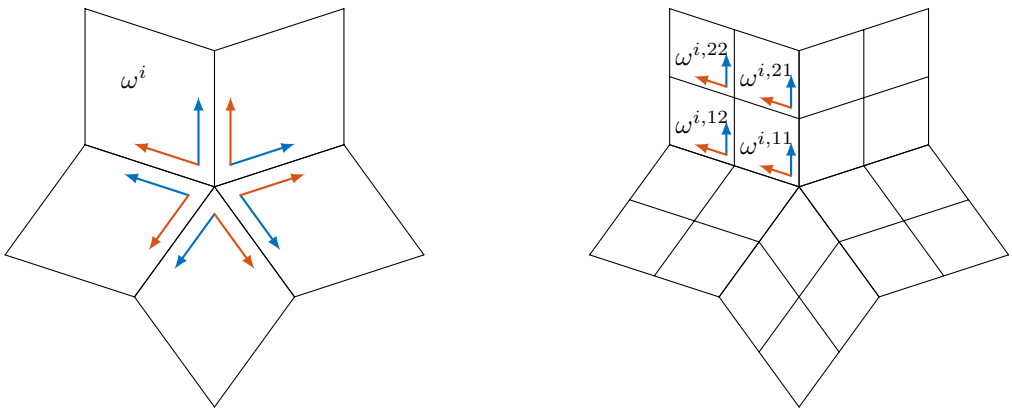

(a) Contact of μ Bézier elements (b) 2×2-split Bézier elements

Figure 3: Figure (a) shows, topologically, several Bézier elements meeting at a common point (with valence $\mu = 5$). As explained in Section 2.1.4, we split each element before applying the smoothing matrix Π, and Figure (b) shows, again topologically, the 2×2-split Bézier elements. The split-then-smoothen methodology works in two steps. First, the application of Π modifies only those control points that belong to the sub-elements with superscript $\{11\}$. Subsequently, the control points other sub-elements share with the $\{11\}$ sub-elements are modified to ensure C^1 smoothness conditions between all sub-elements are met.

Depending upon the additional properties that Π might have, we can make statements about the behavior of the transformed control points, $\boldsymbol{b}^i_{pq}$, obtained using Equation (2.11). We are particularly interested in two such properties — positive coefficients and idempotence — and the consequence of having these properties is stated explicitly in the following straightforward results.

Lemma 2.1. *If* $\Pi_{ij} \geq 0,\ \forall i, j = 1, \ldots, 3\mu$, *then the control points* $\{\boldsymbol{b}^i_{11},\ \boldsymbol{b}^i_{21},\ \boldsymbol{b}^i_{12} : i = 1, \ldots, \mu\}$ *obtained using Equation* (2.11) *lie within the convex hull formed by the control points* $\{\boldsymbol{B}^i_{11},\ \boldsymbol{B}^i_{21},\ \boldsymbol{B}^i_{12} : i = 1, \ldots, \mu\}$.

Lemma 2.2. *If* $\Pi^2 = \Pi$, *then* Π *is a projection and* $[\boldsymbol{b}_{11},\ \boldsymbol{b}_{21},\ \boldsymbol{b}_{12}]^T = \Pi\,[\boldsymbol{b}_{11},\ \boldsymbol{b}_{21},\ \boldsymbol{b}_{12}]^T$.

Perhaps not surprisingly, the properties mentioned in Lemmas 2.1 and 2.2 will be useful in the construction of non-negative spline basis functions and nested spline spaces, respectively; see Sections 3 and 4.

2.1.4. A 2×2 *split before* Π

Recently, [36] utilized the D-patch framework and a specific smoothing matrix developed in [44], and coupled them with a 2×2 Bézier element splitting to construct C^1 spline elements that complement PHT-splines. We adopt the same approach, albeit leaving the smoothing matrix Π as a variable. We next present a short overview of the approach.

Suppose that the Bézier control points of μ Bézier elements meeting at an extraordinary point already satisfy Equation (2.8) for $q = 1, 2, 3$. Then, the following is done to enforce C^1 smoothness at the extraordinary point. Figure 3 helps illustrate the steps below, and we will refer to this methodology as the *split-then-smoothen* approach.

(a) First, split each $\boldsymbol{x}^i$ into 4 sub-elements $\boldsymbol{x}^{i,jk}$, $j, k \in \{1, 2\}$, by splitting the parent element $\omega^i = \omega = [0,\ a]^2$ along parameter lines $u = a/2$ and $v = a/2$. The sub-elements $\omega^{i,jk}$ are indexed with jk as in Figure 3b. Let $\boldsymbol{B}^{i,jk}_{pq}$ be the control points that define the sub-element $\boldsymbol{x}^{i,jk}$. Recall that $\boldsymbol{B}^{i,jk}_{pq}$ can be obtained from control points $\boldsymbol{B}^{i}_{pq}$ using the de Casteljau algorithm. Let us denote with $\boldsymbol{S}^{jk}$ the matrix that acts upon the vector of control points $\boldsymbol{B}^{i}_{pq}$ to yield control points $\boldsymbol{B}^{i,jk}_{pq}$ when the square parent element ω is split at parameter lines $u = a/2$ and $v = a/2$. Then, we can write,

$$\boldsymbol{B}^{i,jk} = \boldsymbol{S}^{jk}\boldsymbol{B}^{i} \ . \tag{2.12}$$

(b) Next, transform the control points $\{\boldsymbol{B}^{i,11}_{11}, \boldsymbol{B}^{i,11}_{21}, \boldsymbol{B}^{i,11}_{12} : i = 1, \ldots, \mu\}$ using Π, as shown in Equation (2.11).

(c) Finally, for all i, adjust the control points at the boundaries of sub-elements $\boldsymbol{x}^{i,11}$ in a manner similar to Equation (2.6) such that C^1 smoothness between $\boldsymbol{x}^{i,11}$ and its neighbors is ensured.

Let us arrange the initial set of Bézier control points $\boldsymbol{B}^{i}_{pq}$, $i = 1, \ldots, \mu$, and $p, q = 0, \ldots, 3$, in a vector $\boldsymbol{B}$. Furthermore, let the final set of projected control points on each $\omega^{i,jk}$ be arranged in a vector $\boldsymbol{b}^{i,jk}$. Then, using the above approach, we can construct linear maps $\Pi^{i,jk}$ such that,

$$\boldsymbol{b}^{i,jk} = \Pi^{i,jk}\boldsymbol{B} \ . \tag{2.13}$$

We will refer to an un-split Bézier element as the *macro* element, and we will call each of the four sub-elements the *micro* elements. Quantities associated with the macro elements may be called macro quantities, and similarly for micro elements. For

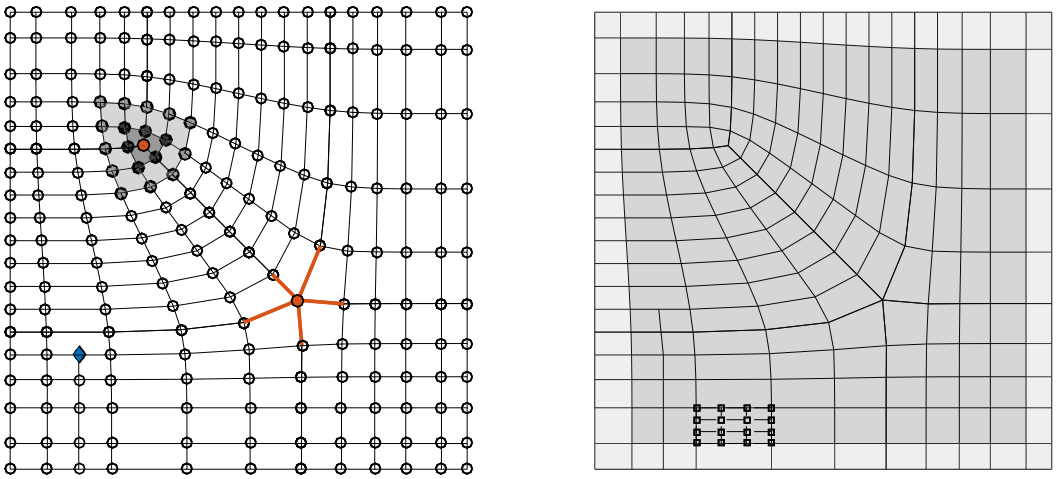

(a) Unstructured quad mesh (b) Elemental mesh

Figure 4: Figure (a) shows an unstructured quadrilateral mesh, $\mathcal{M}$, and its components [50]. The circular vertices are the mesh control points. The T-junction in the mesh has been highlighted with a blue diamond, while the extraordinary points have been shown with red disks. Edges highlighted in red are the spoke edges corresponding to the valence 5 extraordinary point. Similarly, the darkly and lightly shaded control points/faces are the 1- and 2-ring control points/faces for the valence 3 extraordinary point, respectively. Figure (b) shows the elemental mesh, $\mathcal{M}_{\text{el}}$, of $\mathcal{M}$. Each face in $\mathcal{M}_{\text{el}}$ is assigned a Bézier element. The outermost layer of faces, shaded lightly here, are usually assigned zero measure. This convention on the boundaries acts as a flag to indicate open knot vectors. Usually, open knot vectors are explicitly represented in B-splines and NURBS by end knots with $p+1$ multiplicities for splines of polynomial order p. The present convention emanates from T-spline technology.

instance, the initial set of un-smoothed control points may be called the macro control points, while the smoothed control points on each micro element may be called the micro control points.

2.2. Unstructured quad mesh

We define an unstructured quadrilateral mesh, $\mathcal{M}$, as in [50] but with some differences in terminology. Such a mesh is composed of quadrilaterals called *elements* or *faces*, and it can contain

(a) *T-junctions*: these are vertices that are analogous to hanging nodes in the finite element literature, and

(b) *extraordinary points*: these are vertices in the mesh interior that are not T-junctions and where $\mu \neq 4$ edges meet.[1]

[1]There is also the possibility of extraordinary points on mesh exterior boundaries, but we do not consider them herein.

An example $\mathcal{M}$ is shown in Figure 4. To each vertex in $\mathcal{M}$, a *control point* $\boldsymbol{P}_\ell \in \mathbb{R}^d$ and a *weight* $w_\ell \in \mathbb{R}^+$ are assigned. We will denote with $\boldsymbol{P}_\ell^w := (w_\ell \boldsymbol{P}_\ell,\ w_\ell) \in \mathbb{R}^{d+1}$ the homogeneous form of control points. The global index ℓ runs from 1 to n, which is the total number of vertices in $\mathcal{M}$. We will assume that there are n_{ep} extraordinary points in the mesh with valences μ_i, $i = 1, \ldots, n_{\text{ep}}$.

The set of 0-ring faces of an extraordinary point is by definition empty, and its 1-ring faces are all those that touch the extraordinary point. For $m \geq 2$, the *m-ring* faces of an extraordinary point are all faces that touch the $(m-1)$-ring faces and are not a part of the $(m-2)$-ring faces. The *m-disk* neighborhood of an extraordinary point is defined as the set containing all its 1-, 2-, ..., m-ring faces. The edges emanating from the extraordinary point will be called *spoke edges*.

The set of 0-ring vertices of an extraordinary point contains only the extraordinary point itself. For $m \geq 1$, the m-ring of vertices contains all those that lie on the m-ring of faces but are not a part of the $(m-1)$-ring of vertices. The m-disk of vertices is defined as the union of all the 0-, 1-, 2-, ..., m-ring vertices. The same terminology will be used for the associated control points.

In the context of T-splines, we also need the concept of *T-junction extensions*, which are normally composed of face and edge extensions. Face and edge extensions are defined to be closed, directed line segments originating at a T-junction [27, 49]. The *elemental mesh*, $\mathcal{M}_{\text{el}}$, is formed by adding all T-junction face extensions to $\mathcal{M}$, as shown in Figure 4b. The part of a face extension that lies on the face adjacent to the T-junction is called a *one-bay* face extension. Each face of $\mathcal{M}_{\text{el}}$ is assigned a bi-cubic Bézier element; we will denote the eth Bézier element with ω^e. To complete the specification of the spline basis to be defined over $\mathcal{M}_{\text{el}}$, non-negative real numbers, called *knot spans*, are assigned to its edges. Knot spans denote lengths in the parametric domain and we require that knot spans on opposite sides of every face in $\mathcal{M}_{\text{el}}$ sum to the same value. Usually, the outer layer of faces is excluded from $\mathcal{M}_{\text{el}}$ as at least two of their edges are assigned zero knot spans to emulate open knot vectors at mesh external boundaries.

Definition 2.3 (Admissible mesh)**.** *The mesh $\mathcal{M}$ is said to be admissible if it satisfies the following restrictions:*

(a) no T-junction extensions intersect,

(b) no one-bay face extension subdivides a face in the 3-disk neighborhood of an extraordinary point, and,

(c) no extraordinary point lies within the 3-disk neighborhood of another.

T-splines defined over an admissible mesh are called *analysis-suitable* as such T-splines have linearly independent basis functions forming a convex partition of unity [25, 61]. The concept of analysis-suitable T-splines was originally developed for T-meshes that have no extraordinary points [27]. The restrictions in Definition 2.3 are actually mild. Indeed, an inadmissible $\mathcal{M}$ that satisfies the first condition can be made admissible after at most two local subdivision steps.

Remark 2.2. *For our developments, we will only require the linear independence of the "regular" T-spline basis functions from [50, 25] — these are T-splines that are identically zero on the* 1*-ring elements of extraordinary points.*

Working with admissible meshes has at least two upshots.

- The 2-disk neighborhood of an extraordinary point is unaffected by the presence of T-junctions or extraordinary points elsewhere in the mesh.
- Each face in $\mathcal{M}$ that lies in the 2-disk neighborhood of an extraordinary point will be assigned a single Bézier element.

These allow for greatly simplified exposition. We will make use of the above observations and present our approach towards unstructured splines as local modifications applied to 2-disk neighborhoods in isolation. Figure 5 shows one such 2-disk neighborhood for a valence 5 extraordinary point.

Remark 2.3. *As is often done in the literature, we will abuse the term "extraordinary point" to mean either the mesh-vertex where $\mu \neq 4$ edges meet or the control point associated with such a vertex. Similarly, "element" will either mean a quadrilateral face in the elemental mesh or the Bézier element associated with such a face. The specific meaning being implied will be clear from the context.*

Definition 2.4 (Standard mesh)**.** *The mesh $\mathcal{M}$ is said to be standard if it is admissible and for any given extraordinary point, its spoke edges have the same knot spans assigned to them.*

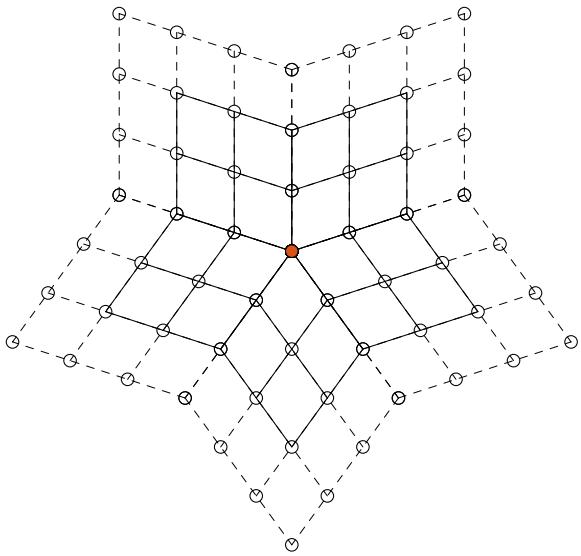

Figure 5: An admissible mesh, see Definition 2.3, has each extraordinary point neighborhood unaffected by T-junctions and extraordinary points elsewhere in the mesh.

A non-standard admissible mesh can be *standardized* using the subdivision algorithm provided in [7] to refine in the neighborhoods of extraordinary points, without violating conditions of admissibility. This can be performed in at most two subdivision steps. We justify the standardization step by its beneficial consequences for geometric modeling. We list some of these below, and the details will be provided in Section 3.

- On a standard mesh, it is possible to build spline surfaces such that the 2-ring elements of an extraordinary point join in C^2 fashion with all their 1- and 2-ring neighbors.

- As a consequence of the above mentioned additional smoothness, it is possible to exactly preserve the geometric map of 2-ring elements during mesh refinements. (We refer to Section 3.3.1 for the related discussion of why we *choose* not to preserve geometric maps for *all* elements during refinement.)

- Limiting all geometric-map changes to the 1-ring of elements enables us to come up with a very simple mesh refinement scheme in the extraordinary point's neighborhood. Several numerical tests in Section 5.2 highlight the fact that our approach leads to only small geometric consistency errors [60].

Remark 2.4. *Mesh standardization is certainly not mandatory and, if one wishes to work with non-uniform knots at the extraordinary point, we propose alternatives in*

Section 6. However, we believe that the aforementioned benefits usually outweigh the minor inconvenience of the standardization step.

2.3. Unstructured spline spaces: Outlook

We will construct spline spaces suitable for design and analysis over a standard mesh $\mathcal{M}$ in Section 3 and 4, respectively. They will be referred to as *design* and *analysis spaces*, respectively. For this purpose, we will group the control points and elements in $\mathcal{M}$ as being *regular*, *transition* or *irregular*. The following discussion of these labels motivates the naming convention.

- The regular control points will be unaffected by the presence of extraordinary points, and will have well-defined spline basis functions associated with them in the context of the T-spline theory. Therefore, we will largely exclude them from the following sections. Instead, we refer the reader to papers such as [3, 27, 48, 49] for details. As a consequence of mesh standardization, even the transition control points will have well-defined C^2 T-spline basis functions associated with them. However, we will include them in our discussions as they will be supported, in part, over the transition and irregular elements.

- In general, the elements of our design and analysis spaces will be C^2 smooth across all regular element boundaries, and C^1 smooth across all irregular element boundaries. The transition elements will be the single layer of elements separating regular and irregular elements.

Our approach toward the construction of design and analysis spaces will be indirect: we will focus on the construction of smooth, linearly independent spline functions over $\mathcal{M}$. The design and analysis spline spaces will simply be defined as the span of these splines. Each of the spline functions will be associated with a single degree of freedom. For geometric modeling, we will choose as the degrees of freedom the control points at the vertices of $\mathcal{M}$. For isogeometric analysis, we will exclude some of these vertex-based control points and introduce new ones on Bézier element interiors.

The construction of smooth spline basis functions over $\mathcal{M}$ will be done in a two-step process.

(a) **Macro extraction**: On the irregular and transition elements, we will construct a linear map from spline control points to the element-local Bézier control points. Such a linear map is called the *Bézier extraction operator* [6, 48], as it essentially *extracts* the Bézier element from the spline control points. Its transpose, referred to as the *spline extraction operator* here, maps the locally defined Bernstein basis functions on each Bézier element to the global spline basis functions. We will call it the *macro* spline extraction operator.

(b) **Micro extraction**: The spline basis functions defined using the macro extractions on each element will be smooth except on the 1-ring elements around the extraordinary point. We will rectify this using the split-then-smoothen approach from Section 2.1.4 — the macro extractions on 1-ring elements will be composed with the splitting and smoothing matrices from Section 2.1.2. This will yield spline basis functions that are linear combinations of Bernstein basis functions defined on the sub-elements of the 2×2-split 1-ring elements, and the corresponding linear map will be called the *micro* spline extraction operator.

Remark 2.5. *The exact sets of elements and control points which will be put in the categories regular, irregular, etc., will be constructed differently for the purposes of geometric modeling and isogemetric analysis (cf. Section 3.1 and Section 4.1, respectively). These differences arise out of our decision to adopt different approaches towards refinements of design and analysis spaces, and our motivations are elaborated upon in Section 3.3.1.*

3. Unstructured spline surfaces

We focus on aspects related to geometric modeling in this section. Specifically, given a mesh $\mathcal{M}$, we look at the construction of smooth surfaces on it. For this purpose, we present the construction of a smooth spline space, the *design space*, over $\mathcal{M}$ in Section 3.2. Subsequently, we propose a simple refinement strategy in Section 3.3. As is usual in unstructured spline treatments, we choose a simple refinement strategy that leads to non-nested geometries, and Section 3.3.1 sheds light on the reasons behind this decision. We start off by defining some additional terminology for the control points and elements in an extraordinary point's neighborhood.

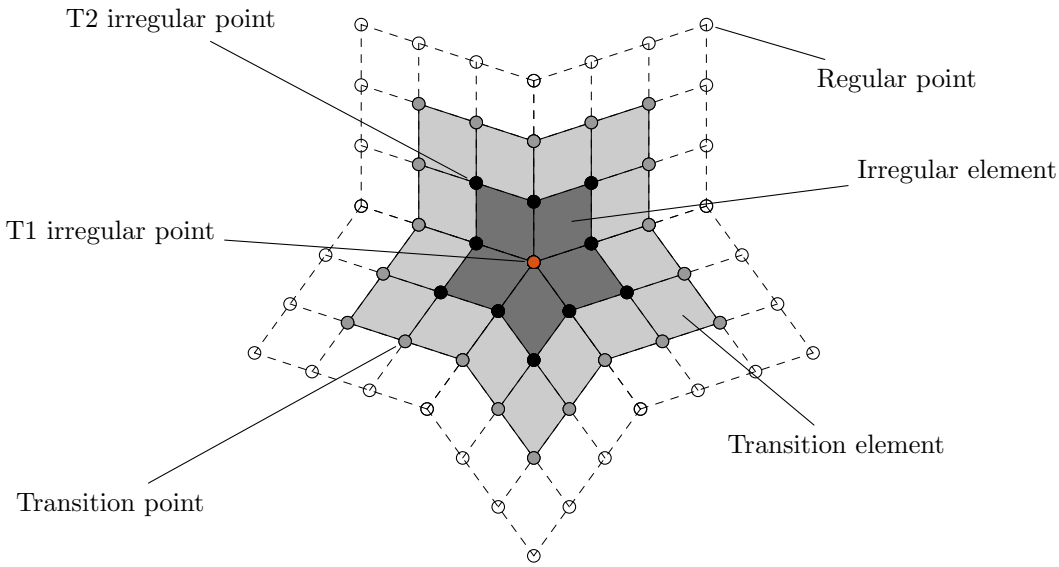

Figure 6: For geometric modeling, the 2-disk neighborhood of an extraordinary point is assigned additional labels as described in Section 3.1. The T1 irregular, T2 irregular, transition, and regular control points are indicated with circular disks that are red, black, light gray, and unfilled, respectively. These are the only spline control points that influence the 2-disk element neighborhood of the extraordinary point. Similarly, irregular and transition elements are indicated with dark and light gray shades, respectively. Note that the above color scheme will be adopted throughout this document to indicate the labels associated with control points/elements.

3.1. Irregular and regular control points and elements

As mentioned in Section 2.3, we place additional labels on the control points and elements in the neighborhoods of extraordinary points, and these are given below. Figure 6 illustrates the labels.

- The 1-disk control points of an extraordinary point will be collectively called *irregular* control points. We will further distinguish between two types: the extraordinary points and their 1-ring control points, referring to them as *T1* and *T2 irregular* control points, respectively. The 2-ring control points will be called *transition*, and all other control points will be called *regular*.

- The 1-ring elements of an extraordinary point will be called *irregular*, while the elements that lie in the 2-ring will be called *transition* elements. All other elements will be called *regular*.

3.2. Spline basis construction

In this section, we outline the construction of spline functions on mesh $\mathcal{M}$ for geometric modeling. We will assume that $\mathcal{M}$ has been standardized. Each control

point $\boldsymbol{P}_\ell^w$ will have an associated spline function M_ℓ, and the space spanned by these will be called the *design space*, denoted by $\mathbb{S}_D$,

$$\mathbb{S}_D := \text{span}\left(M_\ell \ : \ \ell \in \{1, \ldots, n\}\right) \ . \tag{3.1}$$

A spline function M_ℓ will be called *regular*, *transition* or *irregular* in accordance with the label of its control point $\boldsymbol{P}_\ell^w$.

As explained in Section 2.3, we will focus only on the construction of spline functions associated with the irregular control points. For the ith extraordinary point and its 2-disk neighborhood, we define $\mathcal{I}^{f,i}$ and $\mathcal{T}^{f,i}$ as the sets that contain all indices (i.e., their labels as per some global numbering scheme) corresponding to irregular and transition elements, respectively. Similarly, we define $\mathcal{I}^{v,i}$, $\mathcal{T}^{v,i}$ and $\mathcal{R}^{v,i}$ as the sets that contain all indices corresponding to irregular, transition and regular control points, respectively; see Figure 6 for reference. Our construction can be succinctly explained as follows.

(a) **Macro extraction**: For all $e \in \mathcal{I}^{f,i} \cup \mathcal{T}^{f,i}$, using the rules in Appendix A, we first construct the Bézier extraction $\boldsymbol{E}_e$ on ω^e. Using the macro spline extraction, $\boldsymbol{C}_e := \boldsymbol{E}_e^T$, we then obtain spline functions $M_\ell\big|_{\omega^e}$ associated with control points $\boldsymbol{P}_\ell^w$ in terms of the Bernstein basis functions defined on ω^e. The spline functions thus defined are C^2 for $\ell \in \mathcal{T}^{v,i}$. However, for $\ell \in \mathcal{I}^{v,i}$ the spline functions M_ℓ are only C^0 across the spoke edges, while C^2 at the contact between transition elements and their neighbors.

(b) **Micro extraction**: We now wish to increase the smoothness of the spline functions across spoke edges. Consider spline function M_ℓ, $\ell \in \mathcal{I}^{v,i}$, and collect its associated spline extraction coefficients from $\boldsymbol{C}_e$ for all $e \in \mathcal{I}^{f,i}$. These extraction coefficients are the Bézier degrees of freedom associated with M_ℓ on each irregular element. Then, we modify these degrees of freedom using Equation (2.13). Doing so for each spline function and for each irregular element, we obtain four micro spline extractions $\boldsymbol{C}_{e,jk}$ over each of the sub-elements $\omega^{e,jk}$ obtained by splitting ω^e, $j, k \in \{1, 2\}$. These result in C^1 smooth spline functions M_ℓ, $\ell \in \mathcal{I}^{v,i}$, over

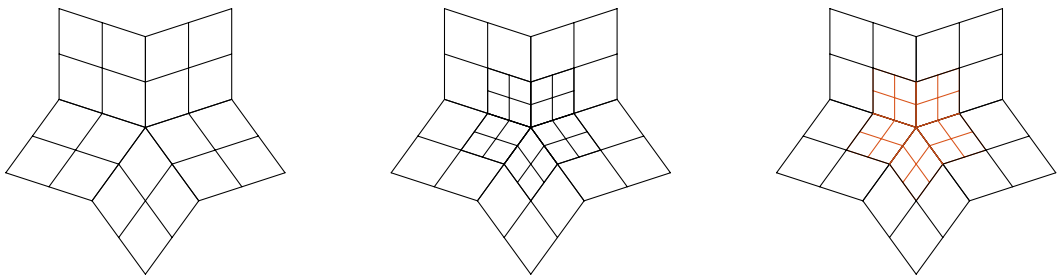

(a) Original 2-disk neighborhood (b) Modified 2-disk neighborhood (c) C^2/C^1 smoothness lines

Figure 7: Imposition of smoothness at the extraordinary point is performed by modifying 1-ring Bézier elements using the split-then-smoothen approach from Section 2.1.4. Referring to Figure (c), the construction in Section 3.2 leads to spline functions with smoothness C^2 across the black lines and C^1 across the red ones.

the modified 2-disk neighborhood shown in Figure 7b.

The above procedure is repeated for the 2-disk neighborhoods of all n_{ep} extraordinary points, and completes the construction of a spline function associated with each irregular control point. Figure 7c shows the smoothness of spline functions built using our construction: for $\ell \in \mathcal{I}^{v,i}$, M_ℓ is C^2 smooth across the black lines, C^1 smooth across the red lines, and a polynomial in the white space. The regular and transition control points are all associated with C^2 spline functions. Examples of irregular splines built in the above manner are presented in Section 5.

Remark 3.1. *The rules in Appendix A are those from [50] albeit with a small modification: the computation of vertex control points in Equation* (A.4) *differs from the one in [50] by a factor of* $\frac{4}{\mu}$*. This change has been introduced to ensure that all rows of the macro Bézier extraction* $\boldsymbol{E}_e$ *sum to* 1*, and helps retain partition of unity.*

Proposition 3.1. *The spline functions* M_ℓ*,* $\ell = 1, \ldots, n$*, have local support, and form a partition of unity. Moreover, the spline functions are non-negative if the smoothing matrices used have non-negative entries only.*

Proof. In the regular regions of the mesh, all the properties follow from the T-spline theory [61]. Therefore, let us consider a 2-disk neighborhood of one of the extraordinary points (with index i). On all $e \in \mathcal{I}^{f,i} \cup \mathcal{T}^{f,i}$, the properties of non-negativity, partition of unity, and locality follow directly from the above construction (i.e., the properties of the extraction operators).

- The properties are obvious for transition elements as they only involve the macro extraction operators built using rules in Appendix A.
- On irregular elements, construction of $\boldsymbol{E}_e$ in accordance with Appendix A implies that all of its rows sum to 1 and all of its entries are non-negative. Then, from the

affine-invariance of the smoothing matrices it is clear that each column of $\boldsymbol{C}_{e,jk}$ will sum to 1 for all $j, k \in \{1, 2\}$. Moreover, using Lemma 2.1, the smoothing matrices having non-negative entries is a sufficient condition for $\boldsymbol{C}_{e,jk}$ to have non-negative entries or, in other words, a sufficient condition for the spline functions M_ℓ to be non-negative.

□

Proposition 3.2. *The spline functions M_ℓ, $\ell = 1, \ldots, n$ form a basis for $\mathbb{S}_D$.*

Proof. We approach the proof by showing that the representation of the zero function should have zero coefficients. Suppose

$$\sum_{\ell=1}^{n} c_\ell M_\ell \equiv 0 \ , \tag{3.2}$$

on all elements of the mesh. We observe the following.

- The regular spline functions are linearly independent amongst themselves by the T-spline theory [25].
- The regular spline functions in the 3-ring of an extraordinary point are the only ones that share supports with the transition and irregular spline functions.

Therefore, the coefficients c_ℓ in Equation (3.2) must be zero for $\ell \in \mathcal{R}^v \setminus \cup_{i=1}^{n_{\text{ep}}} \mathcal{R}^{v,i}$, where $\mathcal{R}^v$ contains indices of all regular spline functions. In order to prove linear independence of the remaining spline functions, it is sufficient to focus on the transition elements. Consider the 2-disk neighborhood of the ith extraordinary point, the one shown in Figure 6, for instance.

Let $e \in \mathcal{T}^{f,i}$ correspond to the shaded element ω^e in Figure 8. Let $\boldsymbol{C}_e$ be the spline extraction operator that maps the 16 Bernstein basis functions defined on ω^e to the 4×4 grid of spline functions surrounding ω^e (their control points are shown in Figure 8 using blue disks). Since $\boldsymbol{C}_e$ constructed in accordance with Appendix A is a non-singular 16×16 matrix, reproduction of the zero function on ω^e implies that the coefficients c_ℓ associated with the 4×4 grid of spline functions must vanish.

Then, by considering all transition elements one by one, it is easy to see that the reproduction of zero implies that the coefficients c_ℓ associated with all degrees of freedom shown in Figure 6 must be equal to zero. Repeating the argument for all extraordinary points proves that all coefficients c_ℓ in Equation (3.2) must be zero, and so the assertion follows. □

Our proposed construction has the following advantages.

- We only use a finite number of bi-cubic Bézier elements for the C^1 completion around the extraordinary points.
- Standardization of $\mathcal{M}$ ensures that using the extraction rules in Appendix A leads to C^2 smooth contact of transition elements with all their neighbors.

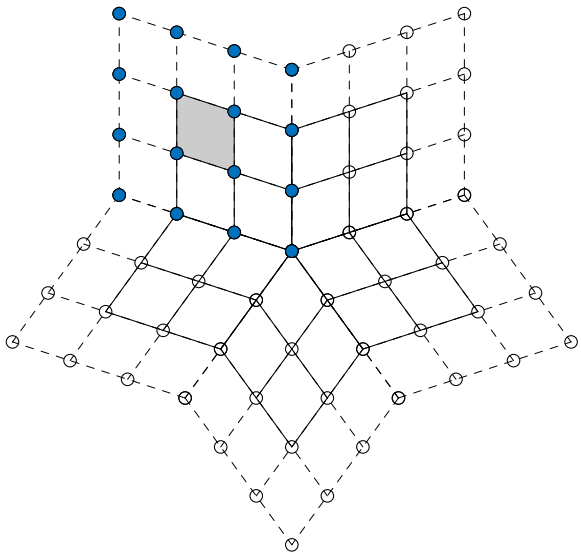

Figure 8: The 4×4 grid of control points that contribute to the Bézier control points on the lightly-shaded transition element are depicted with blue disks.

- The 2×2 split employed leads to a limited footprint of the D-patch framework's application. Indeed, the geometric map of transition elements is unaffected and the C^2 smooth contact between irregular and transition elements is preserved.

Using the spline basis functions M_ℓ and control points $\boldsymbol{P}_\ell^w$, an unstructured spline surface $\boldsymbol{S} \subset \mathbb{R}^d$ can be constructed by the usual perspective projection of $\boldsymbol{S}^w$ from $\mathbb{R}^{d+1}$ to $\mathbb{R}^d$ where,

$$\boldsymbol{S}^w(u,v) = \sum_{\ell=1}^{n} \boldsymbol{P}_\ell^w M_\ell(u,v) \ . \tag{3.3}$$

3.3. Refining surfaces

In the last section we saw the construction of unstructured spline surfaces, and we aim to discuss refinement of such surfaces here. However, before we proceed with the details, it is worthwhile to delve a little deeper into what refinement entails, and why non-nested refinements are the norm for unstructured spline surfaces; see [23, 32, 50] for example. While this may be obvious to the geometric modeling community, the same cannot be said with certainty for the engineering analysis community, and we deem the following discussion worthwhile.

In the following, and subsequently, we will denote the surfaces, meshes, spline spaces, etc., at refinement level k by indexing them with a superscript, $(\cdot)^k$. Missing

superscripts and superscripts of 0 will be taken to mean the same thing, namely quantities at the coarsest refinement level. All meshes $\mathcal{M}^k$ are implicitly assumed to be standard (see Definition 2.4).

3.3.1. Rationale for non-nested refinements

Ideally, we would like the refinement of unstructured spline surfaces to mimic the refinement of structured spline surfaces. In other words, we would like all refinements to be such that the design spaces are nested at successive refinement levels, $\mathbb{S}_D^k \subseteq \mathbb{S}_D^{k+1}$; this is a sufficient condition for a general geometry to stay invariant. At the same time, it should be observed that:

- A C^1 construction around extraordinary points introduces lines of reduced continuity (see Figure 7c for example), and may even introduce degree-elevated Bézier elements [50] in the 1-ring neighborhood.
- A C^2 construction around extraordinary points must necessarily introduce degree-elevated Bézier elements in the 1-ring neighborhood [5, 43, 24].

Then, maintaining nestedness of design spaces entails,

- preservation of the zones of reduced continuity, and,
- preservation of the zones of degree-elevation.

We view these restrictions as highly undesirable for the purpose of geometric modeling. Indeed, the first one would necessitate using splines of reduced smoothness, while the second would require non-uniform polynomial degree splines in regions where well-defined bi-cubic C^2 T-spline basis functions could be built – simply because, at some coarser refinement level in the past, the same could not be done. Not only would this require further developments in non-uniform degree bivariate spline technology, it may also lead to unintuitive placement of spline control points and control-net connectivities.

In light of the above observations, we opt for performing non-nested refinements of our unstructured spline surfaces during the geometric modeling phase. That is, we perform the C^1 construction outlined in Section 3.2 in a memory-less fashion. This

is done at all refinement levels by labeling control points and elements as irregular, regular, etc., according to Section 3.1 — i.e., without any reference to the number of refinements the original mesh has undergone — and, then, constructing the new design space as in Section 3.2.

3.3.2. Refinement types

In order to simplify our discussion on refinements, we first isolate the refinements applied to regular regions of the mesh from those applied to the 2-disk neighborhoods of extraordinary points.

(a) R1: Valid T-spline refinements applied in the regular regions of $\mathcal{M}^k$ that leave the 2-disk neighborhoods of all extraordinary points unchanged, i.e., no transition or irregular elements are refined.

(b) R2: For one or more extraordinary points, all the transition and irregular elements are split into 2×2 new elements. If the refinements need to propagate into the regular region in accordance with the T-spline theory, they are assumed to do so.

Refinements R1 and R2 can be combined to obtain more complex styles of refinement. The former are well understood [26, 49] and lead to nested spaces and thus invariant geometry. We will, therefore, specialize our discussion by considering only R2 refinements. For the refined mesh to be standard, we require that the 1-ring elements are always split at parameter lines $u = a/2$ and $v = a/2$, where $0 < a \leq a_0$ and a_0 is the spoke edge knot span. In particular, we will choose $a = a_0$ as this was seen to yield better results during refinement studies. Additionally, since we are choosing to split all irregular and transition elements, and since splitting zero knot spans at each refinement level will eventually lead to discontinuities, we restrict ourselves to non-zero knots spans in the 2-disk neighborhood to avoid the discussion of such special cases.

3.3.3. Refinement strategy

While we have opted for non-nested refinements during geometric modeling, we would still like to minimize the geometric consistency errors [60] introduced when $\boldsymbol{S}^k$

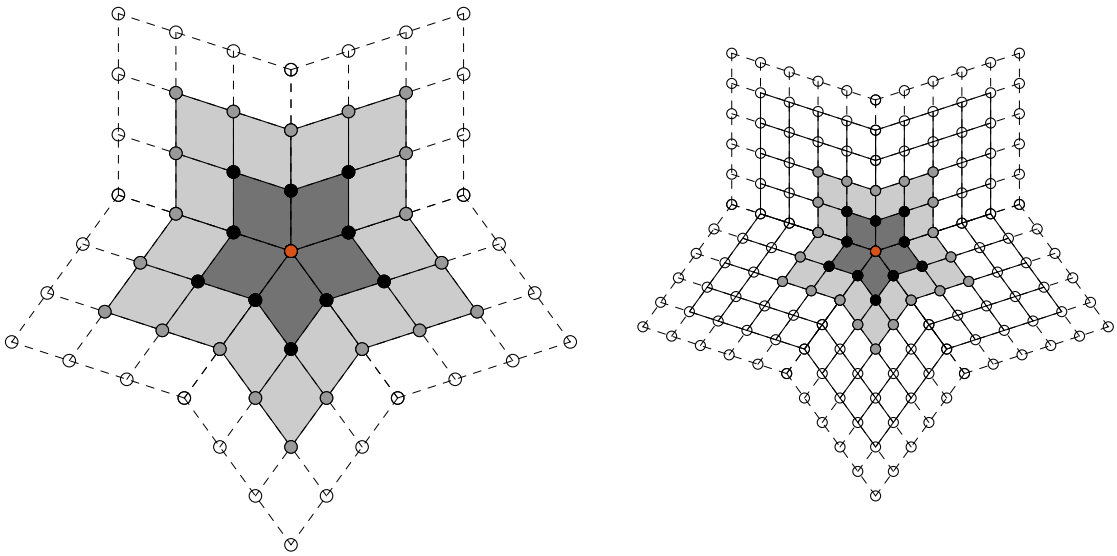

(a) Coarse 2-disk neighborhood (b) R2 refined 4-disk neighborhood

Figure 9: Modification of the 2-disk neighborhood, and the control point and element labels, when an R2 refinement is applied. The control points and element colors and shades correspond to their labels (see Figure 6 for reference). In Figures (a) and (b), only those control points have been shown that affect the (initial) 2-disk and (refined) 4-disk element neighborhoods of the extraordinary point, respectively.

is refined to obtain $\boldsymbol{S}^{k+1}$. To achieve this, we propose a conceptually simple refinement strategy that, as the numerical tests presented in Section 5.2 demonstrate, leads to small errors in practice. Let us look at Figure 9 where we show the 2-disk neighborhood of an extraordinary point on the left, and the R2 refined 2-disk neighborhood on the right.

Assuming that such a refinement can be carried out without violating any of the conditions in Definition 2.3, it is implemented as follows, and such a control-point update procedure will be referred to as $\mathcal{U}_D$-updates.

(a) After addition of vertices and edges to $\mathcal{M}^k$, and an appropriate splitting of knot spans, we obtain $\mathcal{M}^{k+1}$.

(b) We re-categorize the element and control points as regular, irregular, etc., according to Section 3.1, and construct the design space $\mathbb{S}_D^{k+1}$ on $\mathcal{M}^{k+1}$ as outlined in Section 3.2.

(c) In homogeneous coordinates, for $\boldsymbol{S}^{w,k} \in \left(\mathbb{S}_D^k\right)^{d+1}$, we perform the computation of

the homogeneous control points for $\boldsymbol{S}^{w,k+1} \in \left(\mathbb{S}_D^{k+1}\right)^{d+1}$ in the following manner:

(i) We require that the geometric maps of all regular elements of $\boldsymbol{S}^{w,k}$ stay invariant. This uniquely determines all the regular and transition control points for $\boldsymbol{S}^{w,k+1}$, and these can be computed using the usual T-spline refinement algorithm.

(ii) We require that the geometric maps of all transition elements stay invariant as well. This uniquely determines the new 1-ring control points of $\boldsymbol{S}^{w,k+1}$ as linear combinations of the 1-disk control points of $\boldsymbol{S}^{w,k}$. In fact, the update rules of 1-ring control points are simply the tensor-products of univariate knot-insertion rules, a consequence of mesh standardization. A general treatment of univariate rules can be found in [8], for example, and for completion we present them in the context of our work in Appendix B.

(iii) The only unknown control points at this stage are the extraordinary points. In order to compute them, we require that, for each extraordinary point, $\boldsymbol{S}^{w,k+1}$ interpolate the same point as $\boldsymbol{S}^{w,k}$ at the common meeting point of the irregular Bézier elements. This yields n_{ep} equations for n_{ep} extraordinary points. All equations are uncoupled from each other, and the cost of computing the new control points is negligible.

4. Unstructured isogeometric analysis

Section 3 outlined the construction of smooth spline surfaces on unstructured quadrilateral meshes $\mathcal{M}$. In order to devise an approach towards performing analysis on such geometries that is truly rooted in the philosophy of isogeometric analysis, we recall one of its primary goals (see [12, page 5]):

> "A fundamental step is to focus on one, and only one, geometric model, which can be utilized directly as an analysis model, or from which geometrically precise analysis models can be automatically built."

Then, in order to perform isogeometric analysis on the unstructured spline surfaces from Section 3, we require the following:

(a) an analysis-suitable spline space, $\mathbb{S}_A \supseteq \mathbb{S}_D$, and,

(b) a refinement scheme to generate a sequence of nested spline spaces, $\mathbb{S}_A =: \mathbb{S}_A^0 \subseteq \mathbb{S}_A^1 \subseteq \cdots \subseteq \mathbb{S}_A^k$,

where $\mathbb{S}_D$ is the design space on $\mathcal{M}$ used to construct the unstructured geometry we wish to perform analysis on. The first requirement ensures that the geometry is an element of the analysis-suitable space $\mathbb{S}_A$ invoked on $\mathcal{M}$. The second ensures that the geometry stays invariant as we refine; this is desirable when performing engineering analysis, and in certain cases — for example applications to problems posed in terms of minimum principles, such as the principle of minimum potential energy in linear elasticity theory — ensures that each successive refinement achieves a lower minimum; see [19, Chapter 4, pg. 188].

Remark 4.1. *For analysis, the geometry inherited from the geometric modeling stage is treated as the* true geometry *upon which analysis needs to be performed. Therefore, we relabel the inherited mesh and geometry as being the* coarsest level of refinement*, or refinement level $k = 0$. All refinements done for the purpose of analysis are done on this level.*

Before proceeding with details of the construction of $\mathbb{S}_A$, we first define the set of control points and elements that are marked irregular, regular, etc., in Section 4.1. Then, in Section 4.2 we revisit the well-known bi-cubic C^1 elements and describe how irregular spline functions can be modified to reduce the continuity between transtition and irregular elements to C^1. This prepares us for the construction of spline basis functions that span analysis-suitable spaces $\mathbb{S}_A^k$ on $\mathcal{M}^k$, presented in Section 4.3.

4.1. Irregular and regular control points and elements

Similar to Section 3.1, we categorize the control points and elements in the neighborhood of an extraordinary point as follows. Note that, unlike Section 3.1, the labels here depend on the number of refinements, k, that we have performed on the design geometry for the purpose of analysis. Figure 10, where a 2-disk neighborhood on

$\mathcal{M}^0 = \mathcal{M}$ and the 4-disk neighborhood on $\mathcal{M}^1$ obtained by its refinement have been shown, helps elucidate the following convention.

- The $(2^{k+1} - 1)$-disk control points of an extraordinary point will be collectively called *irregular* control points. We will further distinguish between two types: the $(2^{k+1} - 2)$-disk and $(2^{k+1} - 1)$-ring control points, referring to them as *T1* and *T2 irregular* control points, respectively. The 2^{k+1}-ring control points will be called *transition*, and all other control points will be called *regular*.

- The $(2^{k+1} - 1)$-disk elements of an extraordinary point will be called *irregular*, while the elements that lie in the 2^{k+1}-ring will be called *transition* elements. All other elements will be called *regular*.

The above labels have been defined as such considering only R2 refinements introduced in Section 3.3. That is, at each refinement stage *all* the irregular and transition elements (as defined above) are assumed to be split into 2×2 new elements. Moreover, the refinement is such that 1-ring elements are always split at parameter lines $u = a_0/2$ and $v = a_0/2$, where a_0 is the spoke edge length. This requirement, while a choice during the geometric modeling stage, is a necessary condition for ensuring nestedness during refinements, and is a consequence of the split-then-smoothen approach applied to 1-ring elements.

Remark 4.2. *For $k = 0$, the above definitions coincide with the ones in Section 3.1; cf. Figures 6 and 10a.*

4.2. C^1 elements and C^1 extensions onto irregular elements

Shown in Figure 11a, a C^1 element is defined to be a bi-cubic Bézier element with 4 spline control points/degrees of freedom on it. Each of the spline control points, $\tilde{\boldsymbol{P}}_L$, has an associated spline function, $\tilde{M}_L$, which is a linear combination of 4 underlying Bernstein basis functions. Figure 11b shows the coefficients of linear combination for the spline function associated with the control point in blue, and other spline functions can be built in a symmetric manner. As should be obvious, the spline functions $\tilde{M}_L$

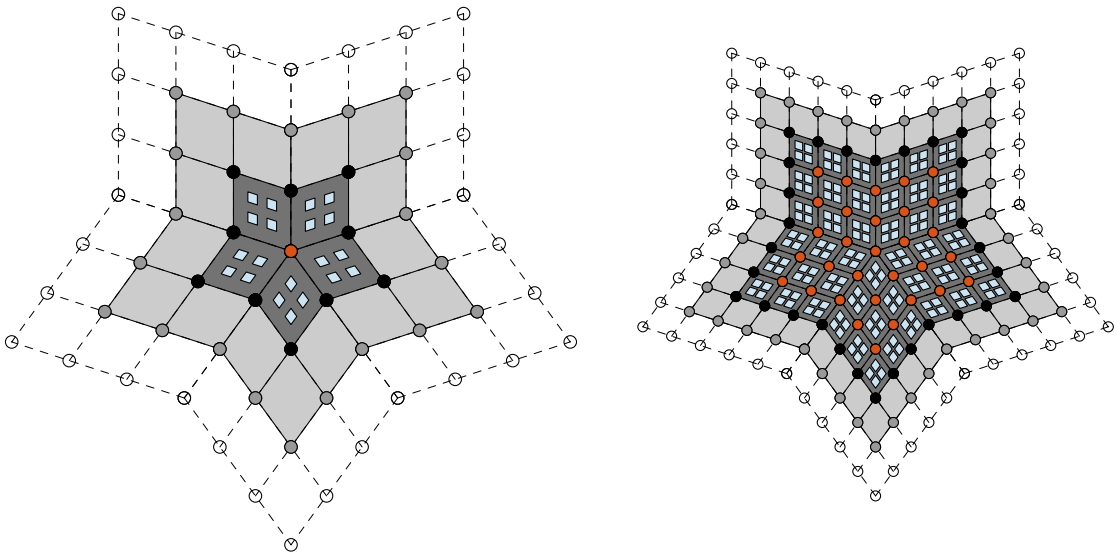

(a) $k = 0$ (b) $k = 1$

Figure 10: For isogeometric analysis, the neighborhood of an extraordinary point is assigned additional labels as described in Section 4.1. (Note that the above color scheme corresponds to the one used in Figure 6.) The T1 irregular, T2 irregular, transition, and regular control points are indicated with circular disks that are red, black, light gray, and unfilled, respectively. The irregular and transition elements are indicated with dark and light gray shades, respectively. The labels coincide with those defined for geometric modeling at refinement level $k = 0$, but differ for higher refinement levels (see Figure 6). Additionally, for isogeometric analysis, we designate the irregular elements as C^1 elements; their control points are indicated with blue squares. As can be seen, the number of C^1 element rings around the extraordinary point does not simply double as a consequence of refinement, but increases as $2^{k+1} - 1$ with the refinement level k. This approach ensures that while the outer boundary of the light gray transition elements has a C^2 join with the regular elements (not shown), all the other elements shown are C^1 continuous with each other; see also Figure 14. This, as explicated in Section 4.4.4, is a necessary condition for obtaining nested spaces via refinement. It is important to note that in each analysis model, such as in Figures (a) and (b) above, the control points that remain are all but the ones colored red. These define the degrees of freedom for our analysis space.

are non-negative, and on structured meshes ($\mu = 4$) they are the usual C^1 bi-cubic B-splines.

The analysis spaces we will construct in Section 4.3 will contain splines that are only C^1 smooth at the join of irregular and transition elements. Therefore, we will need to modify the extraction operators of irregular splines appropriately and Figure 12 illustrates the required modifications. There are two possible placements of a T2 irregular control point, as shown in Figures 12a and 12b. More precisely, the control point may lie at the common meeting point of either 3 transition and 1 irregular, or 2 transition and 2 irregular elements. Then, the macro Bézier extraction operator of the control point built according to Appendix A will include all the Bézier control points on

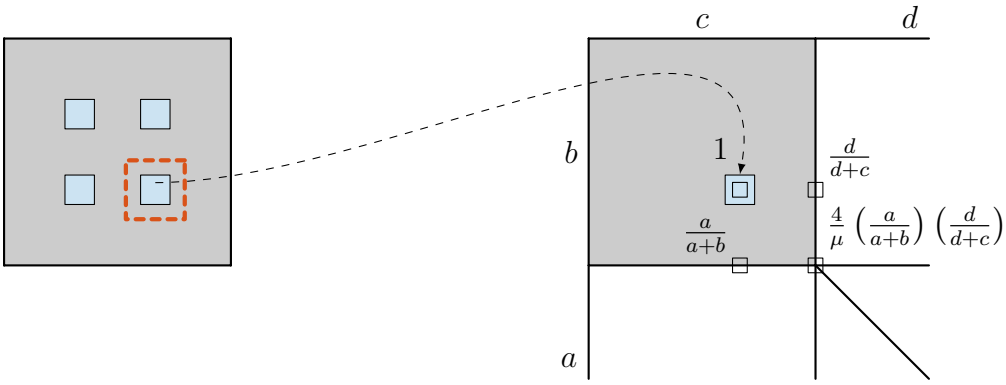

(a) Spline control points (b) Spline extraction coefficients

Figure 11: Figure (a) shows a C^1 element which has 4 spline control points attached to its face. The spline functions associated with the control points are each equal to a linear combination of 4 Bernstein basis functions. For instance, in Figure (b) we see that the spline function associated with the blue control point is a linear combination of the Bernstein basis functions associated with the 4 Bézier control points shown as black squares; the coefficients of such a linear combination are rational polynomial functions of knot spans, as given in the figure.

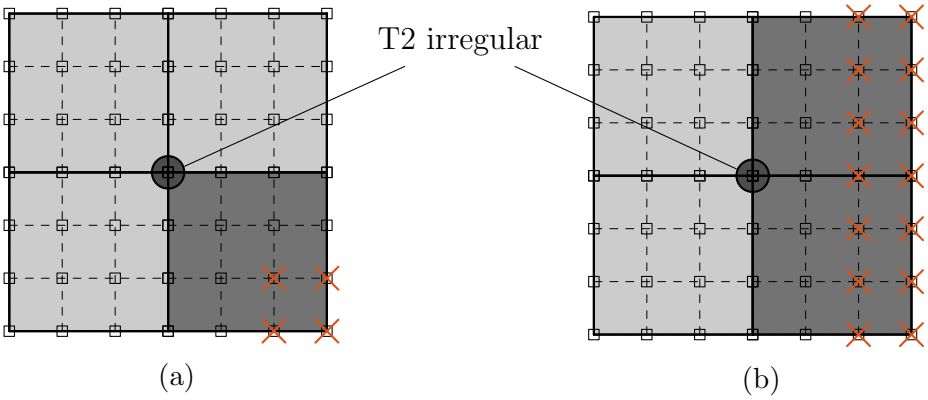

Figure 12: The two possible placements of a T2 irregular control point, indicated with a black circle. The corresponding transition and irregular elements are indicated with light- and dark-gray shades, respectively. From their macro extraction operators, built according to Appendix A, we eliminate the coefficients corresponding to the crossed out Bézier control points. In other words, we only allow a C^1 extension of irregular spline functions across the common boundary of transition and irregular elements.

the transition and irregular elements, as shown. However, in order to enforce only C^1 continuity between transition and irregular elements — equivalently, considering a C^1 extension of the T2 irregular spline functions from transition elements onto irregular elements — we eliminate the coefficients corresponding to the Bézier control points that have been crossed out in Figures 12a and 12b. Note that these changes leave the T2 irregular spline functions unchanged on transition elements.

We are now ready to present a modified collection of irregular spline functions for the purpose of analysis.

- We eliminate *all* spline functions associated with T1 irregular control points.
- For the T2 irregular control points, we modify the spline extraction operators on irregular elements, built initially according to Appendix A, such that only C^1 smoothness is enforced between transition and irregular elements as described above.
- We designate all irregular elements as C^1 elements. In order to ensure the property of partition of unity, we may need to scale the corresponding spline functions $\tilde{M}_L$. The scaling coefficients will be rational polynomial functions of knot spans.

The above setup leads to the following control-point structure; see Figure 10 for reference.

- After elimination of all T1 irregular control points, those that remain — i.e., the T2 irregular, transition and regular control points — are called *vertex-based control points.*
- Designation of irregular elements as C^1 elements introduces 4 new control points per irregular element. These are called *face-based control points*, and the corresponding set of indices is denoted with $\mathcal{F}^{v,i}$ when considering the ith extraordinary point's neighborhood.

We elaborate on construction of the basis functions in Section 4.3.

4.3. Spline basis construction

On mesh $\mathcal{M}^k$, i.e., when the 2-ring neighborhood on $\mathcal{M}^0$ has undergone k levels of R2 refinements, we explain how analysis-suitable spline spaces, $\mathbb{S}_A^k$, can be constructed. In a 2^{k+1}-disk neighborhood of the ith extraordinary point, we define $\mathcal{I}^{f,i}$ and $\mathcal{T}^{f,i}$ as the sets that contain all indices corresponding to irregular and transition elements, respectively. Similarly, we define $\mathcal{I}_1^{v,i}$, $\mathcal{I}_2^{v,i}$, $\mathcal{T}^{v,i}$ and $\mathcal{R}^{v,i}$ as the sets that contain

all indices corresponding to T1 irregular, T2 irregular, transition and regular control points, respectively. As defined in Section 4.2, the set $\mathcal{F}^{v,i}$ contains the indices of the face-based control points introduced on the irregular elements.

The spline space $\mathbb{S}_A^k$ is built by constructing smooth spline functions associated with the control points shown in Figure 10. A spline function will be called *vertex-based* (*T2 irregular*, *transition* or *regular*) or *face-based* in accordance with the label of its control point. As in Section 3.2, the construction follows the two-step procedure introduced in Section 2.3. Note that, even though we do not explicitly refer to the refinement level k in the following steps, the control point and element sets depend on k, as explained in Section 4.1.

(a) **Macro extraction**: We first construct spline extraction operators on the Bézier elements ω^e, $e \in \mathcal{I}^{f,i} \cup \mathcal{T}^{f,i}$. This is done as follows.

   (i) For all $e \in \mathcal{I}^{f,i} \cup \mathcal{T}^{f,i}$, we construct the Bézier extraction operator $\boldsymbol{E}_e$ that maps control points $\boldsymbol{P}_\ell^w$, $\ell \in \mathcal{I}_2^{v,i} \cup \mathcal{T}^{v,i} \cup \mathcal{R}^{v,i}$, to Bézier control points on ω^e using the rules in Appendix A and the C^1 modifications outlined in Section 4.2. Recall that $\mathcal{I}_1^{v,i}$ does not contribute. The spline extraction operator, $\boldsymbol{C}_e = (\boldsymbol{E}_e)^T$, defines the vertex-based spline functions, $N_\ell\big|_{\omega^e}$.

   (ii) The extraction operators of the spline functions $\tilde{M}_L$, $L \in \mathcal{F}^{v,i}$, are built according to Figure 11b. In order to ensure the property of partition of unity, we need to multiply their spline extraction coefficients with appropriate scaling coefficients, $\tilde{s}_L$. Only those spline functions that are non-zero at the common boundaries of transition and irregular elements need to be scaled, and the two different types of scaling coefficients needed are shown in Figures 13a and 13b. The scaling coefficients of the other spline functions are set to 1. The spline extraction operator built in this manner on ω^e is denoted by $\tilde{\boldsymbol{C}}_e$ and defines the face-based spline functions, $\tilde{N}_L\big|_{\omega^e}$.

(b) **Micro extraction**: The macro extraction operators $\boldsymbol{C}_e$ and $\tilde{\boldsymbol{C}}_e$ constructed as above define spline functions that are at least C^1 everywhere except across the

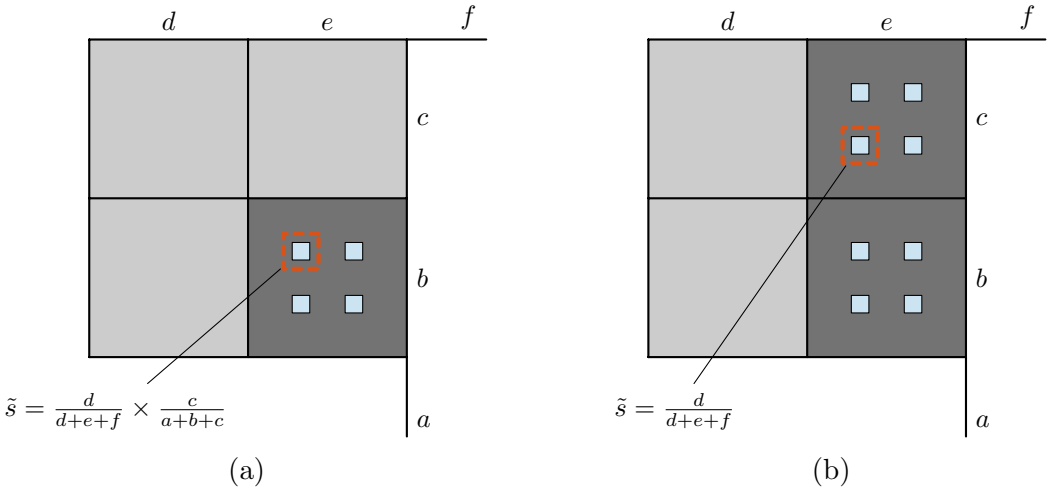

Figure 13: The scaling coefficients for two representative face-based spline functions that are non-zero at the common boundary of transition and irregular elements. The corresponding transition and irregular elements are indicated with light- and dark-gray shades, respectively.

spoke edges. Then, on the 1-ring of elements, we modify them using the split-then-smoothen approach from Section 2.1.4, Equation (2.13), to get micro extraction operators $\boldsymbol{C}_{e,jk}$, and $\tilde{\boldsymbol{C}}_{e,jk}$, $j,k \in \{1,2\}$. This completes the construction of C^1 smooth spline functions N_ℓ and $\tilde{N}_L$ over the modified 2-disk neighborhood shown in Figure 14.

Proposition 4.1. *The spline functions N_ℓ, $\ell \in \{1,\dots,n\}\backslash\mathcal{I}_1^v$, and $\tilde{N}_L$, $L \in \mathcal{F}^v$, have local support, and form a partition of unity, where,*

$$\mathcal{I}_1^v := \bigcup_{i=1}^{n_{ep}} \mathcal{I}_1^{v,i} \ , \qquad \mathcal{F}^v := \bigcup_{i=1}^{n_{ep}} \mathcal{F}^{v,i} \ . \tag{4.1}$$

Moreover, all of the spline functions, i.e. all N_ℓ and $\tilde{N}_L$, are non-negative if the smoothing matrices used have non-negative entries only.

Proof. The proof is similar to the one of Proposition 3.1, and follows directly from the above construction. □

Let us define the spline space $\mathbb{S}_A^k$ as follows,

$$\mathbb{S}_A^k := \text{span}\left(N_\ell,\ \tilde{N}_L\ :\ \ell \in \{1,\dots,n\}\backslash\mathcal{I}_1^v,\ L \in \mathcal{F}^v\right) \ . \tag{4.2}$$

According to the above construction, the smoothness of the analysis space varies with refinement as shown in Figure 14. Let us show next that the spline functions N_ℓ and $\tilde{N}_L$ form a basis for the analysis space.

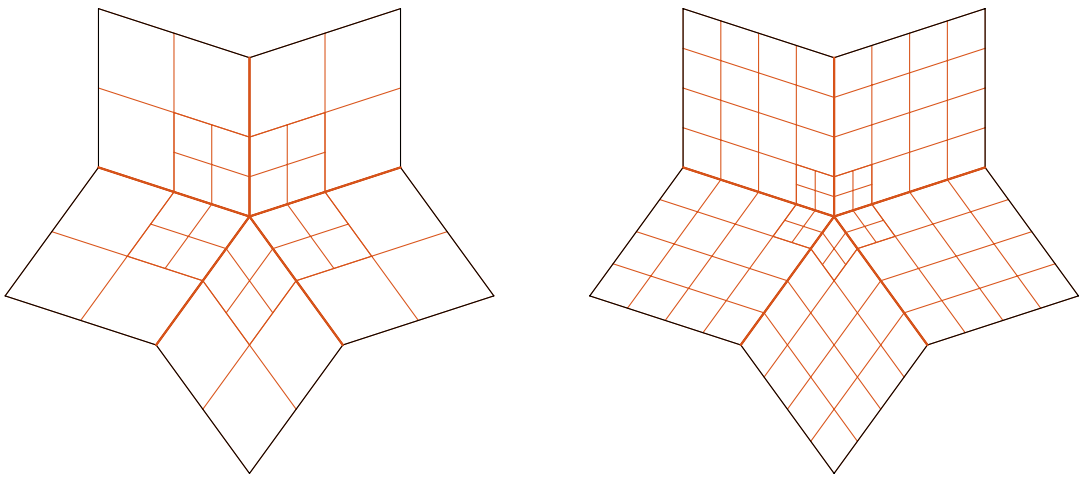

(a) $k = 0$ (b) $k = 1$

Figure 14: The construction in Section 4.3 leads to spline functions with smoothness C^2 across the black lines and C^1 across the red ones, and the above figures show how these lines of reduced regularity vary with refinement of an extraordinary point's neighborhood.

Proposition 4.2. *The spline functions N_ℓ, $\ell \in \{1, \ldots, n\} \backslash \mathcal{I}_1^v$, and $\tilde{N}_L$, $L \in \mathcal{F}^v$, form a basis for $\mathbb{S}_A^k$.*

Proof. We approach the proof by showing that the representation of the zero function should have zero coefficients. Suppose

$$\sum_{\substack{\ell=1,\ldots,n \\ \ell \notin \mathcal{I}_1^v}} c_\ell N_\ell + \sum_{i=1}^{n_{\text{ep}}} \sum_{L \in \mathcal{F}^{v,i}} \tilde{c}_L \tilde{N}_L \equiv 0 \,, \tag{4.3}$$

on all elements of the mesh. Using the same reasoning as in the proof of Proposition 3.2, the coefficients c_ℓ in Equation (4.3) must be zero for $\ell \in \mathcal{R}^v \backslash \cup_{i=1}^{n_{\text{ep}}} \mathcal{R}^{v,i}$. Subsequently, let us look at each 2^{k+1}-disk neighborhood of the ith extraordinary point (see Figure 10) separately. On such neighborhoods, all the face-based spline functions are linearly independent following the proof provided in [36].

Then, we only need to prove the collective linear independence of (a) the innermost layer of regular spline functions, (b) the outermost layer of face-based spline functions, (c) the T2 irregular spline functions, and (d) the transition spline functions, and the assertion will follow. It is sufficient to focus only on the transition elements where the supports of all these spline functions overlap. We have color-coded the transition elements in Figure 15a. For $e \in \mathcal{T}^{f,i}$, consider the full spline extraction operator constructed by the vertical concatenation of the vertex- and face-based extraction operators,

$$\bar{\boldsymbol{C}}_e = \begin{bmatrix} \boldsymbol{C}_e \\ \tilde{\boldsymbol{C}}_e \end{bmatrix} .$$

Then, on the light blue and gray transition elements in Figure 15a, $\bar{\boldsymbol{C}}_e$ is a non-singular 16×16 matrix. This implies that we have local linear independence, and for the reproduction of zero, all the coefficients of spline functions that contribute to the blue

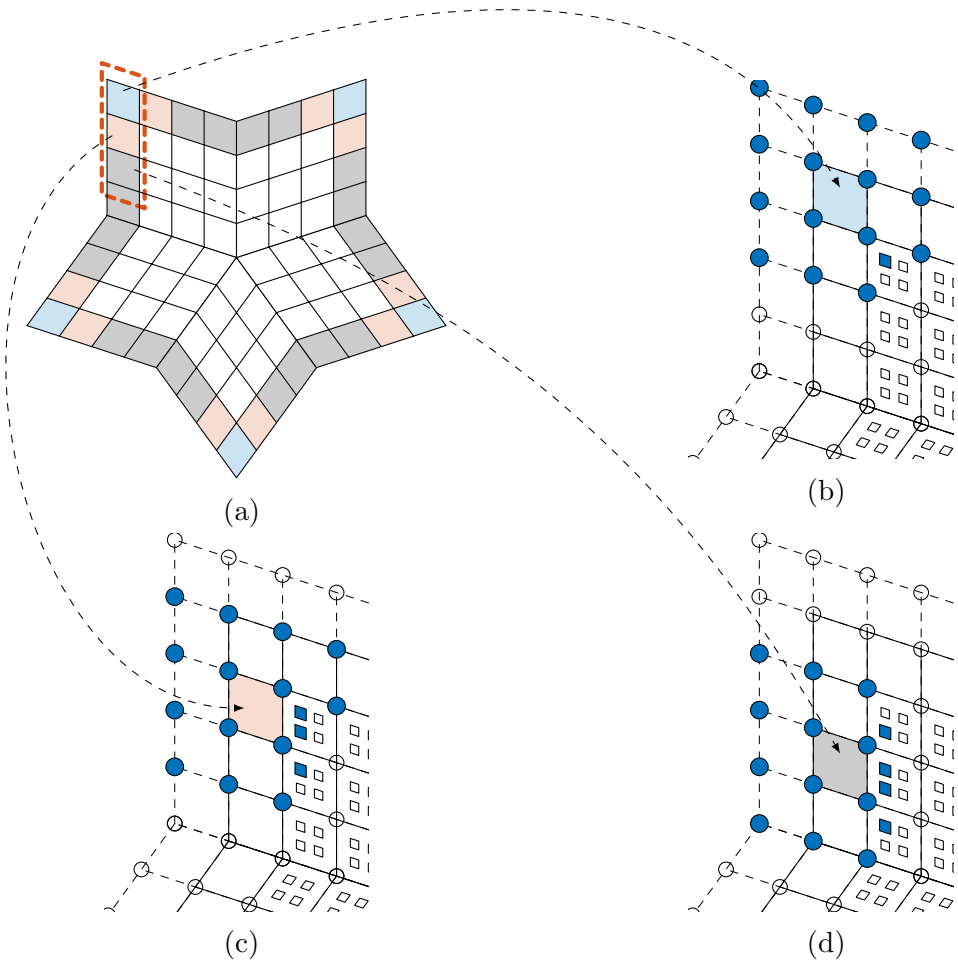

Figure 15: In Figure (a), the transition elements have been color coded as per the proof of Proposition 4.2. The spline functions non-zero over the transition elements shown in Figures (b)–(d) are associated with the control points shown in blue in each figure. Each element of the same color is treated in the same manner.

elements must vanish. In the following, we will consider the three elements encircled by the dashed line in Figure 15a. Then, the coefficients of the 16 spline functions that contribute to the light blue and gray elements in Figure 15a must vanish from the above reasoning (their control points are shown in blue in Figures 15b and 15d).

Then, if we can show that the local linear independence on the light blue and gray elements implies that the coefficients of all spline functions that contribute to the pink elements must vanish, the assertion will follow. We observe the following.

- The coefficients of all spline functions shown in Figure 15b must vanish.
- The coefficients of all spline functions contributing to the pink element are shown in Figure 15c. Since this element shares some degrees of freedom with the blue element in Figure 15b, the above observation implies that there are only 5 coefficients left on the pink element that may be non-zero. However, these too must vanish as the spline functions associated with these 5 coefficients are linear combinations of 5 Bernstein basis functions defined on the pink element, with the linear map being a 5×5 non-singular matrix by construction.

This means that all coefficients c_ℓ and $\tilde{c}_L$ in Equation (4.3) must be zero, and so the assertion follows. $\square$

4.4. Geometry representation

Propositions 4.1 and 4.2 prove that we can perform meaningful analysis using the constructed spline functions. However, recalling the goal of isogeometric analysis, we must prove that the inherited geometry $\boldsymbol{S}$ is represented exactly at all refinement levels. After discussions on equivalence of splines defined on $\mathcal{M}^k$ in Section 4.4.1, we show that the design space is contained within the analysis space at $k = 0$ in Section 4.4.3. Subsequently, in Section 4.4.4, we constructively prove that the spline spaces $\mathbb{S}_A^k$ are nested (i.e., $\mathbb{S}_A^k \subseteq \mathbb{S}_A^{k+1}$), under the assumption of idempotence of the smoothing matrices used.

Before proceeding, let us define a notational convention that considerably simplifies the following discussion. Essentially, in the rest of this section we will only consider macro quantities (extraction operators, control points, etc.). The reason for doing this is that the micro quantities can be deterministically and straightforwardly computed from the macro ones using the split-then-smoothen approach. As a result, equivalence of macro quantities implies equivalence of micro quantities and, thus, it is sufficient to consider only the former. Therefore, for instance, while discussing the restriction of vector-valued spline $\boldsymbol{S}^w$ to a Bézier element ω^e, it will suffice to consider the associated macro Bézier control points $\{\boldsymbol{B}_{pq}^e : p, q = 0, \ldots, 3\}$ only — regardless of whether ω^e is a 1-ring element or not. In particular, with some abuse of notation, we will consider the restriction of $\boldsymbol{S}^w$ to ω^e to be equivalent to the vector of associated 16 macro Bézier control points,

$$\boldsymbol{S}^w\big|_{\omega^e} \equiv [\ldots,\ \boldsymbol{B}_{p0}^e,\ \boldsymbol{B}_{p1}^e,\ \boldsymbol{B}_{p2}^e,\ \boldsymbol{B}_{p3}^e,\ \ldots]\ . \tag{4.4}$$

4.4.1. Equality of splines on $\mathcal{M}^k$

Let us make a key observation that will help us along the way. Consider two general, at least C^1, bi-cubic, vector-valued spline functions, $\boldsymbol{S}_1$ and $\boldsymbol{S}_2$, defined on $\mathcal{M}^k$. Let $\mathcal{R}^f$ contain the indices of regular elements, and consider the ith extraordinary point's

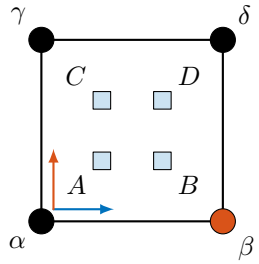

Figure 16: Indices of spline control points that contribute to the interior Bézier control points on an irregular element ω^e. T1 irregular control points are inactive. For instance, index β has been colored red to show its correspondence to a T1 irregular control point, and thus all except it contribute.

neighborhood. Let $\boldsymbol{S}_1$ and $\boldsymbol{S}_2$ be such that on ω^e, as in Equation (4.4),

$$\boldsymbol{S}_j^w\big|_{\omega^e} \equiv [\ldots,\ \boldsymbol{B}_{p0}^{e,j},\ \boldsymbol{B}_{p1}^{e,j},\ \boldsymbol{B}_{p2}^{e,j},\ \boldsymbol{B}_{p3}^{e,j},\ \ldots]\ , \qquad j = 1, 2\ .$$

If the following holds for all $i \in \{1, \ldots, n_{\text{ep}}\}$,

$$\boldsymbol{S}_1^w\big|_{\omega^e} = \boldsymbol{S}_2^w\big|_{\omega^e}\ , \qquad e \in \mathcal{R}^f\ , \tag{4.5}$$

$$\boldsymbol{B}_{pq}^{e,1} = \boldsymbol{B}_{pq}^{e,2}\ , \qquad p, q \in \{2, 3\},\ e \in \mathcal{I}^{f,i} \cup \mathcal{T}^{f,i}, \tag{4.6}$$

then the C^1 smoothness between all Bézier elements automatically ensures that,

$$\boldsymbol{S}_1 = \boldsymbol{S}_2\ .$$

In other words, if two at least C^1 spline functions defined on $\mathcal{M}^k$ are such that (a) they are equal on the regular regions of $\mathcal{M}^k$, and (b) they have equal interior Bézier control points on all irregular and transition elements, then the splines are equal. This is a re-interpretation of the well-known fact that, away from the mesh boundary, for C^1 splines the interior Bézier control points contain all the information. We will keep this observation in mind, and only work with the interior macro Bézier control points $\boldsymbol{B}_{pq}^e$, $p, q \in \{2, 3\}$, in the following discussion on the restriction of macro Bézier extractions to interior control points.

4.4.2. Restriction of macro extractions to ω^e interior

Consider the macro spline extraction operators $\boldsymbol{C}_e$ and $\tilde{\boldsymbol{C}}_e$, built in Section 4.3, and let $\boldsymbol{E}_e := (\boldsymbol{C}_e)^T$ and $\tilde{\boldsymbol{E}}_e := (\tilde{\boldsymbol{C}}_e)^T$. Let $\mathcal{P}_v^e$ contain the indices of all T2 irregular control points that lie on the corners of an irregular element ω^e, and let $\mathcal{P}_f^e$ contain

the indices of all face-based control points on ω^e. For example, with reference to Figure 16, $\mathcal{P}_v^e = \{\alpha, \gamma, \delta\}$ and $\mathcal{P}_f^e = \{A, B, C, D\}$, and β corresponds to the index of a T1 irregular control point. Let $\boldsymbol{E}_{e,0}$ and $\tilde{\boldsymbol{E}}_{e,0}$ be the restrictions of $\boldsymbol{E}_e$ and $\tilde{\boldsymbol{E}}_e$ to the interior Bézier control points on ω^e. That is, for an irregular element ω^e and a spline function $\boldsymbol{S}^w \in \left(\mathbb{S}_A^k\right)^{d+1}$ (with vertex- and face-based control points denoted by $\{\boldsymbol{P}_\ell^w : \ell \in \mathcal{P}_v^e\}$ and $\{\tilde{\boldsymbol{P}}_L^w : L \in \mathcal{P}_f^e\}$) such that,

$$\boldsymbol{S}^w\big|_{\omega^e} \equiv [\ldots,\ \boldsymbol{B}_{p0}^e,\ \boldsymbol{B}_{p1}^e,\ \boldsymbol{B}_{p2}^e,\ \boldsymbol{B}_{p3}^e,\ \ldots]\ ,$$

we have,

$$\begin{bmatrix} \boldsymbol{B}_{11}^e \\ \boldsymbol{B}_{21}^e \\ \boldsymbol{B}_{12}^e \\ \boldsymbol{B}_{22}^e \end{bmatrix} = \tilde{\boldsymbol{E}}_{e,0} \begin{bmatrix} \tilde{\boldsymbol{P}}_A^w \\ \tilde{\boldsymbol{P}}_B^w \\ \tilde{\boldsymbol{P}}_C^w \\ \tilde{\boldsymbol{P}}_D^w \end{bmatrix} + \boldsymbol{E}_{e,0} \begin{bmatrix} \boldsymbol{P}_\alpha^w \\ \boldsymbol{P}_\gamma^w \\ \boldsymbol{P}_\delta^w \end{bmatrix} = \begin{bmatrix} \tilde{s}_A & & & \\ & \tilde{s}_B & & \\ & & \tilde{s}_C & \\ & & & \tilde{s}_D \end{bmatrix} \begin{bmatrix} \tilde{\boldsymbol{P}}_A^w \\ \tilde{\boldsymbol{P}}_B^w \\ \tilde{\boldsymbol{P}}_C^w \\ \tilde{\boldsymbol{P}}_D^w \end{bmatrix} + \boldsymbol{E}_{e,0} \begin{bmatrix} \boldsymbol{P}_\alpha^w \\ \boldsymbol{P}_\gamma^w \\ \boldsymbol{P}_\delta^w \end{bmatrix}, \tag{4.7}$$

where $\tilde{s}_A$ is the scaling coefficient, computed as in Figure 13, Section 4.3, for the basis function $\tilde{N}_A$, and so on.

4.4.3. $\mathbb{S}_D \subseteq \mathbb{S}_A$

We are now in a position to show, in a constructive manner, that the design space is a subset of the analysis space at refinement level $k = 0$.

Proposition 4.3. *Let $\boldsymbol{S}^w = \sum_{\ell=1}^n \boldsymbol{P}_\ell^w M_\ell \in (\mathbb{S}_D)^{d+1}$, where $\mathbb{S}_D$ is the design space on $\mathcal{M}$. Then, there exist control points $\boldsymbol{Q}_\ell^w$ and $\tilde{\boldsymbol{Q}}_L^w$ such that,*

$$\boldsymbol{S}^w = \sum_{\substack{\ell=1,\ldots,n \\ \ell \notin \mathcal{I}_1^v}} \boldsymbol{Q}_\ell^w N_\ell + \sum_{L \in \mathcal{F}^v} \tilde{\boldsymbol{Q}}_L^w \tilde{N}_L \in (\mathbb{S}_A)^{d+1}\ . \tag{4.8}$$

Proof. As mentioned in Remark 4.2, the control point and element labels for design and analysis coincide for $k = 0$ and, thus, we will use them uniformly. We first set all the control points corresponding to regular spline basis functions to be the same for design and analysis, $\boldsymbol{Q}_\ell^w = \boldsymbol{P}_\ell^w$, $\ell \in \mathcal{R}^v$. Next, consider a 2-disk neighborhood of an extraordinary point.

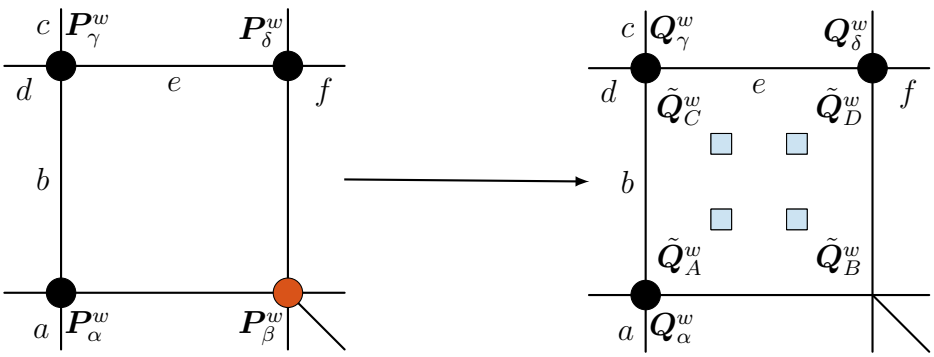

Figure 17: It is possible to exactly represent $\boldsymbol{S}^w \in (\mathbb{S}_D)^{d+1}$ as an element of the analysis space $(\mathbb{S}_A)^{d+1}$. All regular, transition, and T2 irregular control points are kept unchanged. The new face-based control points are set as linear combinations of the T1 and T2 irregular control points; see Equation (4.10).

- All transition spline basis functions for design and analysis are equivalent. Therefore, we set their control points to be equal,

$$\boldsymbol{Q}^w_\ell = \boldsymbol{P}^w_\ell \ , \qquad \ell \in \cup_{i=1}^{n_{\rm ep}} \mathcal{T}^v \ .$$

- All T2 irregular spline basis functions, restricted to transition elements, are the same for design and analysis. Therefore, we set their control points to be equal as well,

$$\boldsymbol{Q}^w_\ell = \boldsymbol{P}^w_\ell \ , \qquad \ell \in \cup_{i=1}^{n_{\rm ep}} \mathcal{I}_2^{v,i} \ .$$

- Consider a 2-disk neighborhood of an extraordinary point, and for irregular element ω^e let,

$$\boldsymbol{S}^w\big|_{\omega^e} \equiv [\ldots,\ \boldsymbol{B}^e_{p0},\ \boldsymbol{B}^e_{p1},\ \boldsymbol{B}^e_{p2},\ \boldsymbol{B}^e_{p3},\ \ldots] \ . \tag{4.9}$$

Then, set the face-based control points such that,

$$\begin{bmatrix} \boldsymbol{B}^e_{11} \\ \boldsymbol{B}^e_{21} \\ \boldsymbol{B}^e_{12} \\ \boldsymbol{B}^e_{22} \end{bmatrix} = \begin{bmatrix} \tilde{s}_A & & & \\ & \tilde{s}_B & & \\ & & \tilde{s}_C & \\ & & & \tilde{s}_D \end{bmatrix} \begin{bmatrix} \tilde{\boldsymbol{Q}}^w_A \\ \tilde{\boldsymbol{Q}}^w_B \\ \tilde{\boldsymbol{Q}}^w_C \\ \tilde{\boldsymbol{Q}}^w_D \end{bmatrix} + \boldsymbol{E}_{e,0} \begin{bmatrix} \boldsymbol{P}^w_\alpha \\ \boldsymbol{P}^w_\gamma \\ \boldsymbol{P}^w_\delta \end{bmatrix} ,$$

where the quantities are as defined in Equation (4.7) and the labels correspond to Figure 17. Note that $\tilde{s}_B = 1$. Since the left-hand side can be expressed in terms of $\boldsymbol{P}^w_\ell$, $\ell \in \{\alpha, \beta, \gamma, \delta\}$, using Equation (A.2), we obtain the following explicit

expressions for control points $\tilde{\boldsymbol{Q}}_i^w$,

$$\tilde{\boldsymbol{Q}}_A^w = \frac{b+c}{a+b+c}\boldsymbol{P}_\beta^w + \frac{a}{a+b+c}\boldsymbol{P}_\delta^w, \quad \tilde{\boldsymbol{Q}}_D^w = \frac{f}{d+e+f}\boldsymbol{P}_\alpha^w + \frac{d+e}{d+e+f}\boldsymbol{P}_\beta^w, \quad \tilde{\boldsymbol{Q}}_C^w = \boldsymbol{P}_\beta^w \ ,$$
$$\begin{aligned}\tilde{\boldsymbol{Q}}_B^w = &\left(\frac{b+c}{a+b+c}\right)\left[\left(\frac{f}{d+e+f}\right)\boldsymbol{P}_\alpha^w + \left(\frac{d+e}{d+e+f}\right)\boldsymbol{P}_\beta^w\right] \\ &+ \left(\frac{a}{a+b+c}\right)\left[\left(\frac{d+e}{d+e+f}\right)\boldsymbol{P}_\delta^w + \left(\frac{f}{d+e+f}\right)\boldsymbol{P}_\gamma^w\right] \ .\end{aligned} \tag{4.10}$$

Setting all the control points in all 2-disk neighborhoods in this manner, and following the discussion in Section 4.4.1, the assertion follows. □

4.4.4. $\mathbb{S}_A^k \subseteq \mathbb{S}_A^{k+1}$

We have just shown in Section 4.4.3 that elements of the design space are also elements of the analysis space, implying that we lose no geometric information by representing the geometry built on $\mathcal{M}$ using the design space $\mathbb{S}_D$ as an element of the analysis space $\mathbb{S}_A$. However, for this to remain so when refinements are carried out during analysis, we wish the analysis spaces $\mathbb{S}_A^k$ to form a nested sequence of spaces, i.e., $\mathbb{S}_A^k \subseteq \mathbb{S}_A^{k+1}$. In this section we explicitly outline the conditions under which such a nested sequence is obtained.

Before we begin, let us first observe the differences between Figures 6 and 10. It is clear that during isogeometric analysis, the number of rings of C^1 elements — equivalently, irregular elements — in each extraordinary point's neighborhood increase with each refinement step, while during geometric modeling, this number stays constant ($= 1$). Indeed, based on our discussion in Section 3.3.1, we decided to go for non-nested refinements for geometric modeling, and this explains the latter observation. The logic behind the former, however, is subtle and we address it next lest it get overlooked.

Observe in Figure 10, and recall from Section 4.1, that when going from refinement level k to $k+1$, the number of irregular- or C^1-element rings increases from $2^{k+1}-1$ to $2^{k+2}-1 = 2\left(2^{k+1}-1\right)+1$. That is, not only do we obtain 2 new irregular element rings by splitting the irregular elements at level k, we introduce an *additional* ring of irregular elements with each refinement step. To understand this, first note that a necessary condition for nestedness of spline spaces $\mathbb{S}_A^k$ and $\mathbb{S}_A^{k+1}$ is the following: if an

arbitrary spline $S \in \mathbb{S}_A^k$ is C^1 across a mesh edge, then the splines in $\mathbb{S}_A^{k+1}$ must be such that they can reproduce C^1 smoothness across that mesh edge. Then, looking at Figure 14, it is clear why the additional layer of C^1 elements is added. If it was not, then the smoothness between the outermost ring of elements shown in Figure 14b will be elevated to C^2 and this would clearly violate the aforementioned necessary condition for nestedness.

Proposition 4.4. *If the smoothing matrices used are idempotent, the spline spaces $\mathbb{S}_A^k$ built as in Section 4.3 are nested,*

$$\mathbb{S}_A = \mathbb{S}_A^0 \subseteq \mathbb{S}_A^1 \subseteq \mathbb{S}_A^2 \subseteq \cdots \tag{4.11}$$

Proof. The proof is constructive. Given $\boldsymbol{S}^w \in (\mathbb{S}_A^k)^{d+1}$, we will present a strategy to compute control points of its refined form, $\bar{\boldsymbol{S}}^w \in (\mathbb{S}_A^{k+1})^{d+1}$.

Let the vertex- and face-based control points for $\boldsymbol{S}^w$ and $\bar{\boldsymbol{S}}^w$ be denoted by $\{\boldsymbol{P}_\ell^w, \tilde{\boldsymbol{P}}_L^w\}$ and $\{\boldsymbol{Q}_\ell^w, \tilde{\boldsymbol{Q}}_L^w\}$, respectively. We will use the usual symbols to denote irregular, regular, etc., control point and element labels, and will differentiate the sets at level k from those at level $k+1$ by putting a horizontal bar over the latter. (One may use as a reference Figure 10 to recall how these sets vary with refinement.)

For Bézier element ω^e in $\mathcal{M}^k$, we can find the Bézier extracted representation of $\boldsymbol{S}^w$ as in Equation (4.9). Similarly, for Bézier element ω^e in $\mathcal{M}^{k+1}$ we can find the local representation of $\boldsymbol{S}^w$,

$$\boldsymbol{S}^w\big|_{\omega^e} \equiv [\ldots,\ \hat{\boldsymbol{B}}_{p0}^e,\ \hat{\boldsymbol{B}}_{p1}^e,\ \hat{\boldsymbol{B}}_{p2}^e,\ \hat{\boldsymbol{B}}_{p3}^e,\ \ldots]\ , \tag{4.12}$$

by the application of the de Casteljau algorithm. The restriction of $\bar{\boldsymbol{S}}^w$ to ω^e in $\mathcal{M}^{k+1}$ will have the same form as Equation (4.9) but with control points $\bar{\boldsymbol{B}}_{pq}^e$.

- The regular control points for $\bar{\boldsymbol{S}}^w$ are computed using the usual refinement algorithms applied to control points of $\boldsymbol{S}^w$. Therefore, we will assume that we know $\boldsymbol{Q}_\ell^w$ for $\ell \in \bar{\mathcal{R}}^v$.
- By simply requiring that $\boldsymbol{S}^w$ stay invariant in the regular regions of $\mathcal{M}^k$, we can compute $\boldsymbol{Q}_\ell^w$, $\ell \in \bar{\mathcal{T}}^{v,i} \cup \bar{\mathcal{I}}_2^{v,i}$, $i = 1, \ldots, n_{\text{ep}}$, from the control points $\boldsymbol{P}_\ell^w$, $\ell \in \mathcal{T}^{v,i} \cup \mathcal{I}_2^{v,i}$, using tensor-products of univariate knot-insertion rules (see Appendix B).

The above control points ensure that,

$$\begin{aligned} \boldsymbol{S}^w\big|_{\omega^e} &= \bar{\boldsymbol{S}}^w\big|_{\omega^e}, \qquad e \in \bar{\mathcal{R}}^f\ , \\ \hat{\boldsymbol{B}}_{pq}^e &= \bar{\boldsymbol{B}}_{pq}^e, \qquad e \in \bar{\mathcal{T}}^{f,i},\ i \in \{1, \ldots, n_{\text{ep}}\},\ p, q \in \{2, 3\}. \end{aligned}$$

Then, following our discussion in Section 4.4.1, we only need to find face-based control points $\tilde{\boldsymbol{Q}}_L$ such that,

$$\hat{\boldsymbol{B}}_{pq}^e = \bar{\boldsymbol{B}}_{pq}^e, \qquad e \in \bar{\mathcal{I}}^{f,i},\ i \in \{1, \ldots, n_{\text{ep}}\},\ p, q \in \{2, 3\}, \tag{4.13}$$

to prove that $\boldsymbol{S}^w = \bar{\boldsymbol{S}}^w$. This is easy to accomplish using Equation (4.7). For ω^e, $e \in \bar{\mathcal{I}}^{f,i}$, we compute the face-based control points using Equation (4.7),

$$\begin{bmatrix} \tilde{s}_A & & & \\ & \tilde{s}_B & & \\ & & \tilde{s}_C & \\ & & & \tilde{s}_D \end{bmatrix} \begin{bmatrix} \tilde{\boldsymbol{Q}}^w_A \\ \tilde{\boldsymbol{Q}}^w_B \\ \tilde{\boldsymbol{Q}}^w_C \\ \tilde{\boldsymbol{Q}}^w_D \end{bmatrix} = \begin{bmatrix} \hat{\boldsymbol{B}}^e_{11} \\ \hat{\boldsymbol{B}}^e_{21} \\ \hat{\boldsymbol{B}}^e_{12} \\ \hat{\boldsymbol{B}}^e_{22} \end{bmatrix} - \boldsymbol{E}_{e,0} \begin{bmatrix} \boldsymbol{P}^w_\alpha \\ \boldsymbol{P}^w_\gamma \\ \boldsymbol{P}^w_\delta \end{bmatrix} ,$$

where the quantities are as defined in Equation (4.7), and the labels refer to Figure 16. In particular, on irregular elements that do not touch transition elements, the above simplifies to,

$$[\tilde{\boldsymbol{Q}}^w_A,\ \tilde{\boldsymbol{Q}}^w_B,\ \tilde{\boldsymbol{Q}}^w_C,\ \tilde{\boldsymbol{Q}}^w_D] = [\hat{\boldsymbol{B}}^e_{11},\ \hat{\boldsymbol{B}}^e_{21}, \hat{\boldsymbol{B}}^e_{12}, \hat{\boldsymbol{B}}^e_{22}] ,$$

as all T2 irregular spline functions are identically zero, and all scaling coefficients $\tilde{s}_j$ are equal to 1. Furthermore, given that the smoothing matrices used are,

(a) built in accordance with Remark 2.1, and,

(b) idempotent, see Lemma 2.2,

then the above control-point update guarantees that geometry will stay invariant even on the 1-ring irregular elements, as proved in [36].

Then, setting all face-based control points as above, for all $i \in \{1, \ldots, n_{\text{ep}}\}$, we have satisfied the requirement posed in Equation (4.13), thereby proving that $\bar{\boldsymbol{S}}^w = \boldsymbol{S}^w$. □

The control point update procedure defined in the above proof will be referred to as $\mathcal{U}_A$-updates.

5. Numerical Tests

In this section we instantiate the abstract framework developed so far. A crucial component concerns the particular smoothing matrices used, and Section 5.1 provides valid examples that feature the linear transformations developed in [44]. The examples given in Section 5.1 can then be used to initialize the framework. Numerical tests presented in Sections 5.2 and 5.3 for applications aimed towards geometric modeling and analysis, respectively.

5.1. Examples of smoothing matrices

As a first step towards analyzing the efficacy of the proposed setup, we borrow from [44] two examples of smoothing matrices: Π^+, that has non-negative entries, and Π°,

that is idempotent. Both these matrices have the following block structure,

$$\Pi = \begin{bmatrix} \Pi_1 & \Pi_2 & \Pi_3 \\ \Pi_4 & \Pi_5 & \Pi_6 \\ \Pi_7 & \Pi_8 & \Pi_9 \end{bmatrix} , \tag{5.1}$$

where each submatrix Π_i is a $\mu \times \mu$ circulant (or cyclic) matrix, i.e., there exist vectors $\boldsymbol{p}_i$ of length μ such that

$$(\Pi_i)_{jk} = (\boldsymbol{p}_i)_{(j-k) \bmod \mu}, \quad j, k = 0, 1, \ldots, \mu - 1 . \tag{5.2}$$

The particular choices of vectors $\boldsymbol{p}_i$ that yield Π^+ and Π° are provided in the following examples.

Example 5.1 (Π^+; non-negative entries)**.** *We construct* Π^+ *using the following vectors and Equations* (5.1) *and* (5.2)*,*

$$\begin{aligned} (\boldsymbol{p}_1)_j &= (\boldsymbol{p}_4)_j = (\boldsymbol{p}_7)_j = 0 , \\ (\boldsymbol{p}_2)_j &= (\boldsymbol{p}_3)_j = \frac{1}{2\mu} , \\ (\boldsymbol{p}_5)_j &= (\boldsymbol{p}_9)_j = \frac{1}{2\mu} \left(1 + \cos(j\phi_\mu)\right) , \\ (\boldsymbol{p}_6)_j &= \frac{1}{2\mu} \left(1 + \cos(2\psi + j\phi_\mu)\right) , \\ (\boldsymbol{p}_8)_j &= \frac{1}{2\mu} \left(1 + \cos(2\psi - j\phi_\mu)\right) , \end{aligned} \tag{5.3}$$

where $\phi_\mu := 2\pi/\mu$*,* $\psi := \arg\left((1 + \iota\beta \sin(\phi_\mu))e^{-\iota\phi_\mu/2}\right)$*, and we choose* $\beta = 0.4$*. It is easy to verify that* Π^+ *has only non-negative entries. Note that* Π^+ *is not idempotent.*

Example 5.2 (Π°; idempotent)**.** *To construct* Π°*, we use the following vectors and, again, Equations* (5.1) *and* (5.2)*,*

$$\begin{aligned} (\boldsymbol{p}_1)_j &= (\boldsymbol{p}_2)_j = (\boldsymbol{p}_3)_j = (\boldsymbol{p}_4)_j = (\boldsymbol{p}_7)_j = \frac{1}{3\mu} , \\ (\boldsymbol{p}_5)_j &= (\boldsymbol{p}_9)_j = \frac{1}{3\mu} \left(1 + 3\cos(j\phi_\mu)\right) , \\ (\boldsymbol{p}_6)_j &= \frac{1}{3\mu} \left(1 + 3\cos(2\psi + j\phi_\mu)\right) , \\ (\boldsymbol{p}_8)_j &= \frac{1}{3\mu} \left(1 + 3\cos(2\psi - j\phi_\mu)\right) , \end{aligned} \tag{5.4}$$

where $\phi_\mu := 2\pi/\mu$, $\psi := \arg\left((1+\iota\beta\sin(\phi_\mu))e^{-\iota\phi_\mu/2}\right)$, *and we choose* $\beta = 0.4$. *It is easy to verify that* Π° *is idempotent, but does have negative entries.*

5.2. Geometric modeling

We start off our discussion of applications geared toward geometric modeling by looking at the basis functions associated with irregular control points on an example configuration. Thereafter, we present examples of unstructured surfaces built using the design space from Section 3.2. Lastly, refinement studies demonstrate that, while the geometries do not stay invariant, the measured discrepancy is very small.

5.2.1. Examples of irregular spline functions

Let us first consider examples of irregular spline functions built in accordance with Section 3.2. These are shown in Figure 18 and correspond to,

- left column: an irregular control point that does not share an edge with the extraordinary point (Figure 18a),
- middle column: an irregular control point that shares an edge with the extraordinary point (Figure 18b), and
- right column: the extraordinary point (Figure 18c).

The second row shows spline functions built using the smoothing matrix Π^+, and these are observed to be non-negative in accordance with Proposition 3.1. On the other hand, the spline functions built using Π° are shown in the third row and, while they look almost the same as those in the second row, they are *slightly* negative (except the one in Figure 18i); the minimum was observed to be of order -10^{-3}. Therefore, to underscore the regions where the conditions of non-negativity are violated, the last row shows the contour plots for the splines in the row above from -10^{-3} to 10^{-3} by 10^{-4}.

5.2.2. Surface obstacle course

Using control nets from the SurfLab surface obstacle course [1], we applied the construction from Section 3.2 to perform a C^1 completion around the extraordinary

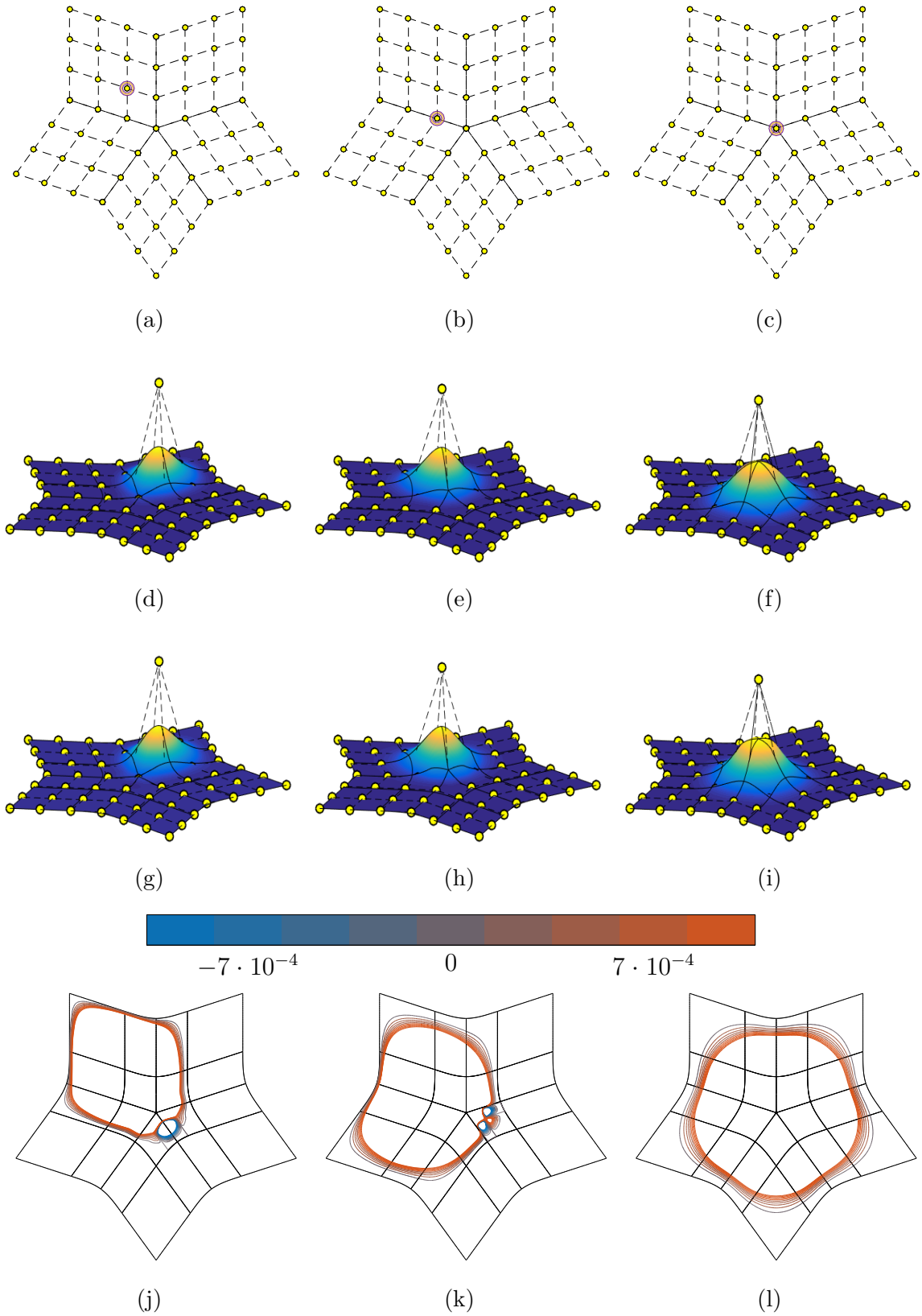

Figure 18: Figures (d), (e), (f) show examples of spline functions built using Π^+ corresponding to (a) an irregular control point that shares a face but not an edge with the extraordinary point, (b) an irregular control point that shares an edge with the extraordinary point, and (c) the extraordinary point, respectively. Similarly, Figures (g), (h) and (i) show the spline functions built using Π°. Figures (j), (k) and (l) show contours from -10^{-3} to 10^{-3} by 10^{-4} corresponding to the splines in (g), (h) and (l), respectively. It can be observed that the use of Π° leads to violation of non-negativity. (Note that the spline in (i) is non-negative.)

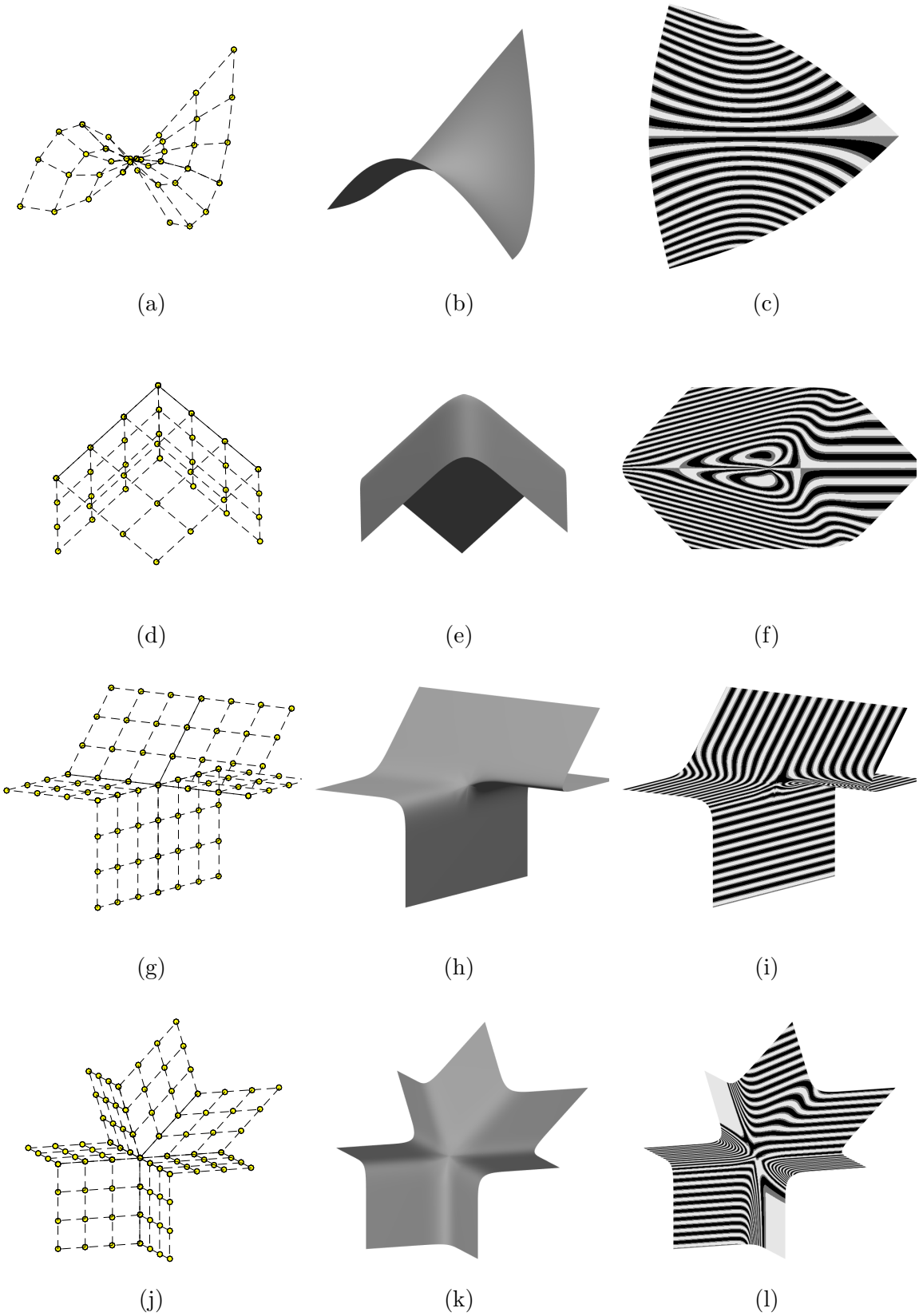

Figure 19: The quadrilateral control nets in the left column are used for constructing the surfaces in the middle column. The shaded surfaces are provided in the middle column, and the right column shows the highlight line distribution over each surface.

point. Figure 19 shows the control nets used in the left column, the surfaces constructed in the middle column, and the highlight line distributions on these surfaces in the last column. As a result of the C^1 construction, the highlight lines cannot be expected to be smooth in the extraordinary point neighborhoods, but the non-smoothness is limited to a very small region as a result of the 2×2 split applied to the 1-ring elements. While it is possible to optimize the parameters of the smoothing matrix for a given control net in order to improve upon the highlight line distribution in the extraordinary point's neighborhood, this was not a direction explored here.

Note that all the examples shown have been built using the smoothing matrix Π^+. As should be evident from Figure 18, using Π° leads to similar results (not shown), with the difference that worse highlight lines were observed near extraordinary points, a possible reason being the undulations due to sign changes that were observed in Figures 18j and 18k.

Remark 5.1. *In the following sections, we will only present results obtained using Π^+. The results obtained for all (design and analysis) numerical tests presented in this work differed only minutely when Π° was used, and in order to avoid confusion we omit the latter. Both Π^+ and Π° were observed to yield spline spaces demonstrating excellent approximation results, and therefore non-negative basis functions and better shape properties justify our decision to focus on the former.*

5.2.3. Refinements and geometric consistency

In this section we employ the $\mathcal{U}_D$-update procedure, proposed in Section 3.3.3, for refining surfaces built using the design space, and test its robustness by quantifying the geometric consistency errors such a non-nested refinement scheme introduces. The setup for our numerical tests is as follows.

- Valence: We consider meshes containing single extraordinary points of valence $\mu = 3,\ 5,\ 6$ and 7.
- Knot spans: Referring to Figure 20, we consider the following three configurations:
    - Case 1: all red and blue spoke edges have equal knot spans,

- Case 2: the blue spoke edge knot spans are 10 times smaller than the knot spans of the red ones, and,
- Case 3: the blue spoke edge knot spans are 10 times larger than the knot spans of the red ones.

The knot spans transversal to the outermost boundary are all zero, indicating open knot vectors. All other knot spans are defined by the rule that, on each face, opposite knot spans must be equal.

- Elements: The initial meshes have $4 \times \mu$ elements at level 0.
- Control points: in the xy-plane, the control point positions coincide with the mesh vertices shown in Figure 20. In particular, the extraordinary points are located at $(0, 0)$, and the meshes were scaled such that, starting from $(0, 0)$ and moving in the direction of spoke edges, the farthest control points encountered are unit distance from $(0, 0)$. The initial surface for each test case, $\boldsymbol{S}_0$, is created by setting the heights of the control points to 0 except for the control point associated with the extraordinary point, which is set to 1.
- Refinements: We refine the mesh according to $\mathcal{U}_D$-updates, thereby computing the control points defining the refined surface that, as we will see, maintains a good approximation of the initial surface, $\boldsymbol{S}_0$. The initial surfaces are refined a maximum of 3 times and, denoting the surfaces at level k with $\boldsymbol{S}_k$, we compare $\boldsymbol{S}_i$ to $\boldsymbol{S}_j$ for $i, j \in \{0, 1, 2, 3\}$.

The distance between surfaces $\boldsymbol{S}_i$ and $\boldsymbol{S}_j$ is measured in the L^2 and L^∞ norms, and the measures are denoted by $\text{dist}(\boldsymbol{S}_i, \boldsymbol{S}_j)_2$ and $\text{dist}(\boldsymbol{S}_i, \boldsymbol{S}_j)_\infty$, respectively. The results for the different test cases are tabulated in Tables 1, 2 and 3. In practice, we observe geometric consistency errors that are an order of magnitude smaller than the non-nested refinements used for T-splines [60]. The dynamic weighted refinements proposed in [60] leads to errors comparable to our method, albeit our method has the advantage of being simple in concept and implementation.

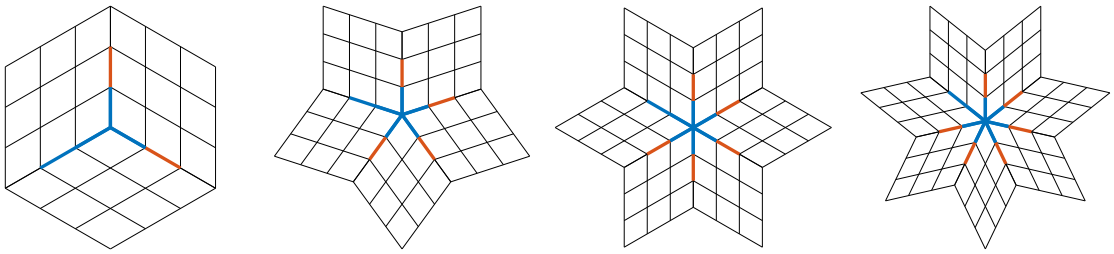

(a) Valence 3 (b) Valence 5 (c) Valence 6 (d) Valence 7

Figure 20: The initial meshes on which geometric consistency tests are performed. The knot spans assigned to the edges in blue and red are varied to simulate differing surfaces; see Section 5.2.3 for details. For generating $\boldsymbol{S}^0$, the control point positions in the xy-plane correspond to the mesh vertices shown in the figures. In the z-direction, in each setup, the height for the extraordinary point is set to 1 and for all other control points it is set to 0. The outermost knot spans are all equal to 0.

Valence	$\text{dist}(\cdot,\cdot)_2$				$\text{dist}(\cdot,\cdot)_\infty$			
	$(\boldsymbol{S}_0, \boldsymbol{S}_1)$	$(\boldsymbol{S}_1, \boldsymbol{S}_2)$	$(\boldsymbol{S}_2, \boldsymbol{S}_3)$	$(\boldsymbol{S}_0, \boldsymbol{S}_3)$	$(\boldsymbol{S}_0, \boldsymbol{S}_1)$	$(\boldsymbol{S}_1, \boldsymbol{S}_2)$	$(\boldsymbol{S}_2, \boldsymbol{S}_3)$	$(\boldsymbol{S}_0, \boldsymbol{S}_3)$
3	1.35e-03	2.55e-04	3.47e-05	1.44e-03	7.56e-03	2.69e-03	1.03e-03	7.98e-03
5	4.57e-03	8.94e-04	1.69e-04	5.05e-03	1.39e-02	5.24e-03	1.89e-03	1.56e-02
6	5.65e-03	1.12e-03	2.21e-04	6.28e-03	1.64e-02	5.95e-03	2.05e-03	1.82e-02
7	6.41e-03	1.28e-03	2.52e-04	7.15e-03	1.79e-02	6.33e-03	2.20e-03	2.00e-02

Table 1: Geometric consistency errors for Case 1 knot spans (Blue : Red :: 1 : 1) when surfaces are refined using $\mathcal{U}_D$-updates during the design phase.

Valence	$\text{dist}(\cdot,\cdot)_2$				$\text{dist}(\cdot,\cdot)_\infty$			
	$(\boldsymbol{S}_0, \boldsymbol{S}_1)$	$(\boldsymbol{S}_1, \boldsymbol{S}_2)$	$(\boldsymbol{S}_2, \boldsymbol{S}_3)$	$(\boldsymbol{S}_0, \boldsymbol{S}_3)$	$(\boldsymbol{S}_0, \boldsymbol{S}_1)$	$(\boldsymbol{S}_1, \boldsymbol{S}_2)$	$(\boldsymbol{S}_2, \boldsymbol{S}_3)$	$(\boldsymbol{S}_0, \boldsymbol{S}_3)$
3	4.22e-04	9.13e-05	1.61e-05	4.29e-04	6.68e-03	2.59e-03	1.43e-03	6.58e-03
5	8.54e-04	1.73e-04	5.07e-05	9.12e-04	1.30e-02	2.93e-03	2.53e-03	1.33e-02
6	9.79e-04	1.93e-04	5.69e-05	1.06e-03	1.55e-02	3.32e-03	2.67e-03	1.59e-02
7	1.06e-03	2.14e-04	6.06e-05	1.16e-03	1.77e-02	4.03e-03	2.85e-03	1.85e-02

Table 2: Geometric consistency errors for Case 2 knot spans (Blue : Red :: 1 : 10) when surfaces are refined using $\mathcal{U}_D$-updates during the design phase.

5.2.4. Special case: Bisection and uniform knot spans

In the special case when all 2-disk knot spans are uniform and are bisected during refinement, $\mathcal{U}_D$-updates simplify greatly. As part of this procedure, while the 1-ring control points are always computed in accordance with tensor-product knot insertion rules, the update rule for the ith extraordinary point, $\boldsymbol{P}^w_{\text{ep}}$, of valence $\mu_i \neq 4$ reduces to the following when Π^+ is used,

$$\boldsymbol{P}^{w,k+1}_{\text{ep}} = \frac{51}{112}\boldsymbol{P}^{w,k}_{\text{ep}} + \frac{3}{7\mu_i}\sum_{\ell\in\bar{\mathcal{I}}^{v,i}_2}\boldsymbol{P}^{w,k}_{\ell} + \frac{13}{112\mu_i}\sum_{\ell\in\hat{\mathcal{I}}^{v,i}_2}\boldsymbol{P}^{w,k}_{\ell}\ , \tag{5.5}$$

where $\mathcal{I}^{v,i}_2$ contains the indices of all T2 irregular control points, $\bar{\mathcal{I}}^{v,i}_2$ contains indices of those T2 irregular control points that share an edge with $\boldsymbol{P}^w_{\text{ep}}$, and $\hat{\mathcal{I}}^{v,i}_2 := \mathcal{I}^{v,i}_2 \backslash \bar{\mathcal{I}}^{v,i}_2$. Similarly, when Π° is used the update rule simplifies to the following,

$$\boldsymbol{P}^{w,k+1}_{\text{ep}} = \frac{31}{64}\boldsymbol{P}^{w,k}_{\text{ep}} + \frac{3}{8\mu_i}\sum_{\ell\in\bar{\mathcal{I}}^{v,i}_2}\boldsymbol{P}^{w,k}_{\ell} + \frac{9}{64\mu_i}\sum_{\ell\in\hat{\mathcal{I}}^{v,i}_2}\boldsymbol{P}^{w,k}_{\ell}\ . \tag{5.6}$$

Proposition 5.1. *In the absence of T-junctions and when all knot spans in $\mathcal{M}$ are uniform, we are essentially working with uniform B-splines. Then, global uniform refinements coupled with $\mathcal{U}_D$-updates define a subdivision scheme that is a C^2_1 variant of the Catmull–Clark scheme. That is, the limit surface obtained according to such update procedure is C^2 everywhere, except at extraordinary points where it is C^1.*

Proof. The proof follows straightforwardly from [39, Theorem 6.1] and Equations (5.5) and (5.6). □

5.3. Isogeometric analysis

We test the numerical behavior of the analysis spaces constructed in Section 4.3 using Π^+ as the smoothing matrix. In order to do so, we solve function approximation, Poisson, and biharmonic problems in Section 5.3.1. Subsequently, in Section 5.3.2 we present two application-based examples governed by fourth-order PDEs: the Scordelis–Lo roof, and spinodal decomposition of a binary fluid on the surface of a double-doughnut.

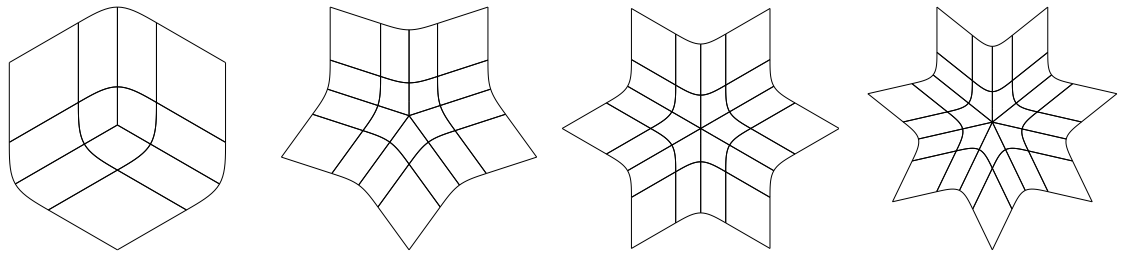

(a) Valence 3 (b) Valence 5 (c) Valence 6 (d) Valence 7

Figure 21: The computational domains at the coarsest level of refinement used for benchmarking a manufactured solution.

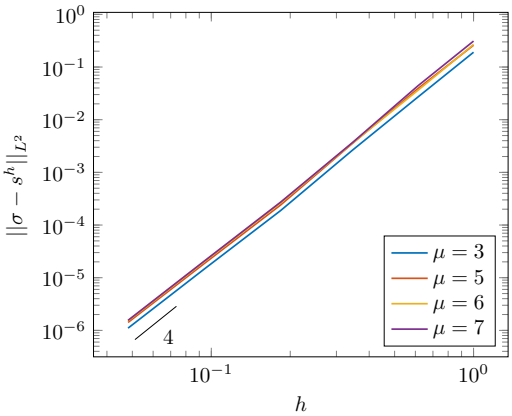

(a) Function approximation, L^2

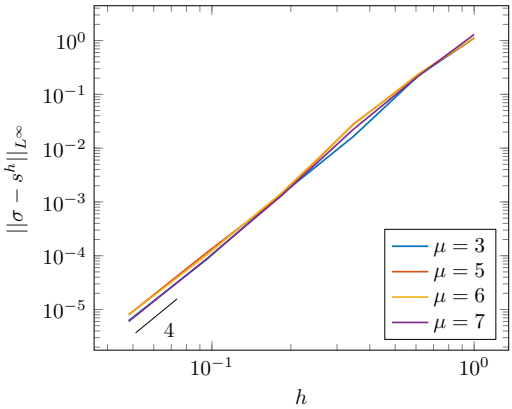

(b) Function approximation, L^∞

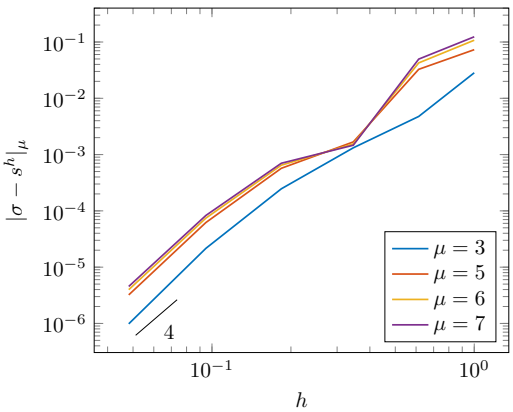

(c) Function approximation, EP

Figure 22: Figures (a) and (b) show the error convergence rates in L^2 and L^∞ norms, while (c) shows the error convergence rates at the extraordinary point for the function approximation problem in Equation (5.8).

Valence	$\text{dist}(\cdot,\cdot)_2$				$\text{dist}(\cdot,\cdot)_\infty$			
	$(\boldsymbol{S}_0, \boldsymbol{S}_1)$	$(\boldsymbol{S}_1, \boldsymbol{S}_2)$	$(\boldsymbol{S}_2, \boldsymbol{S}_3)$	$(\boldsymbol{S}_0, \boldsymbol{S}_3)$	$(\boldsymbol{S}_0, \boldsymbol{S}_1)$	$(\boldsymbol{S}_1, \boldsymbol{S}_2)$	$(\boldsymbol{S}_2, \boldsymbol{S}_3)$	$(\boldsymbol{S}_0, \boldsymbol{S}_3)$
3	1.76e-03	3.56e-04	5.68e-05	1.85e-03	9.23e-03	3.29e-03	1.50e-03	1.00e-02
5	5.05e-03	1.24e-03	2.89e-04	5.68e-03	2.01e-02	5.92e-03	2.71e-03	2.15e-02
6	6.29e-03	1.56e-03	3.83e-04	7.16e-03	2.34e-02	6.81e-03	2.90e-03	2.51e-02
7	7.17e-03	1.81e-03	4.43e-04	8.22e-03	2.57e-02	7.54e-03	3.12e-03	2.78e-02

Table 3: Geometric consistency errors for Case 3 knot spans (Blue : Red :: 10 : 1) when surfaces are refined using $\mathcal{U}_D$-updates during the design phase.

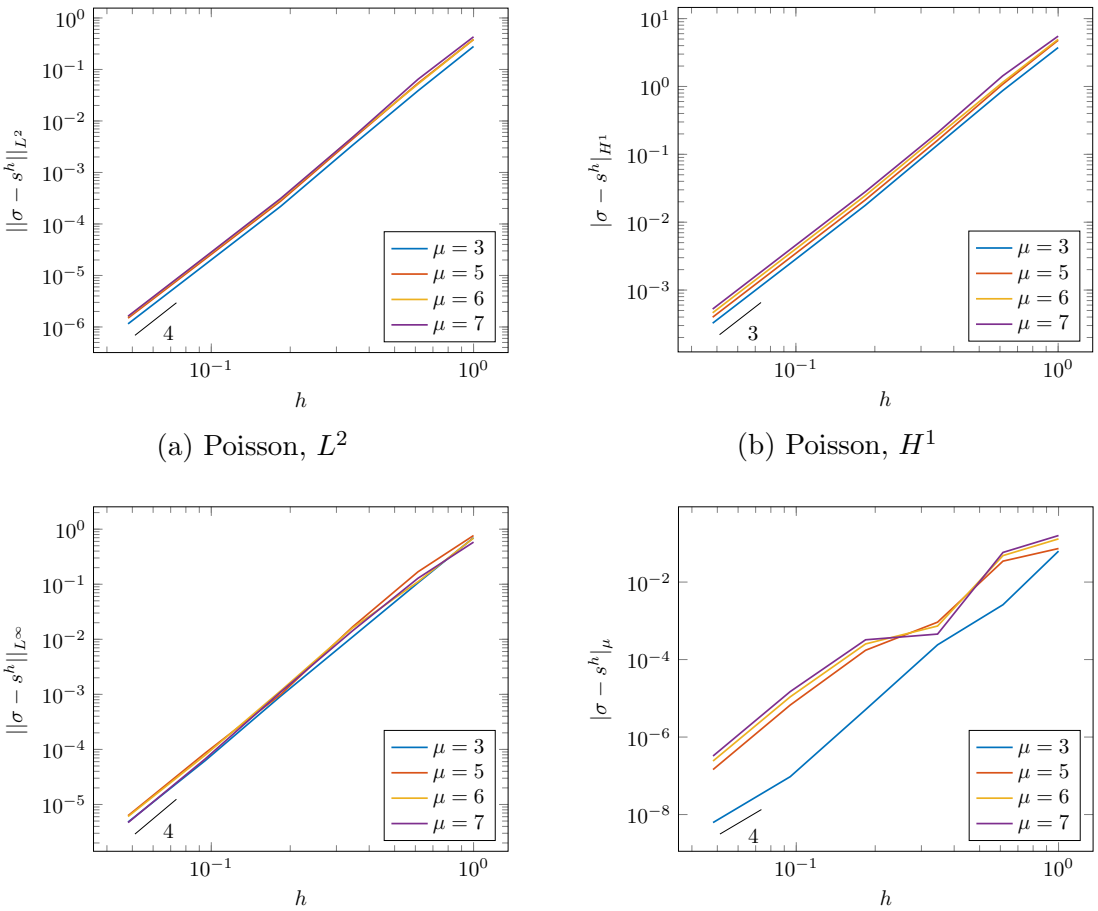

(a) Poisson, L^2

(b) Poisson, H^1

(c) Poisson, L^∞

(d) Poisson, EP

Figure 23: Figures (a)–(c) show the error convergence rates in L^2, H^1 and L^∞ norms for the Poisson problem in Equation (5.9), while the error convergence rates at the extraordinary point are shown in Figure (d) for the same.

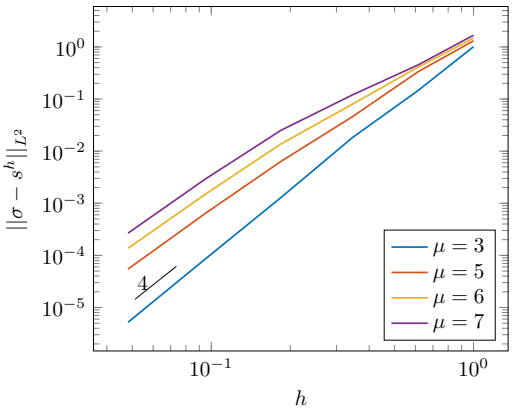

(a) Biharmonic, L^2

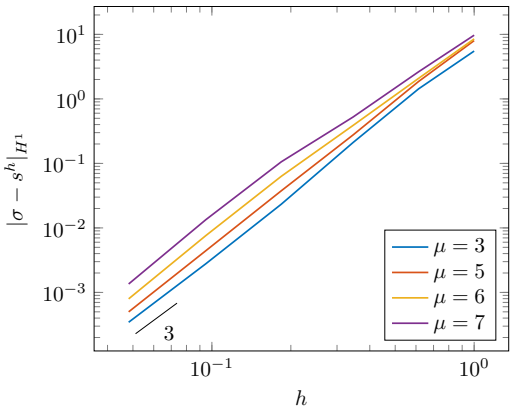

(b) Biharmonic, H^1

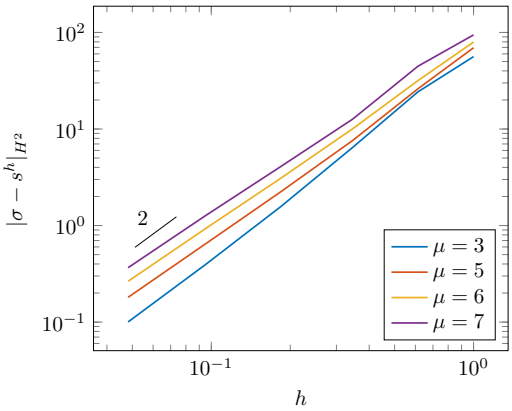

(c) Biharmonic, H^2

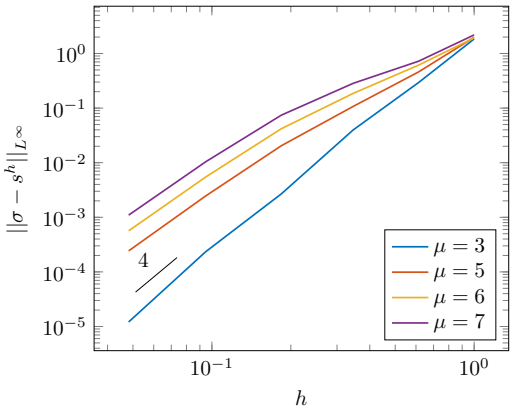

(d) Biharmonic, L^∞

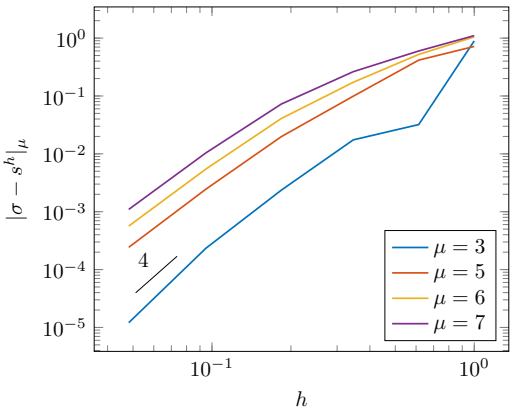

(e) Biharmonic, EP

Figure 24: Figures (a)–(e) show the error convergence rates in L^2, H^1, H^2, L^∞ norms and at the extraordinary point for the biharmonic problem in Equation (5.10).

5.3.1. Benchmarking using manufactured solutions

In order to benchmark the approach using manufactured solutions, we solved function approximation, Poisson, and biharmonic problems with the function $\sigma(u, v)$,

$$\sigma(u, v) = \sin\left(2\pi\left(u + \frac{1}{3}\right)\right)\sin\left(2\pi\left(v + \frac{1}{5}\right)\right), \quad (u,\ v) \in \Omega\ , \tag{5.7}$$

as the exact solution defined on the computational domain Ω. The following trial and test function spaces were used for the Poisson and biharmonic problems,

$$\mathcal{S}_0 := \left\{s^h \in \mathbb{S}_A : s^h = s_0^h \text{ on } \Gamma\right\}\ , \qquad \mathcal{V}_0 := \left\{w^h \in \mathbb{S}_A : w^h = 0 \text{ on } \Gamma\right\}\ ,$$
$$\mathcal{S}_1 := \left\{s^h \in \mathcal{S}_0 : s^h_{,\boldsymbol{n}} = s^h_{1,\boldsymbol{n}} \text{ on } \Gamma\right\}\ , \qquad \mathcal{V}_1 := \left\{w^h \in \mathcal{V}_0 : w^h_{,\boldsymbol{n}} = 0 \text{ on } \Gamma\right\}\ ,$$

where $\Gamma = \partial\Omega$ is the boundary of Ω, $\boldsymbol{n}$ is the unit normal to Γ, $a_{,\boldsymbol{n}} := \nabla a \cdot \boldsymbol{n}$, and $s_0^h \in \mathbb{S}_A$ and $s_1^h \in \mathcal{S}_0$ are defined such that,

$$\int_\Gamma w^h s_0^h\ d\Gamma = \int_\Gamma w^h \sigma\ d\Gamma\ , \qquad \forall w^h \in \mathbb{S}_A,\ w^h \neq 0 \text{ on } \Gamma\ ,$$
$$\int_\Gamma w^h_{,\boldsymbol{n}} s^h_{1,\boldsymbol{n}}\ d\Gamma = \int_\Gamma w^h_{,\boldsymbol{n}} \sigma^h_{,\boldsymbol{n}}\ d\Gamma\ , \qquad \forall w^h \in \mathbb{S}_A,\ w^h_{,\boldsymbol{n}} \neq 0 \text{ on } \Gamma\ .$$

Then, the following three problems were solved.

$$\mathrm{P}_1 : \text{Find } s^h \in \mathbb{S}_A : \qquad \int_\Omega w^h s^h\ d\Omega = \int_\Omega w^h \sigma\ d\Omega\ , \qquad \forall w^h \in \mathbb{S}_A\ , \tag{5.8}$$

$$\mathrm{P}_2 : \text{Find } s^h \in \mathcal{S}_0 : \qquad \int_\Omega \nabla w^h \cdot \nabla s^h\ d\Omega = -\int_\Omega w^h \Delta\sigma\ d\Omega\ , \qquad \forall w^h \in \mathcal{V}_0\ , \tag{5.9}$$

$$\mathrm{P}_3 : \text{Find } s^h \in \mathcal{S}_1 : \qquad \int_\Omega \Delta w^h \Delta s^h\ d\Omega = \int_\Omega w^h \Delta^2\sigma\ d\Omega\ , \qquad \forall w^h \in \mathcal{V}_1\ . \tag{5.10}$$

Gaussian quadrature of order 4 was used on interior element of the mesh, while on the boundary elements Gaussian quadrature of order 9 was used.

To begin benchmarking, we first considered meshes containing a single extraordinary point. The extraordinary points were all placed at the origin $(0, 0)$, and we considered valences 3, 5, 6 and 7. The rest of the control points used to build these

planar domains were placed at the vertex locations shown in Figure 20. Additionally, the meshes were scaled such that, starting from $(0, 0)$ and moving in the direction of spoke edges, the farthest control points encountered are unit distance from $(0, 0)$. The corresponding computational domains at the coarsest level of refinement are shown in Figure 21. The error convergence rates, as the meshes are globally and uniformly refined using $\mathcal{U}_A$-updates from 4.4.4, are shown in Figures 22, 23 and 24 for all the cases. The following can be observed:

- The error convergence rates are optimal for the function approximation and Poisson problems for all test cases in L^2, H^1 and L^∞ norms.
- For the biharmonic problem, and the valence 3 domain shown in Figure 21a, the error convergence rates in L^2, H^1, H^2 and L^∞ norms are optimal.
- For the biharmonic problem, and extraordinary points with $\mu > 3$, the error convergence rates, while optimal in the H^1 norm, are *slightly* sub-optimal in L^2 (≥ 3.6), H^2 (≥ 1.8), and L^∞ (≥ 3.4) norms. We conjecture that the rates will converge towards optimal ones with refinement. However, we were unable to verify this conjecture because the high condition numbers of system matrices for subsequent refinement levels ($> 10^{16}$) make the round-off errors dominate the convergence rates; similar behavior was noticed when Π° was used. It is usually difficult to verify optimal error convergence rates numerically in the presence of conditioning issues; see [21] for example.

It should be noted that since Π^+ is not idempotent, its use as the smoothing operator leads to slight variations in geometries during refinement; indeed, from Proposition 4.4, $\mathcal{U}_A$-updates only guarantee invariant geometry when idempotent smoothing operators are used. Nevertheless, in practice, we have observed the variations to be very small and these have been tabulated in Table 4 for the analysis tests corresponding to Figure 21. The geometric consistency errors have been presented only for the first three levels of refinement as the trend is obvious from the data.

Remark 5.2. *The geometric consistency errors shown in Table 4 are very small, and we did not observe any adverse effects on our computations because of them. Nevertheless, it is possible to formulate refinement procedures that lead to a monotone reduction in dist($\boldsymbol{S}_0, \boldsymbol{S}_j$) with increasing j. This could be achieved, conceptually, by referring back to $\boldsymbol{S}_0$ (instead of $\boldsymbol{S}_j$) for the computation of control points that define $\boldsymbol{S}_{j+1}$. An efficient implementation of such an update procedure would only require storing the Bézier extracted 1-ring elements of $\boldsymbol{S}_0$.*

Next, we employed a square mesh containing two extraordinary points of valence 3 and valence 5. The mesh defines the computational domain $\Omega = [0,\ 1]^2$, and is shown in Figure 25a. The problems solved are the same ones from before; see Equations (5.8), (5.9) and (5.10). The error convergence rates for the solutions obtained on this multi-EP mesh are shown in Figure 25b (function approximation); Figure 25c (Poisson); and Figure 25d (biharmonic). The error convergence rates are, once again, in accordance with the observations made above for the single-EP meshes.

Linear elasticity. As a final benchmark, we perform a standard patch test [19] for the geometry in Figure 25a. The objective of this test is to ensure that an arbitrary "patch" of elements can reproduce constant strain states exactly. For this purpose, we impose the exact displacement field,

$$u(x, y) = x/3 + y/5 + 1 \ , \qquad v(x, y) = x - y/2 - 2 \ , \tag{5.11}$$

on the boundary of our computational domain and solve the equations of linear elasticity. The material is assumed to be homogeneous and isotropic, and we choose $E = 10^5$ as the Young's modulus and $\nu = 0.3$ as the Poisson's ratio. As stated in Remark 1.3, as a consequence of isogeometric compatibility, i.e. $\mathbb{S}_D \subset \mathbb{S}_A$, and the properties of our spline spaces, we expect exact satisfaction of the patch test, and this is precisely what we observe. The computed displacement fields on the geometry, u^h and v^h, are shown in Figures 26a and 26b; the pointwise error,

$$e(x, y) := \left((u(x, y) - u^h(x, y))^2 + (v(x, y) - v^h(x, y))^2\right)^{1/2} \ ,$$

was observed to be of the order of 10^{-16} everywhere on the geometry, thus implying exact reproduction of the linear displacement field and satisfaction of the patch test.

Valence	$\text{dist}(\cdot,\cdot)_2$				$\text{dist}(\cdot,\cdot)_\infty$			
	$(\boldsymbol{S}_0, \boldsymbol{S}_1)$	$(\boldsymbol{S}_1, \boldsymbol{S}_2)$	$(\boldsymbol{S}_2, \boldsymbol{S}_3)$	$(\boldsymbol{S}_0, \boldsymbol{S}_3)$	$(\boldsymbol{S}_0, \boldsymbol{S}_1)$	$(\boldsymbol{S}_1, \boldsymbol{S}_2)$	$(\boldsymbol{S}_2, \boldsymbol{S}_3)$	$(\boldsymbol{S}_0, \boldsymbol{S}_3)$
3	5.03e-05	1.44e-06	3.65e-08	5.03e-05	1.24e-03	2.23e-04	3.84e-05	1.24e-03
5	1.69e-04	6.02e-06	1.66e-07	1.69e-04	2.17e-03	4.34e-04	6.49e-05	2.17e-03
6	2.01e-04	7.64e-06	2.16e-07	2.01e-04	2.39e-03	4.91e-04	6.91e-05	2.39e-03
7	2.20e-04	8.78e-06	2.52e-07	2.20e-04	2.49e-03	5.26e-04	7.39e-05	2.49e-03

Table 4: Geometric consistency errors introduced when performing analysis on meshes built using Π^+, and shown in Figure 21; $\mathcal{U}_A$-updates are used for refinement.

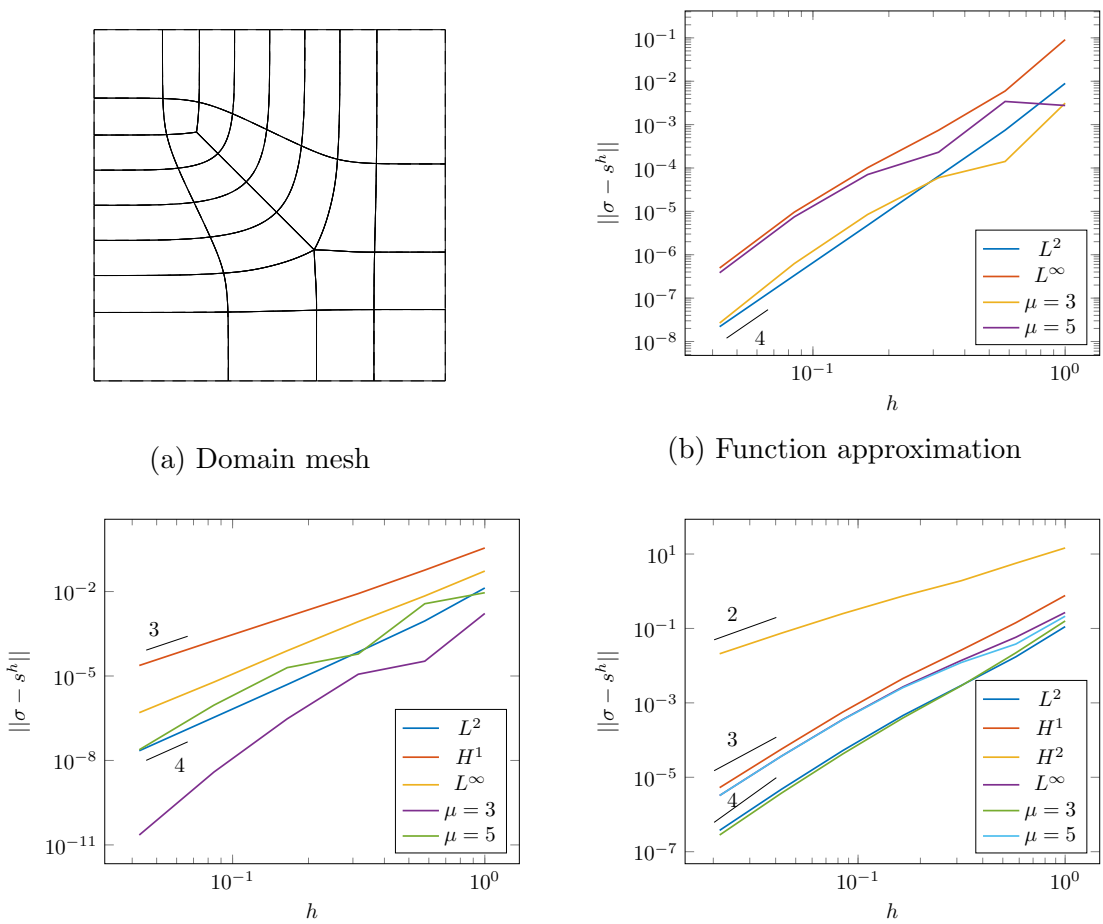

(a) Domain mesh

(b) Function approximation

(c) Poisson

(d) Biharmonic

Figure 25: Figure (a) shows the mesh used at the coarsest level of refinement, and Figures (b), (c) and (d) show the solution convergence for the projection problems in Equations (5.8), (5.9) and (5.10), respectively. The errors at the extraordinary points are indicated by $\mu = 3$ and $\mu = 5$.

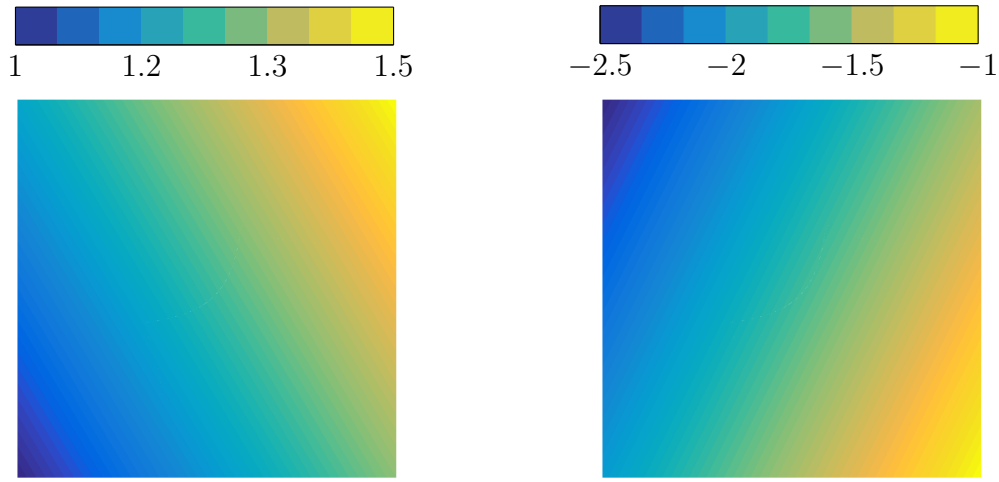

(a) $u^h(x, y)$ (b) $v^h(x, y)$

Figure 26: Results of a patch test. Exact displacement field given in Equation (5.11) is imposed on the boundaries of the geometry in Figure 25a, and the computed displacement fields, u^h and v^h, are shown in Figures (a) and (b). The computed displacement field matches the exact displacement field given in Equation 5.11 up to machine precision ($\approx 10^{-16}$), thus implying satisfaction of the patch test.

5.3.2. Applications to high-order PDEs

Scordelis–Lo roof. A curved cylinder with dimensions $(r,\ L,\ \theta_{\text{sector}}) = (25,\ 50,\ 2\pi/3)$ is loaded under gravity and has the following material parameters:

$$\text{Young's modulus,} \quad E = 4.32 \times 10^8 \ ,$$

$$\text{Poisson's ratio,} \quad \nu = 0.0 \ ,$$

$$\text{Thickness,} \quad t = 0.25 \ .$$

The shell formulation used is based on the Kirchhoff–Love thin shell theory in which transverse shear strains are zero. The end result is a rotation-free formulation requiring C^1 continuous trial functions. Necessarily, since transverse shear strains are suppressed, one would anticipate the theory would result in smaller deformations than for Reissner–Mindlin shell theory, which accounts for transverse shear strains.

Using an analytical height function in conjunction with a planar mesh (a scaled version of the mesh in Figure 25a) to create the cylindrical roof, the solution to the thin-shell problem is shown in Figure 27. The vertical displacement at the mid-point of the straight edges converges toward, but underestimates, the Reissner–Mindlin theory

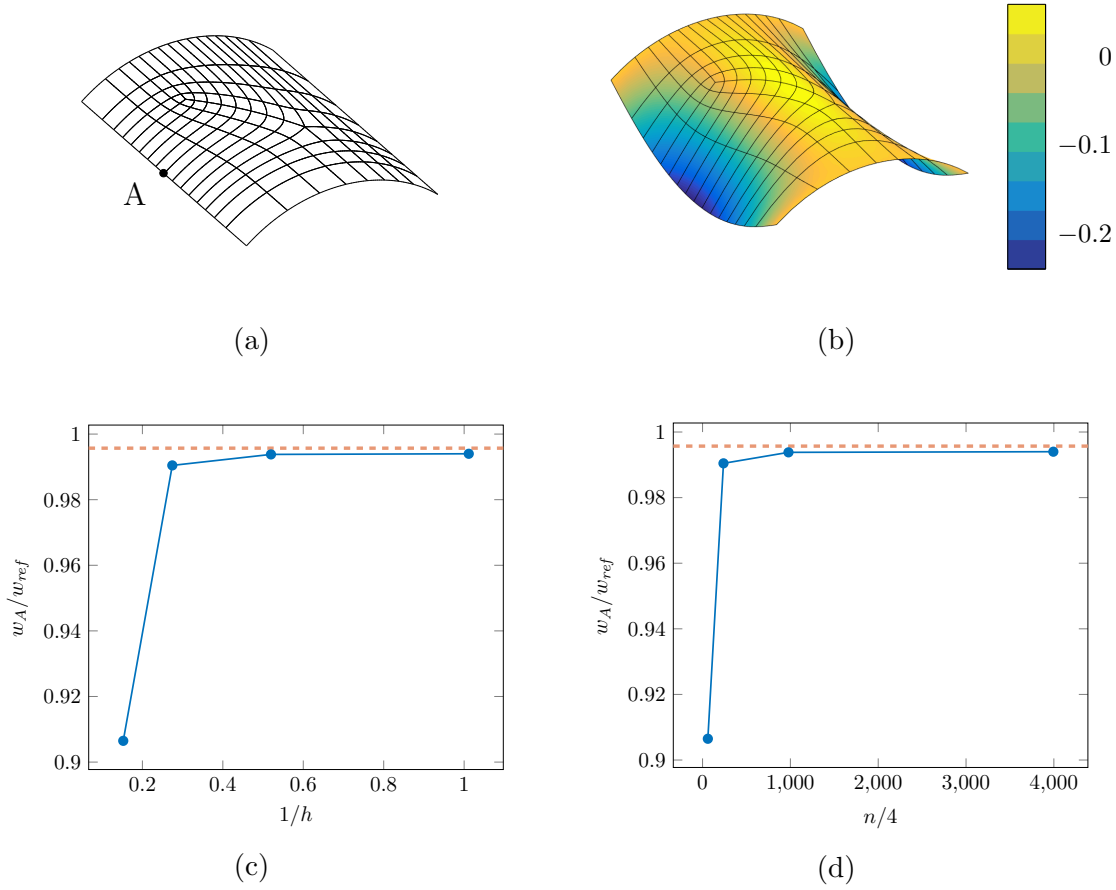

Figure 27: Figures (a) and (b) show the coarsest level of refinement used and the corresponding solution obtained for vertical displacements, respectively. Figures (c) and (d) show convergence of the vertical displacement, w_A, at point A, labelled in Figure (a), with mesh size and number of degrees of freedom, respectively. Note that the results are normalized by a reference solution, w_{ref}, based on trasverse-shear deformable Reissner–Mindlin theory. Our results are based on Kirchhoff–Love thin shell theory in which transverse shear deformations are suppressed, and as one would expect, and as observed above, the Kirchhoff–Love converged displacement is somewhat less than that for Reissner–Mindlin theory. The red dashed line refers to the results obtained using the Kirchhoff–Love theory and a uniform NURBS mesh with $67,000$ degrees of freedom.

reference solution of $w_{ref} = 0.3024$. The computed displacement at the last level of refinement was $w_A = 0.3006$, and in complete agreement with the computations in [37]. Note that we did not exploit any symmetry conditions in the simulation; this is why we plotted the results versus the number of degrees of freedom, n, divided by 4. This brings the results in line with those of [37] which assumed four-fold symmetry. It should be noted that our mesh is intentionally not well suited for the problem and, moreover, we only employed global refinements unlike [37].

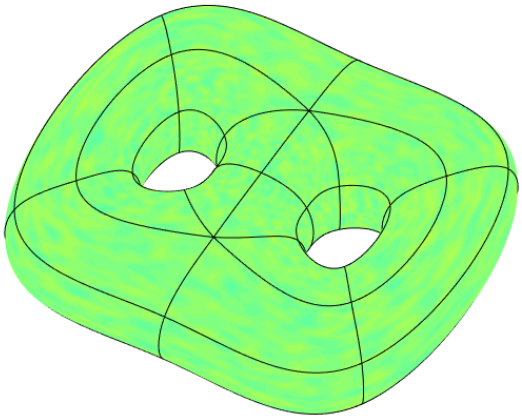

(a) $t = 0$

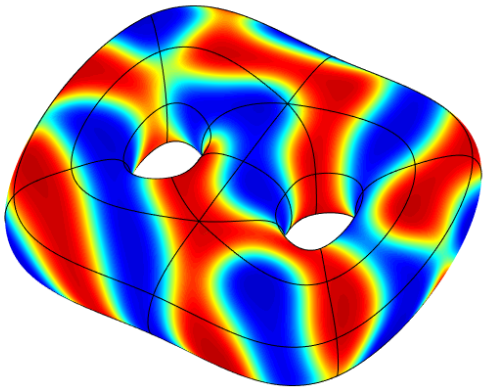

(b) $t = 4.3197 \times 10^{-5}$

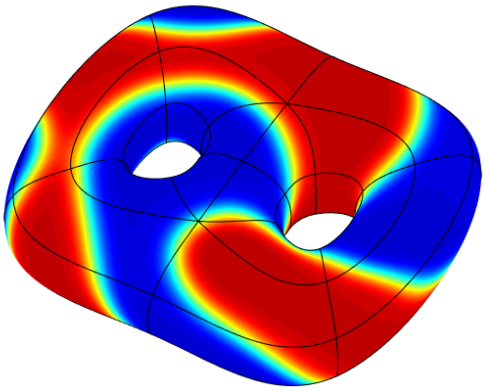

(c) $t = 4.8741 \times 10^{-4}$

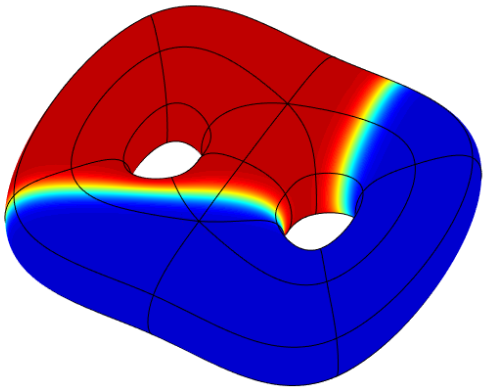

(d) $t = 1.3464 \times 10^{-2}$

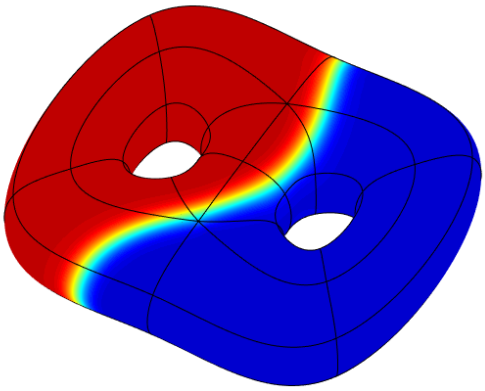

(e) $t = 6.425 \times 10^{-2}$

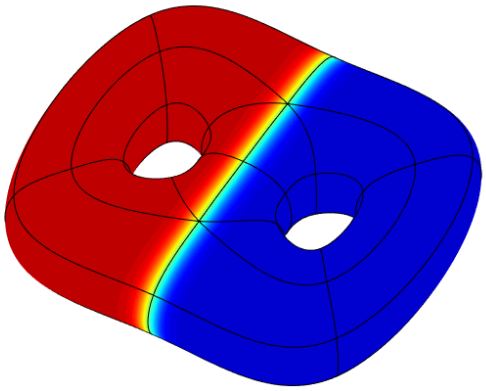

(f) $t = 1006.4156$

Figure 28: Figure (a) shows the initial volume-fraction distribution over the surface of a double-donut, which is the domain of interest for the Cahn–Hilliard problem, and Figures (b)–(f) show its time-evolution. The meshes used for the computation contained $12,382$ degrees of freedom. The few iso-parameter lines plotted above are presented simply to indicate the locations and valences (6) of the extraordinary points.

Cahn–Hilliard. We solve the fourth-order non-linear Cahn–Hilliard problem on the surface of the double-doughnut Ω shown in Figure 28. The following non-dimensional form is considered (see [2]):

$$\frac{\partial c}{\partial t} = \nabla_\Omega \cdot (c(1-c)\nabla_\Omega(\mathbb{N}_2\mu_c - \Delta_\Omega c)) \quad \text{on } \Omega \times [0,\ T]\ ,$$
$$c(\boldsymbol{x}, 0) = c_0(\boldsymbol{x}) \quad \text{on } \Omega\ ,$$

where ∇_Ω and Δ_Ω are the surface gradient and Laplace–Beltrami operators, respectively, and $\mu_c := \frac{1}{3}\log\left(\frac{c}{1-c}\right) + 1 - 2c$. The selected mesh had $12,382$ degrees of freedom, and we solved the equations for initial volume fraction $\bar{c} = 0.5$ and the corresponding value of $\mathbb{N}_2$ was $3,282.5$. The initial value of c, namely c_0, was determined by randomly perturbing $\bar{c}$, as described in [16, 28]. The results are shown in Figure 28. Steady state was reached for the configuration in 650 time-steps. The solution coefficients were strictly between 0 and 1. Then, since the basis functions used are non-negative and form a partition of a unity, one concludes that the computed solution is between 0 and 1 everywhere.

6. Extensions

The promise of the methodology presented here is complemented by several potentially fruitful research topics, and we briefly discuss some of these in the following.

Smoothing matrices. We only considered the smoothing matrices presented in [44] here. However, an interesting question is whether better smoothing matrices can be designed that simultaneously contain all the desirable properties, namely, positivity and idempotence.

Condition numbers. A drawback of the approach, briefly mentioned in Section 5.3, is high condition numbers for very fine meshes, which we assume is a direct consequence of the singular parameterizations employed. Note that the problem was visible only in the case of the biharmonic problem because of the well-known fact that the condition numbers for this problem increase as h^{-4}, where h is the mesh size, even in the

absence of singularities; compare with the Poisson equation where they only increase as h^{-2}. Since C^1 smoothness makes these high-order PDEs easily accessible, further investigations into possible methods of alleviating this problem are warranted.

Non-uniform knots at the extraordinary point. If the uniform knot standardization step from Section 2.2 is not performed, it is still possible to perform the C^1 construction. The framework from [44] is only valid for uniform knot spans. However, coupling with a non-uniform 2×2 split, as outlined in Appendix C, can be employed to adapt the approach to non-uniform knot spans. Nevertheless, in this case the following are some small things one would need to be aware of with regard to geometric modeling (the isogeometric analysis framework stays essentially unchanged):

(a) In the case of non-uniform knots around an extraordinary point, as was also stated in [50], the region of C^1 smoothness of the unstructured spline surfaces would increase as, referring to Figure 6, each transition element would only have C^1 smooth contact with its neighboring transition and irregular elements.

(b) The refinement scheme we proposed in Section 3.3 will not be applicable. In particular, the update rules for the T2 irregular control points will not be the usual knot-insertion rules. However, a way around this approach would be to directly use one of the existing non-uniform subdivision schemes ([7], for example) to update all the irregular control points.

Arbitrary odd polynomial degrees and smoothness. Extensions to arbitrary odd polynomial degrees could be done by coupling the C^1 patch-based construction with the non-uniform subdivision approach outlined in [7] for arbitrary odd polynomial degrees. Then, this would also allow us to achieve second-order smoothness, and higher, at extraordinary points by using high-order singular parameterizations [5, 45, 51].

Other locally refinable spline technologies. It should be clear that the framework is directly applicable to other locally refinable spline technologies, such as LR-splines [14] or (T)HB-splines [15], as long as the following two conditions are met:

(a) Regions of local refinements are sufficiently separated from extraordinary points such that the 2-disk neighborhoods of the latter are "blind" to the former (see Figure 5).

(b) All regular spline functions that are identically zero on the 1-ring elements of extraordinary points are linearly independent (see Remark 2.2).

Note that refinements in the vicinity of extraordinary points could still be carried out using R2 refinements (with these refinements propagating out into the regular regions as per the rules of the particular spline technology being utilized). The issue of performing local refinements close to extraordinary points and, thus, possibly relaxing the first condition above (and the second condition in Definition 2.3) is more involved and requires further investigation.

7. Conclusions

We presented a C^1 construction around extraordinary points for the case of bi-cubic, analysis-suitable T-splines, leveraging the singular parameterizations presented in [44], coupled with the 2×2 element split from [36]. Appreciating the differing requirements posed by geometric modeling and isogeometric analysis, separate spline spaces for both fields were built, and their suitability for applications in these fields was demonstrated by several numerical examples. In particular, superior approximation behavior when solving PDEs was observed.

A key feature of our construction is its locality — only small neighborhoods of extraordinary points are affected — making it highly portable. For example, it would be straightforward to combine the construction here with the one in [54] for smooth polar splines, and the combination would be able to tackle all the usual unstructured configurations. Additionally, performing such a construction in the context of other locally refinable spline technologies (based on local tensor-product structures) should be straightforward.

Finally, we believe that we have created a design and analysis methodology for smooth bi-cubic splines on unstructured quadrilateral meshes containing extraordinary

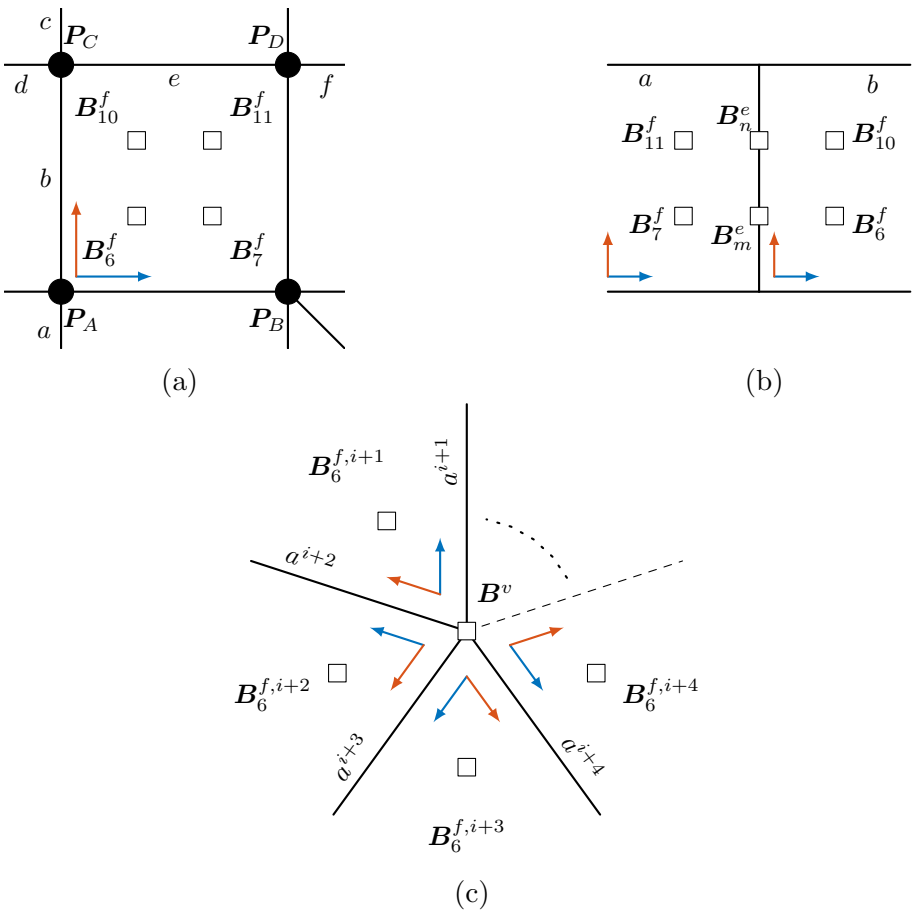

Figure A.29: The spline control points map to the Bézier control points on each elements in $\mathcal{M}_{\text{el}}$ using the rules listed in Equations (A.2), (A.3) and (A.4).

points that, on the one hand, is suitable and attractive for design applications and, on the other hand, achieves optimal, or almost optimal, convergence rates in typical analysis situations and attains desired attributes of an analysis technology.

Acknowledgments

The authors would like to thank Shaolie S. Hossain for access to the system Coronary where some of the simulations were run. Thomas J. R. Hughes was supported by grants from the Office of Naval Research (N00014-17-1-2039). Hendrik Speleers was supported by the MIUR "Futuro in Ricerca 2013" Programme through the project DREAMS (RBFR13FBI3).

Appendix A. Bézier extraction of spline control points

In order to construct the macro extractions used in Sections 3.2 and 4.3, we will make use of the following rules for creating a map from spline control points to Bézier control points. As always, the local coordinate system for Bézier elements will be denoted by the colored arrows, as in Figure 2. All indices in the following equations refer to Figure A.29, where we have relabeled the interior Bézier control points as,

$$\boldsymbol{B}_j^f := \boldsymbol{B}_{pq}, \quad p, q \in \{2, 3\}, \quad j := p + 4q + 1 \ .$$

Additionally, we will make use of the following weighting function,

$$w(a, b) := \frac{a}{a + b} \ . \tag{A.1}$$

Spline $\mapsto$ *Face control points.* Referring to Figure A.29a, define,

$$\begin{aligned} w_v^1 &:= w(a, b + c), \qquad & w_u^1 &:= w(d, e + f) \ , \\ w_v^2 &:= w(a + b, c), \qquad & w_u^2 &:= w(d + e, f) \ , \end{aligned}$$

and let $\bar{w}_z^i := 1 - w_z^i$, $i = 1, 2$ and $z = u, v$. Then, we construct the map from spline control points to the interior Bézier control points as follows,

$$\begin{aligned} \boldsymbol{B}_6^f &= \bar{w}_v^1 \left(\bar{w}_u^1 \boldsymbol{P}_A + w_u^1 \boldsymbol{P}_B \right) + w_v^1 \left(w_u^1 \boldsymbol{P}_D + \bar{w}_u^1 \boldsymbol{P}_C \right) \ , \\ \boldsymbol{B}_7^f &= \bar{w}_v^1 \left(\bar{w}_u^2 \boldsymbol{P}_A + w_u^2 \boldsymbol{P}_B \right) + w_v^1 \left(w_u^2 \boldsymbol{P}_D + \bar{w}_u^2 \boldsymbol{P}_C \right) \ , \\ \boldsymbol{B}_{10}^f &= \bar{w}_v^2 \left(\bar{w}_u^1 \boldsymbol{P}_A + w_u^1 \boldsymbol{P}_B \right) + w_v^2 \left(w_u^1 \boldsymbol{P}_D + \bar{w}_u^1 \boldsymbol{P}_C \right) \ , \\ \boldsymbol{B}_{11}^f &= \bar{w}_v^2 \left(\bar{w}_u^2 \boldsymbol{P}_A + w_u^2 \boldsymbol{P}_B \right) + w_v^2 \left(w_u^2 \boldsymbol{P}_D + \bar{w}_u^2 \boldsymbol{P}_C \right) \ . \end{aligned} \tag{A.2}$$

Face $\mapsto$ *Edge control points.* Referring to Figure A.29b, define,

$$w^1 := w(a, b) \ ,$$

and let $\bar{w}^1 := 1 - w^1$. Then, we construct the map from face control points to the edge-interior Bézier control points as follows,

$$\begin{aligned} \boldsymbol{B}^e_m &= \bar{w}^1 \boldsymbol{B}^f_{11} + w^1 \boldsymbol{B}^f_{10} \ , \\ \boldsymbol{B}^e_n &= \bar{w}^1 \boldsymbol{B}^f_{6} + w^1 \boldsymbol{B}^f_{7} \ . \end{aligned} \tag{A.3}$$

Face $\mapsto$ *Vertex control points.* Referring to Figure A.29c, define,

$$w^i := w(a^{i+2}, a^i) \times w(a^{i-1}, a^{i+1}) \ ,$$

where the index i is to be understood modulo μ, and μ is the number of edges meeting at $\boldsymbol{B}^v$. Then, we construct the map from face control points to the corner Bézier control points as follows,

$$\boldsymbol{B}^v = \frac{4}{\mu} \sum_{i=1}^{\mu} w^i \boldsymbol{B}^{f,i}_6 \ . \tag{A.4}$$

Appendix B. Knot insertion

We will present the knot insertion algorithm in polar form, and what follows is a special case of [8]. In particular, with the neighborhood of an extraordinary point in mind, we will consider the following univariate case:

- cubic splines over the knot interval $[\ \dots,\ t_0,\ t_1,\ t_2,\ t_3,\ t_4,\ \dots\ ]$, where $t_i < t_{i+1}$; and,
- new knots being introduced $[\ \dots,\ u_0,\ u_1,\ u_2,\ u_3,\ \dots\ ]$, where $t_i < u_i < t_{i+1}$,

where the knot spans are assumed to be non-zero to mimic the restriction imposed in Section 3.3, namely, non-zero knot spans in the extraordinary point's neighborhood.

We use the following convenient notation: on a knot vector $[\ \dots,\ \xi_{i-1},\ \xi_i,\ \xi_{i+1},\ \dots\ ]$, the control point of a cubic B-spline associated with the ith knot is indexed by the 3 consecutive knots $\xi_{i-1},\ \xi_i,\ \xi_{i+1}$, i.e., the control point is denoted by $\boldsymbol{P}_{\xi_{i-1}\xi_i\xi_{i+1}}$. Let us focus on the knot intervals $[t_1,\ t_2]$ and $[t_2,\ t_3]$. Both intervals are split into two by the knots u_1 and u_2. Our aim is the computation of the updated control points,

$$\boldsymbol{P}_{t_1 u_1 t_2}, \quad \boldsymbol{P}_{u_1 t_2 u_2}, \quad \boldsymbol{P}_{t_2 u_2 t_3} \ ,$$

on the new knot vector,

$$[\,\ldots,\ t_0,\ u_0,\ t_1,\ u_1,\ t_2,\ u_2,\ t_3,\ u_3,\ t_4,\ \ldots\,]\ .$$

Then, the new points can be computed as follows,

$$\begin{aligned}
\boldsymbol{P}_{t_1u_1t_2} &= \frac{t_3-u_1}{t_3-t_0}\boldsymbol{P}_{t_0t_1t_2} + \frac{u_1-t_0}{t_3-t_0}\boldsymbol{P}_{t_1t_2t_3}\ ,\\
\boldsymbol{P}_{t_2u_2t_3} &= \frac{t_4-u_2}{t_4-t_1}\boldsymbol{P}_{t_1t_2t_3} + \frac{u_2-t_1}{t_4-t_1}\boldsymbol{P}_{t_2t_3t_4}\ ,\\
\boldsymbol{P}_{u_1t_2u_2} &= \frac{t_3-u_2}{t_3-t_1}\boldsymbol{P}_{t_1u_1t_2} + \frac{u_2-u_1}{t_3-t_1}\boldsymbol{P}_{t_1t_2t_3} + \frac{u_1-t_1}{t_3-t_1}\boldsymbol{P}_{t_2u_2t_3}\ .
\end{aligned} \tag{B.1}$$

The rules in higher dimensions are obtained by tensor-products of the above rules, and the above local computations can be performed to compute the refined control points everywhere in the extraordinary point's neighborhood.

Appendix C. Non-uniform knots at the extraordinary point

Instead of performing the first step that makes all spoke edges uniform (see Definition 2.4), we could also perform a C^1 completion at the extraordinary point despite non-uniformity of the spoke edge knot spans. In order to accomplish this, we outline here a simple approach for making the framework in [44] amenable to smooth joins of non-uniform Bézier patches. Once again, assuming that Equation (2.8) is already satisfied when $q = 2, 3$, we adopt the following approach for smoothness imposition.

(a) First, split each $\boldsymbol{x}^i$ into 4 sub-elements $\boldsymbol{x}^{i,jk}$, $j, k \in \{1, 2\}$, by splitting the parent element $\omega^i = [0,\ a^i] \times [0,\ a^{i+1}]$ along parameter lines $u = a/2$ and $v = a/2$ where,

$$a := \min_i(a^i)\ . \tag{C.1}$$

Denoting with $\boldsymbol{S}_a^{i,jk}$ the matrix that acts upon the vector of control points $\boldsymbol{B}_{pq}^i$ to yield control points $\boldsymbol{B}_{pq}^{i,jk}$ when ω^i is split at parameter lines $u = \frac{a}{2}$ and $v = \frac{a}{2}$,

$$\boldsymbol{B}^{i,jk} = \boldsymbol{S}_a^{i,jk}\boldsymbol{B}^i\ . \tag{C.2}$$

Of course, the application of $\boldsymbol{S}_a^{i,jk}$ is equivalent to the application of the de Casteljau algorithm, as before. Compare the above equation with Equation (2.12) and note that the splitting operator depends on i now because of the allowed non-uniformity.

(b) Next, follow the last two steps as outlined in Section 2.1.4 in order to complete the imposition of C^1 smoothness.

References

[1] Surflab: Surface gallery. `http://www.cise.ufl.edu/research/SurfLab/shape_gallery.shtml`.

[2] A. Bartezzaghi, L. Dedè, and A. Quarteroni. Isogeometric analysis of high order partial differential equations on surfaces. *Computer Methods in Applied Mechanics and Engineering*, 295:446–469, 2015.

[3] Y. Bazilevs, V.M. Calo, J.A. Cottrell, J.A. Evans, T.J.R. Hughes, S. Lipton, M.A. Scott, and T.W. Sederberg. Isogeometric analysis using T-splines. *Computer Methods in Applied Mechanics and Engineering*, 199:229–263, 2010.

[4] Y. Bazilevs, M.-C. Hsu, and M.A. Scott. Isogeometric fluid–structure interaction analysis with emphasis on non-matching discretizations, and with application to wind turbines. *Computer Methods in Applied Mechanics and Engineering*, 249:28–41, 2012.

[5] H. Bohl and U. Reif. Degenerate Bézier patches with continuous curvature. *Computer Aided Geometric Design*, 14:749–761, 1997.

[6] M.J. Borden, M.A. Scott, J.A. Evans, and T.J.R. Hughes. Isogeometric finite element data structures based on Bézier extraction of NURBS. *International Journal for Numerical Methods in Engineering*, 87:15–47, 2011.

[7] T.J. Cashman, U.H. Augsdörfer, N.A. Dodgson, and M.A. Sabin. NURBS with extraordinary points: High-degree, non-uniform, rational subdivision schemes. *ACM Transactions on Graphics*, 28:Article No. 46, 2009.

[8] T.J. Cashman, N.A. Dodgson, and M.A. Sabin. A symmetric, non-uniform, refine and smooth subdivision algorithm for general degree B-splines. *Computer Aided Geometric Design*, 26:94–104, 2009.

[9] F. Cirak and M. Ortiz. Fully C^1-conforming subdivision elements for finite deformation thin-shell analysis. *International Journal for Numerical Methods in Engineering*, 51:813–833, 2001.

[10] F. Cirak, M. Ortiz, and P. Schröder. Subdivision surfaces: A new paradigm for thin-shell finite-element analysis. *International Journal for Numerical Methods in Engineering*, 47:2039–2072, 2000.

[11] A. Collin, G. Sangalli, and T. Takacs. Analysis-suitable G^1 multi-patch parametrizations for C^1 isogeometric spaces. *Computer Aided Geometric Design*, 47:93–113, 2016.

[12] J.A. Cottrell, T.J.R. Hughes, and Y. Bazilevs. *Isogeometric Analysis: Toward Integration of CAD and FEA*. John Wiley & Sons, 2009.

[13] J. Deng, F. Chen, X. Li, C. Hu, W. Tong, Z. Yang, and Y. Feng. Polynomial splines over hierarchical T-meshes. *Graphical Models*, 70:76–86, 2008.

[14] T. Dokken, T. Lyche, and K.F. Pettersen. Polynomial splines over locally refined box-partitions. *Computer Aided Geometric Design*, 30:331–356, 2013.

[15] C. Giannelli, B. Jüttler, and H. Speleers. THB-splines: The truncated basis for hierarchical splines. *Computer Aided Geometric Design*, 29:485–498, 2012.

[16] H. Gómez, V.M. Calo, Y. Bazilevs, and T.J.R. Hughes. Isogeometric analysis of the Cahn–Hilliard phase-field model. *Computer Methods in Applied Mechanics and Engineering*, 197:4333–4352, 2008.

[17] C.M. Grimm and J.F. Hughes. Modeling surfaces of arbitrary topology using manifolds. In

Proceedings of the 22nd Annual Conference on Computer Graphics and Interactive Techniques, pages 359–368. ACM Press, 1995.

[18] D. Groisser and J. Peters. Matched G^k-constructions always yield C^k-continuous isogeometric elements. *Computer Aided Geometric Design*, 34:67–72, 2015.

[19] T.J.R. Hughes. *The Finite Element Method: Linear Static and Dynamic Finite Element Analysis.* Courier Corporation.

[20] T.J.R. Hughes, J.A. Cottrell, and Y. Bazilevs. Isogeometric analysis: CAD, finite elements, NURBS, exact geometry and mesh refinement. *Computer Methods in Applied Mechanics and Engineering*, 194:4135–4195, 2005.

[21] M. Kapl and V. Vitrih. Space of C^2-smooth geometrically continuous isogeometric functions on two-patch geometries. *Computers & Mathematics with Applications*, 73:37–59, 2017.

[22] M. Kapl, V. Vitrih, B. Jüttler, and K. Birner. Isogeometric analysis with geometrically continuous functions on two-patch geometries. *Computers & Mathematics with Applications*, 70:1518–1538, 2015.

[23] K. Karčiauskas, T. Nguyen, and J. Peters. Generalizing bicubic splines for modeling and IGA with irregular layout. *Computer-Aided Design*, 70:23–35, 2016.

[24] K. Karčiauskas and J. Peters. Minimal bi-6 G^2 completion of bicubic spline surfaces. *Computer Aided Geometric Design*, 41:10–22, 2016.

[25] X. Li. Some properties for analysis-suitable T-splines. *Journal of Computational Mathematics*, 33:428–442, 2015.

[26] X. Li and M.A. Scott. Analysis-suitable T-splines: Characterization, refineability, and approximation. *Mathematical Models and Methods in Applied Sciences*, 24:1141–1164, 2014.

[27] X. Li, J. Zheng, T.W. Sederberg, T.J.R. Hughes, and M.A. Scott. On linear independence of T-spline blending functions. *Computer Aided Geometric Design*, 29:63–76, 2012.

[28] J. Liu, L. Dedè, J.A. Evans, M.J. Borden, and T.J.R. Hughes. Isogeometric analysis of the advective Cahn–Hilliard equation: Spinodal decomposition under shear flow. *Journal of Computational Physics*, 242:321–350, 2013.

[29] C. Loop. Second order smoothness over extraordinary vertices. In R. Scopigno and D. Zorin, editors, *Eurographics Symposium on Geometry Processing 2004*, pages 165–174, 2004.

[30] C. Loop and S. Schaefer. Approximating Catmull–Clark subdivision surfaces with bicubic patches. *ACM Transactions on Graphics*, 27:Article No. 8, 2008.

[31] C. Loop and S. Schaefer. G^2 tensor product splines over extraordinary vertices. *Computer Graphics Forum*, 27:1373–1382, 2008.

[32] M. Majeed and F. Cirak. Isogeometric analysis using manifold-based smooth basis functions. *Computer Methods in Applied Mechanics and Engineering*, 316:547–567, 2017.

[33] J.C. Navau and N.P. Garcia. Modeling surfaces from meshes of arbitrary topology. *Computer Aided Geometric Design*, 17:643–671, 2000.

[34] T. Nguyen, K. Karčiauskas, and J. Peters. A comparative study of several classical, discrete differential and isogeometric methods for solving Poisson's equation on the disk. *Axioms*, 3:280–299, 2014.

[35] T. Nguyen, K. Karčiauskas, and J. Peters. C^1 finite elements on non-tensor-product 2d and 3d manifolds. *Applied Mathematics and Computation*, 272:148–158, 2016.

[36] T. Nguyen and J. Peters. Refinable C^1 spline elements for irregular quad layout. *Computer Aided Geometric Design*, 43:123–130, 2016.

[37] N. Nguyen-Thanh, J. Kiendl, H. Nguyen-Xuan, R. Wüchner, K.U. Bletzinger, Y. Bazilevs, and T. Rabczuk. Rotation free isogeometric thin shell analysis using PHT-splines. *Computer Methods in Applied Mechanics and Engineering*, 200:3410–3424, 2011.

[38] J. Peters. Patching Catmull–Clark meshes. In *Proceedings of the 27th Annual Conference on Computer Graphics and Interactive Techniques*, pages 255–258. ACM Press, 2000.

[39] J. Peters and U. Reif. *Subdivision Surfaces.* Springer-Verlag, 2008.

[40] H. Prautzsch. Freeform splines. *Computer Aided Geometric Design*, 14:201–206, 1997.

[41] H. Prautzsch. Smoothness of subdivision surfaces at extraordinary points. *Advances in Computational Mathematics*, 9:377–389, 1998.

[42] U. Reif. A unified approach to subdivision algorithms near extraordinary vertices. *Computer Aided Geometric Design*, 12:153–174, 1995.

[43] U. Reif. A degree estimate for subdivision surfaces of higher regularity. *Proceedings of the American Mathematical Society*, 124:2167–2174, 1996.

[44] U. Reif. A refineable space of smooth spline surfaces of arbitrary topological genus. *Journal of Approximation Theory*, 90:174–199, 1997.

[45] U. Reif. TURBS-topologically unrestricted rational B-splines. *Constructive Approximation*, 14:57–77, 1998.

[46] A. Riffnaller-Schiefer, U.H. Augsdörfer, and D.W. Fellner. Isogeometric shell analysis with NURBS compatible subdivision surfaces. *Applied Mathematics and Computation*, 272:139–147, 2016.

[47] G. Sangalli, T. Takacs, and R. Vázquez. Unstructured spline spaces for isogeometric analysis based on spline manifolds. *Computer Aided Geometric Design*, 47:61–82, 2016.

[48] M.A. Scott, M.J. Borden, C.V. Verhoosel, T.W. Sederberg, and T.J.R. Hughes. Isogeometric finite element data structures based on Bézier extraction of T-splines. *International Journal for Numerical Methods in Engineering*, 88:126–156, 2011.

[49] M.A. Scott, X. Li, T.W. Sederberg, and T.J.R. Hughes. Local refinement of analysis-suitable T-splines. *Computer Methods in Applied Mechanics and Engineering*, 213:206–222, 2012.

[50] M.A Scott, R.N. Simpson, J.A. Evans, S. Lipton, S.P.A. Bordas, T.J.R. Hughes, and T.W. Sederberg. Isogeometric boundary element analysis using unstructured T-splines. *Computer Methods in Applied Mechanics and Engineering*, 254:197–221, 2013.

[51] T.W. Sederberg, H. Lin, and X. Li. Curvature of singular Bézier curves and surfaces. *Computer Aided Geometric Design*, 28:233–244, 2011.

[52] T.W. Sederberg, J. Zheng, D. Sewell, and M. Sabin. Non-uniform recursive subdivision surfaces. In *Proceedings of the 25th Annual Conference on Computer Graphics and Interactive Techniques*, pages 387–394. ACM Press, 1998.

[53] J. Stam. Exact evaluation of Catmull–Clark subdivision surfaces at arbitrary parameter values. In *Proceedings of the 25th Annual Conference on Computer Graphics and Interactive Techniques*, pages 395–404. ACM Press, 1998.

[54] D. Toshniwal, H. Speleers, R.R. Hiemstra, and T.J.R. Hughes. Multi-degree smooth polar splines: A framework for geometric modeling and isogeometric analysis. *Computer Methods in Applied Mechanics and Engineering*, 316:1005–1061, 2017.

[55] W.A. Wall, M.A. Frenzel, and C. Cyron. Isogeometric structural shape optimization. *Computer Methods in Applied Mechanics and Engineering*, 197:2976–2988, 2008.

[56] X. Wei, Y. Zhang, T.J.R. Hughes, and M.A. Scott. Truncated hierarchical Catmull–Clark subdivision with local refinement. *Computer Methods in Applied Mechanics and Engineering*, 291:1–20, 2015.

[57] X. Wei, Y. Zhang, L. Liu, and T.J.R. Hughes. Truncated T-splines: Fundamentals and methods. *Computer Methods in Applied Mechanics and Engineering*, 316:349–372, 2017.

[58] M. Wu, B. Mourrain, A. Galligo, and B. Nkonga. Hermite type spline spaces over rectangular meshes with arbitrary topology. *Communications in Computational Physics*, 21:835–866, 2017.

[59] L. Ying and D. Zorin. A simple manifold-based construction of surfaces of arbitrary smoothness. *ACM Transactions on Graphics*, 23:271–275, 2004.

[60] X. Yuan and K. Tang. Rectified unstructured T-splines with dynamic weighted refinement for improvement in geometric consistency and approximation convergence. *Computer Methods in Applied Mechanics and Engineering*, 316:373–399, 2017.

[61] J. Zhang and X. Li. On the linear independence and partition of unity of arbitrary degree analysis-suitable T-splines. *Communications in Mathematics and Statistics*, 3:353–364, 2015.

[62] Y. Zhang, Y. Bazilevs, S. Goswami, C.L. Bajaj, and T.J.R. Hughes. Patient-specific vascular NURBS modeling for isogeometric analysis of blood flow. *Computer Methods in Applied Mechanics and Engineering*, 196:2943–2959, 2007.